Assessment of Radiative Heating Uncertainty for Hyperbolic Earth Entry

Christopher O. Johnston,* Alireza Mazaheri,* Peter Gnoffo,† Bil Kleb‡
NASA Langley Research Center, Hampton, VA 23681
Kenneth Sutton §
National Institute of Aerospace, Hampton, VA 23669
Dinesh Prabhu ¶
ERC Corporation, Mountain View, CA 94035
Aaron M. Brandis ‖
University Affiliated Research Center with University of California Santa Cruz, Mountain View, CA 94035
and
Deepak Bose **
NASA Ames Research Center, Mountain View, CA 94035

This paper investigates the shock-layer radiative heating uncertainty for hyperbolic Earth entry, with the main focus being a Mars return. In Part I of this work, a baseline simulation approach involving the LAURA Navier-Stokes code with coupled ablation and radiation is presented, with the HARA radiation code being used for the radiation predictions. Flight cases representative of peak-heating Mars or asteroid return are defined and the strong influence of coupled ablation and radiation on their aerothermodynamic environments are shown. Structural uncertainties inherent in the baseline simulations are identified, with turbulence modeling, precursor absorption, grid convergence, and radiation transport uncertainties combining for a +34% and −24% structural uncertainty on the radiative heating. A parametric uncertainty analysis, which assumes interval uncertainties, is presented. This analysis accounts for uncertainties in the radiation models as well as heat of formation uncertainties in the flowfield model. Discussions and references are provided to support the uncertainty range chosen for each parameter. A parametric uncertainty of +47.3% and −28.3% is computed for the stagnation-point radiative heating for the 15 km/s Mars-return case. A breakdown of the largest individual uncertainty contributors is presented, which includes C_3 Swings cross-section, photoionization edge shift, and Opacity Project atomic lines. Combining the structural and parametric uncertainty components results in a total uncertainty of +81.3% and −52.3% for the Mars-return case.

In Part II, the computational technique and uncertainty analysis presented in Part I are applied to 1960s era shock-tube and constricted-arc experimental cases. It is shown that experiments contain shock layer temperatures and radiative flux values relevant to the Mars-return cases of present interest. Comparisons between the predictions and measurements, accounting for the uncertainty in both, are made for a range of experiments. A measure of comparison quality is defined, which consists of the percent overlap of the predicted uncertainty bar with the corresponding measurement uncertainty bar. For nearly

*Aerospace Engineer, Aerothermodynamics Branch, Research Technology Directorate, AIAA Member.
†Aerospace Engineer, Aerothermodynamics Branch, Research Technology Directorate, AIAA Fellow.
‡Aerospace Engineer, Aerothermodynamics Branch, Research Technology Directorate, AIAA Lifetime Member.
§Research Scientist, AIAA Associate Fellow
¶Senior Research Scientist, AIAA Associate Fellow
‖Associate Research Scientist, AIAA Professional Member
**Senior Research Scientist, AIAA Associate Fellow.

all cases, this percent overlap is greater than zero, and for most of the higher temperature cases (T >13,000 K) it is greater than 50%. These favorable comparisons provide evidence that the baseline computational technique and uncertainty analysis presented in Part I are adequate for Mars-return simulations.

In Part III, the computational technique and uncertainty analysis presented in Part I are applied to EAST shock-tube cases. These experimental cases contain wavelength dependent intensity measurements in a wavelength range that covers 60% of the radiative intensity for the 11 km/s, 5 m radius flight case studied in Part I. Comparisons between the predictions and EAST measurements are made for a range of experiments. The uncertainty analysis presented in Part I is applied to each prediction, and comparisons are made using the metrics defined in Part II. The agreement between predictions and measurements is excellent for velocities greater than 10.5 km/s. Both the wavelength dependent and wavelength integrated intensities agree within 30% for nearly all cases considered. This agreement provides confidence in the computational technique and uncertainty analysis presented in Part I, and provides further evidence that this approach is adequate for Mars-return simulations.

Part IV of this paper reviews existing experimental data that include the influence of massive ablation on radiative heating. It is concluded that this existing data is not sufficient for the present uncertainty analysis. Experiments to capture the influence of massive ablation on radiation are suggested as future work, along with further studies of the radiative precursor and improvements in the radiation properties of ablation products.

I. Nomenclature

a_i	Curve-fit coefficients for experimental data least-squares fits (i=1,2,3)
$B_{h\nu}$	Planck Function
C_P	Gas specific heat (J/K/mol)
c	Speed of light
E	Enthalpy flux into the shock layer (W/m^2)
E_i	Energy of electronic state i
E_I	Ionization potential of an atom
f_{ij}	Atomic line oscillator strength between electronic levels i and j
g_i	Degeneracy of electronic state i
h_w	Enthalpy of gas at wall (J/kg)
H	Gas enthalpy (J/mol)
I (0–6 eV)	Wall-directed radiative intensity spectrally-integrated between 0 and 6 eV (W/cm^2/sr)
J (0–6 eV)	Spectrally-integrated emission between 0 and 6 eV (W/cm^3/sr)
J_c	Wavelength-integrated intensity divided by shock-tube diameter (W/cm^3/sr)
J_λ	Wavelength dependent intensity divided by shock-tube diameter (W/cm^3/sr/μ)
$\dot{m}_c$	Mass flux of surface char (kg/m^2/s)
$\dot{m}_g$	Mass flux of pyrolysis gas at the surface (kg/m^2/s)
$\dot{m}$	Total mass flux at the surface = $\dot{m}_c + \dot{m}_g$ (kg/m^2/s)
N_+	Ion number density (particles/cm^3)
N_e	Electron number density (particles/cm^3)
N_a	Neutral atom number density (particles/cm^3)
p	Pressure (N/m^2)
Q_+	Electronic partition function of an ion
Q_a	Electronic partition function of an atom
q_{conv}	Convective heating (W/cm^2)
q_{rad}	Wall-directed radiative flux at the wall (W/cm^2)
$q_{r,\lambda}$	Wavelength-dependent wall-directed radiative flux (W/cm^2/μ)
$q^-_{r,\nu}$	Frequency-dependent wall-directed radiative flux without radiation-flowfield coupling(W/cm^2)
R	Universal gas constant (J/mol/K)
T	Temperature (K)
U	Free-stream velocity for flight case or moving shock speed for shock tube case (km/s)
x	Curve fit variable, U (km/s) for shock tube cases and T (K) for constricted arc cases
z	Radial distance normal to the free-stream (cm)

ΔE_I	Reduction in the ionization potential (eV)
$\Delta H_f(0)$	Heat of formation (kJ/mol)
$\Delta\lambda_{S,0}$	Stark broadening width at 10,000 K and 10^{16} cm^{-3} electron number density
Δz	thickness of a constant property layer
δ	shock standoff distance (cm)
$\kappa_{h\nu}$	frequency dependent absorption coefficient
λ	wavelength (nm)
$\lambda_{CL,mult}$	Atomic multiplet centerline wavelength (nm)
$h\nu$	Photon frequency (eV)
ρ	Free stream density (kg/m^3)
ρ_c	Ablator char density (kg/m^3)
ρ_v	Ablator virgin density (kg/m^3)
σ_{bf}	Atomic photoionization absorption cross section (cm^2)

Part I
Flight Simulation Modeling and Uncertainty

II. Introduction to Part I

The purpose of this paper is to provide a radiative heating uncertainty estimate for vehicles at hyperbolic Earth entry conditions. In particular, conditions relevant to Mars or an asteroid return will be studied. Peak heating conditions for these entries may include velocities as high as 15 km/s at an altitude of 60 km.[1] Such conditions result in a shock-layer that is fundamentally different than that formed for Lunar-return conditions (10.5 km/s at 60 km). Shock layer temperatures and ionization levels are significantly higher for the 15 km/s entry than the 10.5 km/s case. This higher velocity leads to radiation and ablation coupling having a strong influence on the flowfield structure, which complicates the flowfield modeling. Furthermore, the radiative heating is dominant over the convective heating at 15 km/s, especially when coupled ablation is considered. This motivates the present focus on radiative heating rather than convective.

Many computational aerothermodynamic studies of Mars-return entry conditions exist in the literature. Stagnation line viscous shock layer solutions with coupled radiation only[2] and coupled radiation and ablation [3–14] were performed with various levels of fidelity in the flowfield and radiation models. These studies confirm the significant influence of coupled radiation and ablation on the radiative heating for a Mars-return case. A coupled ablation and radiation analysis by Bartlett et al.[15] considered the entire trajectory for an Apollo capsule entering Earth at 15.24 km/s. This study showed that the convective heating during the peak heating pulse is reduced to essentially zero. Navier-Stokes simulations with coupled radiation[16,17] and coupled radiation and ablation[18] have been performed recently and shown to agree well with past viscous shock layer results.

Other computational studies relevant to a Mars-return entry include those by Tauber et al.,[19] Park and Davies,[20] Park and Milos,[21] Sutton and Hartung,[22] and Cambier and Tauber.[23] The study by Tauber et al.[19] applied a chemical nonequilibrium single temperature flowfield model without coupled radiation and ablation to study the entry of a 1 – 5 m radius vehicle at an entry velocity of 14 km/s. Park and Davies[20] studied the 14 and 16 km/s entry trajectories for a 3-m radius entry vehicle using the Fay and Riddell formula for the non-ablative convective heating and the NEQAIR[24] code for the radiative heating. For the NEQAIR computations, the conditions behind a normal shock were considered and the shock-layer was assumed isothermal, adiabatic, and optically-thin. All of these assumptions should result in an over-prediction of the radiative flux. For an L/D of zero, the maximum radiative heating was found to equal 3,000 and 6,000 W/cm^2 for the 14 and 16 km/s entry cases, respectively. Sutton and Hartung[22] provided radiative heating values for the stagnation point of hemispheres with radii ranging from 0.05 to 10.0 m. The velocity and altitude ranged from 8 to 18 km/s and 30 to 84 km, respectively. The stagnation-line flowfield computation assumed inviscid flow with coupled radiation. The RAD/EQUIL[25] code was applied for the radiation predictions. Cambier and Tauber[23] applied a nonequilibrium single-temperature Navier-Stokes solver without coupled radiation or ablation to determine the non-ablating convective heating rates. A free-stream condition consisting of a velocity of 14.26 km/s and density of 2.42×10^{-4} kg/m^3 was studied for a

vehicle with a nose radius of 1 m. Ablation and radiative heating were not considered in this study.

Past studies to determine the radiative heating uncertainty for a Mars-return Earth entry have been performed by Coleman et al.[26] and Rolin and Yurevich.[27] The 1960s era study by Coleman et al. investigated the influence of air radiation uncertainties on an inviscid flowfield without ablation. Their analysis consisted of increasing the atomic photoionization cross sections, atomic line oscillator strengths, and atomic line Stark broadening half widths by a factor of two, in addition to a 100% increase in the negative ion photodetachment cross section. These changes resulted in a 15% increase in the radiative heating for an Apollo shaped vehicle at a velocity of 17.4 km/s and an altitude of 53.3 km. Interestingly, they also showed a 40% increase by applying the same changes to a case with a velocity of 10.7 km/s. This larger difference at a lower velocity was a result of the larger negative ion photodetachment contribution at lower velocities. Using a stagnation-line viscous shock layer analysis with coupled ablation, the study by Rolin and Yurevich in the 1980s compared various radiation models for a 1 m radius sphere at 15 km/s with graphite ablation. The different radiation models considered by Rolin and Yurevich consisted of various ablation product and air spectral models. Differences of less than 10% were predicted for the radiative flux resulting from these various models.

Uncertainty analyses of the radiative heating for Lunar return cases, which may provide some insight into the present Mars-return cases, have been performed by Kleb and Johnston[28] and Palmer.[29] The study by Kleb and Johnston investigated the parametric uncertainties inherent in the HARA radiation code, such as atomic line oscillator strengths and Stark broadening half widths. They computed an uncertainty of roughly $\pm 30\%$ for Orion Lunar-return and Fire II cases, with the negative ion photodetachment cross section providing the largest individual uncertainty contribution. The limited data available for the majority of radiation parameters led Kleb and Johnston to apply an interval uncertainty analysis, which is appropriate for epistemic uncertainties (uncertainties due to lack of knowledge). Conversely, the study by Palmer investigated the parametric uncertainties within the flowfield code, such as chemical reaction rate constants and collision cross sections, and computed an uncertainty of less than $\pm 2\%$ for Orion Lunar-return and Fire II cases. Palmer applied a Monte-Carlo analysis, which is appropriate for aleatory uncertainties (uncertainties due to chance).

Sensitivity analyses for a Jupiter entry, which is relevant to the present case since it contains significant radiation and ablation coupling, have been performed by Moss and Simmonds,[30] Park,[31] and Nelson.[32] Moss and Simmonds show the radiative heating sensitivity to the cross section chosen for the C_3 Swings band system and the heats of formation of C_2H, C_3H, and C_4H. A variation of roughly 10% in the radiative heating is found as result of varying these parameters to values found in the literature at the time. Park showed a 25% reduction in the radiative heating by using updated thermodynamic properties for hydrogen, and another 5% reduction by including additional C_2 and C_3 band systems in the vacuum ultraviolet. Nelson studied the sensitivity of the radiative heating to numerous radiation and flowfield parameters. The largest sensitivity was shown to be to C_2 radiation, and unlike Moss's or Park's studies, the sensitivity to C_3 was found to be small. Overall, these Jupiter entry studies provide excellent guidance for the present study, and many of the reported trends are similar to those found in the present work.

The purpose of the present paper is to determine the radiative heating uncertainty at Mars-return entry conditions. Although an uncertainty analysis of the radiative heating for Lunar return conditions was presented by Kleb and Johnston,[28] the shock-layer for the Mars-return case is at significantly higher temperature and pressure than for the Lunar return case. As a result, some physical phenomena not considered by Kleb and Johnston[28] for the Lunar return case may be important for the Mars-return case. These phenomena are identified and discussed in this paper (in Sections VI and VII). This analysis will be based on the state-of-the art LAURA flowfield and HARA radiation codes, which are reviewed in Section III. A review of the influence of ablation coupling on radiative and convective heating is provided in Section IV for a range of entry velocities. Section V focuses on the conservative 15 km/s Mars-return condition and shows details of the coupled flowfield and wall radiative flux spectrum. The uncertainty determined in this study is the combination of a structural and parametric uncertainty component. The various contributors to the structural component are described in detail in Section VI. Similarly, the various contributors to the parametric uncertainty are described in Section VII. The uncertainty results for a range of velocities are presented in Section VIII and the final uncertainty values are discussed in Section IX. Parts II and III of this work, which contain comparisons with experimental data, are also discussed briefly in Section IX.

III. Overview of Baseline Computational Approach

The LAURA v5 Navier-Stokes solver[33] was applied in this work, which includes the coupled ablation and radiation capability discussed by Gnoffo et al.[34] As will be shown in Sections IV and V, the influence of coupled radiation and ablation is significant at Mars-return conditions. As a result, coupled radiation and ablation are included in the baseline predictions. The baseline predictions also include a two-temperature thermochemcial nonequilibrium model and the following 26 species throughout the flowfield (including the wall): N, N^+, NO, NO^+, N_2, $N_2{}^+$, O, O^+, O_2, $O_2{}^+$, e^-, C, C^+, CO, CO_2, C_2, C_3, C_4, C_5, C_2H, C_2H_2, CN, H, H_2, HCN, and CH. The thermodynamic properties for these species were obtained from Gordon and Mcbride.[35] The transport properties were obtained from Wright et al.[36,37] where available. The remaining species were treated using the approximate approach of Svehla[38] modified as suggested by Park.[39] The chemical reaction rates applied were the same as those applied by Johnston et al.[40] The baseline predictions are assumed completely turbulent using the Cebeci-Smith turbulence model[41,42] with a turbulent Schmidt number of 0.9. The influence of turbulence on the radiative heating is discussed in Section VI-A.

The steady-state ablation approximation was applied to compute the wall temperatures and ablation rates. This approximation requires the solution of an approximate surface energy equation:

$$-q_c - \alpha q_{rad} + \epsilon\sigma {T_w}^4 + (\dot{m}_c + \dot{m}_g)h_w = 0 \tag{1}$$

which assumes that the char surface and virgin material recede at the same linear rate. The steady-state ablation approximation provides the following relationship for $\dot{m}_g$:

$$\dot{m}_g = \left(\frac{\rho_v}{\rho_c} - 1\right)\dot{m}_c \tag{2}$$

A carbon-phenolic ablator was assumed throughout this work, with the elemental composition listed in Table 1. The ratio of virgin to char densities required in Eq. (2) was assumed equal to 2.125. The steady-state ablation assumption provides a convenient method for determining plausible ablation rates and wall temperatures, and it is likely an accurate assumption at the peak heating conditions of interest in this work. However, the focus of the present work is the uncertainty of the radiative heating assuming a given ablation rate, meaning that the present work will not treat the influence of uncertainties in the ablator. A separate study similar to that performed by Rindal and Powars,[43] Bueche,[44] or Chen et al.[45] would be required to treat these ablator uncertainties.

The HARA radiation code is coupled to the LAURA flowfield solver to provide coupled radiation predictions. The HARA code applies up-to-date spectral and excitation rate data to an efficient computational algorithm to allow fast and accurate radiation predictions. The baseline radiation properties for air species are discussed by Johnston et al.,[46] while the radiation properties for ablation properties are discussed by Johnston et al.[18] The baseline HARA predictions apply a smeared rotational band (SRB) approach for modeling molecular band systems. The accuracy of the SRB model for the present cases is examined in Section VI-E. The tangent slab approximation is applied for radiation transport using the approach of Johnston.[47] The structural uncertainty introduced by the tangent slab approximation is studied in Section VI-C.

Table 1: Elemental mass fractions assumed for the carbon-phenolic ablator.

Element	Char	Pyrolysis
C	1.0	0.547
H	0.0	0.093
O	0.0	0.341
N	0.0	0.019

IV. Heating Rates Over a Range of Velocities with Coupled Ablation and Radiation

To provide insight into the influence of ablation, vehicle radius, and velocity on the radiative and convective heating, this section presents heating rates for 1 m and 5 m radii spheres at a range of velocities between 10 and 15 km/s with a free-stream density of 3.0×10^{-4} kg/m^3. The ablation rates and wall temperatures are computed assuming steady state ablation of a carbon phenolic ablator, as discussed in Section III. Although the Mars-return case of a 5 m radius sphere at 15 km/s will be the focus of the majority of this paper, the consideration of the lower velocity and smaller radius cases presented here makes clear the transition from more conventional Lunar return type cases at 10 – 11 km/s to the more severe Mars-return cases at 14 – 15 km/s.

For a 1 m radius sphere, the radiative and convective heating rates at the stagnation point and a downstream point are presented in Figs. 1 and 2, respectively, for a range of velocities. The corresponding ablation rates for these points are shown in Fig. 3. Similarly, for a 5 m radius sphere, the ablation rates are shown in Fig. 4, while the heating rates are presented in Figs. 5 and 6. These figures show that for both the 1 and 5 m radii spheres, ablation reduces the radiative and convective heating significantly above 13 km/s. Note that the influence of ablation is less for the downstream point because the local ablation rate is lower, as indicated in Figs. 3 and 4. Also, observe that the typically assumed linear relationship between radiative heating and nose radius is not seen for these cases. For example, the non-ablating stagnation-point radiation increases by only a factor of 1.8 when going from a radius of 1 m to 5 m for the 15 km/s case. This is a result of coupled radiation being treated and that the spectrums are far from being optically thin.

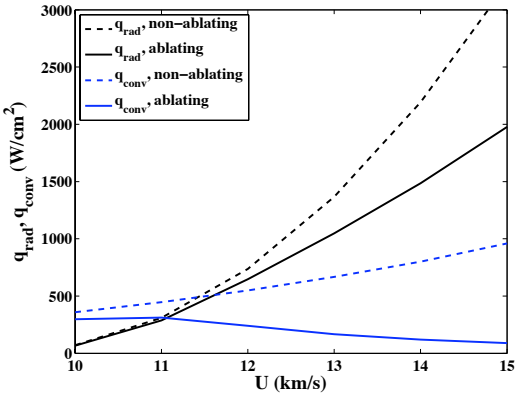

Figure 1: Predicted radiative and convective heating at the stagnation point of a 1 m radius sphere.

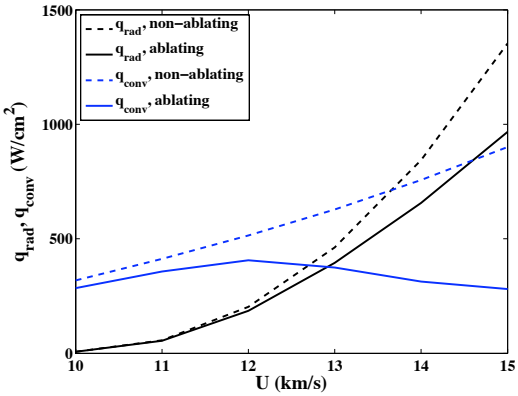

Figure 2: Predicted radiative and convective heating at $z = 0.6$ m of a 1 m radius sphere.

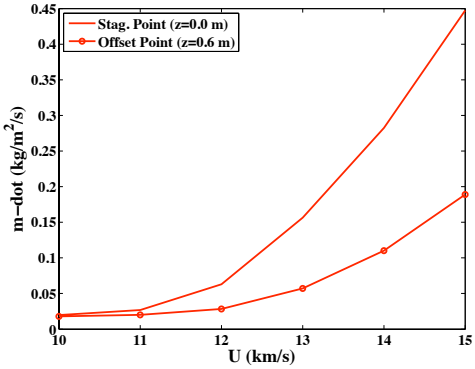

Figure 3: Computed steady-state ablation rates for the 1 m radius sphere.

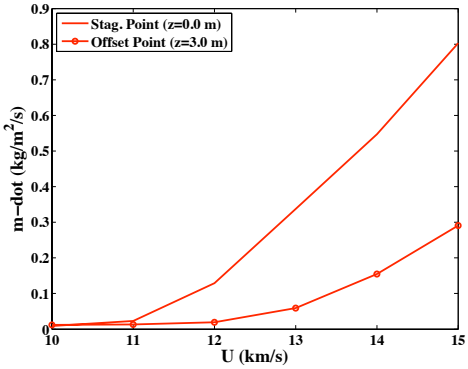

Figure 4: Computed steady-state ablation rates for the 5 m radius sphere.

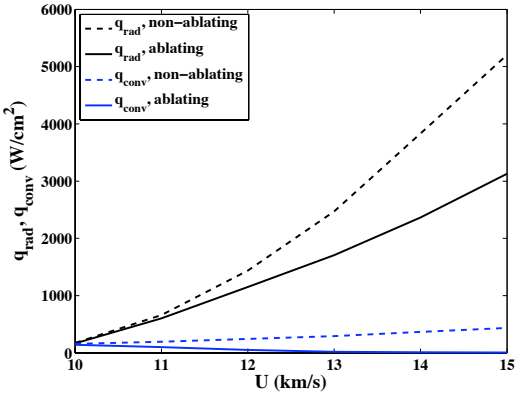

Figure 5: Predicted radiative and convective heating at the stagnation point of a 5 m radius sphere.

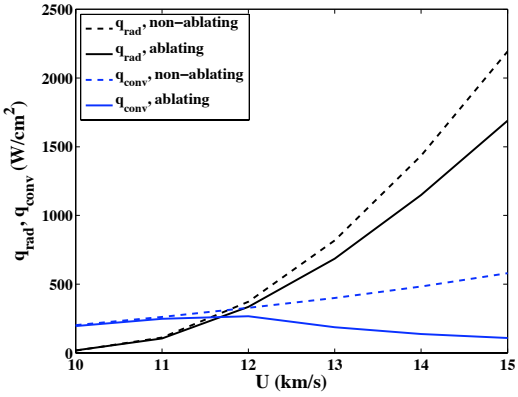

Figure 6: Predicted radiative and convective heating at $z = 3.0$ m of the stagnation point of a 5 m radius sphere.

V. Overview of a Mars-Return Shock-Layer

This section focuses on the 15 km/s, 5 m radius case presented in the previous section, which represents the conservative Mars-return peak heating condition to be studied in the remainder of this paper. Flowfield and radiation details are presented to provide better insight into the strongly coupled radiating and ablating environment. Note that the 5 m radius for this case models the stagnation point shock-standoff distance of an Orion capsule at 22-degrees angle-of-attack.

The stagnation-line temperature profiles for an uncoupled, coupled radiation, and coupled radiation and ablation case are shown in Fig. 7, where the solid line is the translational-rotational temperature and the dashed line is the vibrational-electronic temperature. This figure shows the significant impact of coupled radiation and ablation on the flowfield. Coupled radiation is seen to decease the shock-layer temperature by as much as 4,000 K while decreasing the shock-standoff distance by nearly 20%. The addition of coupled ablation, which assumes steady-state carbon-phenolic ablation, is seen to blow the boundary-layer completely off the wall while increasing the shock-standoff past the uncoupled value.

The stagnation-line pressure profile is shown in Fig. 8 for the coupled radiation case. The value of about 0.65 atm throughout the shock layer is roughly twice the value of 0.3 atm present for Lunar-return cases. This figure also shows the percent ionization along the stagnation-line, which is seen to vary from 32% at the shock to 7% at the boundary layer edge. These values are significantly larger than for Lunar-return cases, where the percent ionization is no greater than 10% throughout the entire layer.

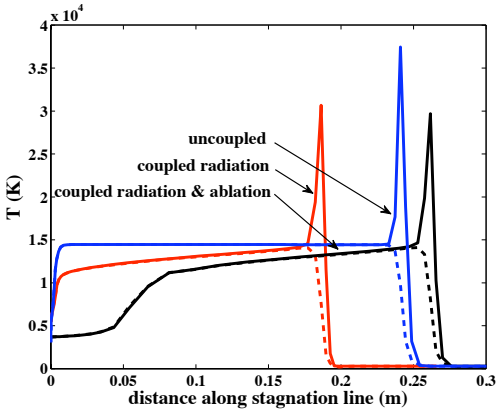

Figure 7: Predicted stagnation-line temperatures for various levels of coupling.

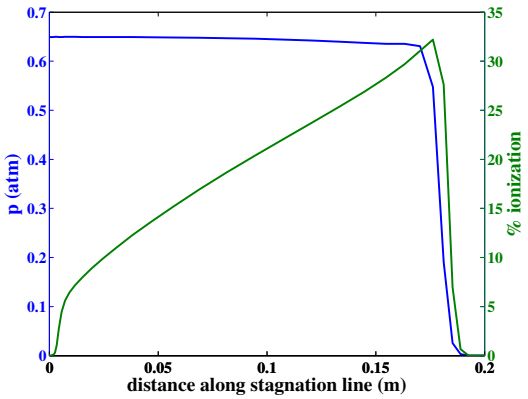

Figure 8: Predicted stagnation-line pressure and percent ionization for the coupled radiation case.

The wall-directed radiative flux along the surface is presented in Fig. 9 for various levels of coupling. This figure illustrates the significance of both radiation and ablation coupling on the radiative heating. Accounting for both coupling phenomena is seen to reduce the radiative heating by 80%, which suggests their treatment is essential to predicting the Mars-return aerothermal environment. This is emphasized further in Fig. 10, which compares the convective heating for various levels of coupling. While radiation coupling reduces the convective heating slightly, the addition of ablation coupling reduces the stagnation region convective heating to nearly zero. It should be noted that convective heating in the stagnation region is an order-of-magnitude smaller than the radiative heating even for the cases without ablation coupling.

The influence of ablation on the stagnation point radiative flux spectrum is presented in Fig. 11, which compares the spectrum for the cases with and without coupled ablation. The red regions of the spectrum represent absorption from ablation products. The absorption in the 2 – 4 eV range is from the C_3 Swings band system, while that in the 5 – 9 eV range is from the C_3 and C_2H UV band systems. In the 10 – 14 eV range, the atomic carbon photoionization contribution along with the numerous CO and H_2 band systems provide significant absorption. As will be discussed in Section VII, significant uncertainty exists for the absorption cross sections of the C_3 and C_2H band systems. These band systems will be shown in Section VIII to contribute significantly to the radiative heating parametric uncertainty.

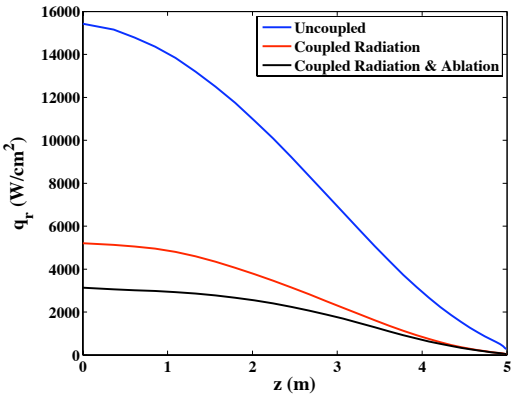

Figure 9: Predicted wall-directed radiative flux values for various levels of coupling.

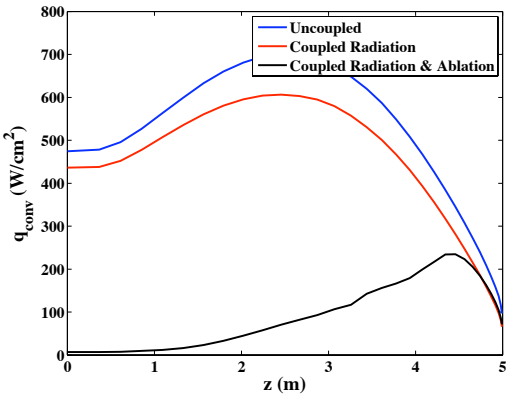

Figure 10: Predicted convective heating values for various levels of coupling.

The relative contribution of atomic line and atomic photoionization processes to the stagnation point radiative flux may be inferred from Fig. 12, which compares the cumulative flux of the full spectrum to those without atomic photoionization or atomic lines included. By comparing the full spectrum result with the case without atomic photoionization ("No Atomic Photo"), it is seen that significant photoionization emission contributes in the 0 – 2 eV range, as well as a slight contribution in the 4 – 6 eV range. Similarly, atomic lines are seen to contribute significanly in the 0 – 3 eV range, with a small contribution in the 9 – 11 eV range. Overall, the atomic line contribution is seen to be slightly larger than the photoionization contribution, although their contributions are the same order-of-magnitude. At lower velocities the relative photoionization contribution is smaller because there is less black-body limiting of the atomic lines.

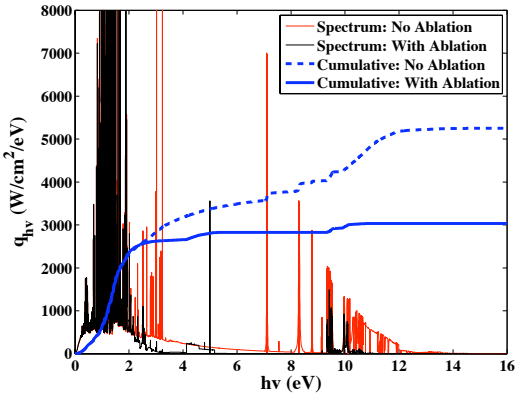

Figure 11: Radiative flux spectrum at the stagnation point for the case with and without ablation.

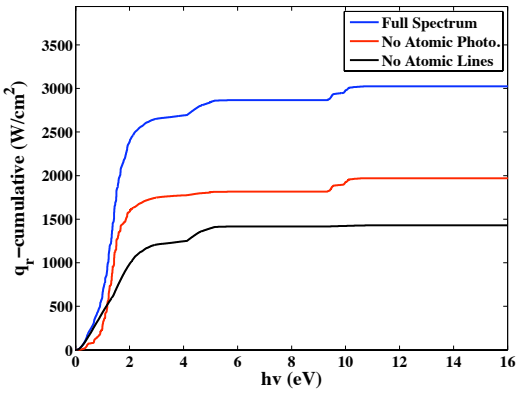

Figure 12: Influence of atomic lines and photoionization on stagnation point radiative flux.

VI. Assessment of Structural Uncertainties

This section reviews the structural (or model form) uncertainties identified to be most significant for a high speed Earth entry. Structural uncertainties refer to uncertainties due to simplifications and inadequacies in the mathematical models applied in the baseline flowfield and radiation simulations.[48] The baseline simulation approach applied in this work was presented in Section III. Note that these baseline simulations include coupled radiation and coupled ablation. The significant influence of these coupled phenomena was presented in Sections IV and V, where they were shown to result in over an 80% decrease in both the radiative and convective heating at Mars-return conditions. These comparisons indicate that coupled simulations are required for the baseline simulations. The baseline

Table 2: Summary of structural uncertainties.

Uncertainty Issue	Uncertainty Value (%) +	-
Turbulence Modeling	+10	-10
Precursor Influence	+20	0
Radiation Transport	0	-10
Grid Convergence	+2	-2
SRB Spectrum of Molec. Bands	+2	-2
Flowfield Diffusion Modeling	0	0
Spallation	0	0
Total	+34	-24

simulation approach also includes the Cebeci-Smith turbulence model and a smeared rotational band radiation model with tangent slab radiation transport. The structural uncertainty issues identified in this baseline simulation approach are summarized in Table 2. Each of these uncertainties are discussed in the following subsections. A structural uncertainty value for each uncertainty issue is identified in these discussions. The resulting structural uncertainty values are also summarized in Table 2, with the total structural uncertainty value being +34 and -24%.

A. Turbulence Modeling

Turbulence has typically been assumed to have a negligible influence on the radiative heating for cases with little or no ablation. However, for cases with massive ablation, such as the present high-speed Mars-return case, this assumption is not necessarily true. The study by Moss et al.[49] for Jupiter entry, which included massive ablation, showed an increase of 30% in the radiative heating for the turbulent case relative to the laminar case. The strong influence of turbulence on radiation was shown by Moss et al. to be a result of the higher temperature inner region of the turbulent boundary layer causing the dissociation of strongly absorbing molecules, therefore resulting in less absorption and a larger radiative flux.

The influence of turbulence on the radiative heating represents a structural uncertainty because of the significant uncertainties present in the turbulence models. These uncertainties include the turbulence model formulation applied (meaning the specific type of algebraic or 2-equation model), the turbulent Schmidt number applied, and whether phenomena such as injection-induced[50] turbulence are included. As mentioned in Section III, the Cebeci-Smith algebraic model with a turbulent Schmidt number of 0.9 is applied as the baseline model for this work. Injection-induced turbulence is not accounted for in this baseline model. This phenomenon was treated by Matsuyama et al.[16] in their analysis of the Galileo probe. They found that injection induced turbulence increased the radiative heating by roughly 5% in the stagnation region. However, the ablation rates for these Galileo results are an order-of-magnitude greater than the present Mars-return cases, which suggests that the influence of injection-induced turbulence for the present cases would be significantly less. Therefore, it may be assumed that injection induced turbulence has a small influence of the present Mars-return cases. This small influence will be accounted for with the ±10% structural uncertainty assigned to turbulence modeling later in this section.

To assess the influence of the present baseline turbulence model, the laminar and turbulent flowfield properties along the body normal downstream of the stagnation point at $z = 3$ m are compared in Figs. 13 - 15. The significant influence of turbulence on the vibrational-electronic temperature is shown in Fig. 13. This figure shows that the low-temperature region near the wall for the laminar case is not present in the turbulent case. This has a large influence on the boundary layer species presented in Fig. 14. For example, the mass fraction of C_3, which is a significant absorber of radiation, is seen to be much smaller for the turbulent case. The reduction of C_3 for the turbulent case results in a 16% greater radiative flux reaching the wall, as shown in Fig. 15. The laminar and turbulent radiative flux values along z are presented in Fig. 16. It is seen that for a significant region downstream of the stagnation point, the turbulent radiative heating is roughly 15% larger than the laminar values.

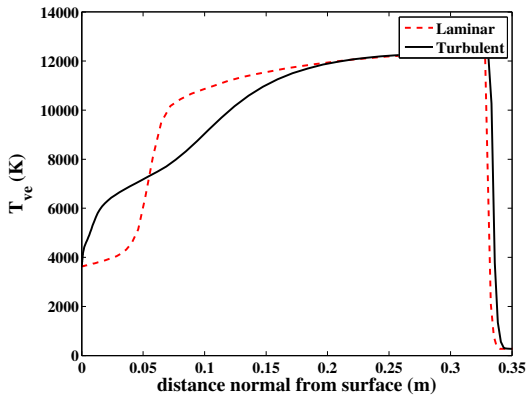

Figure 13: Vibrational-electronic temperature along the body normal at $z = 3$ m for the 15 km/s, 5 m radius case.

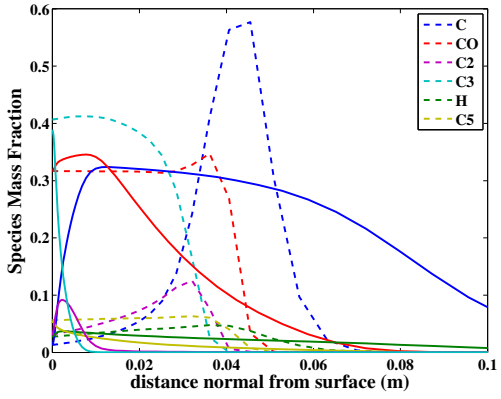

Figure 14: Dominant ablation products along the body normal at $z = 3$ m for the 15 km/s, 5 m radius case. Dashed lines represent the laminar solution while solid lines represent the turbulent.

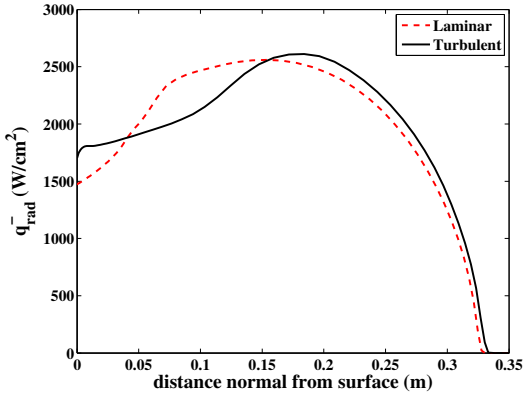

Figure 15: Wall-directed radiative flux along the body normal at z = 3 m for the 15 km/s, 5 m radius case.

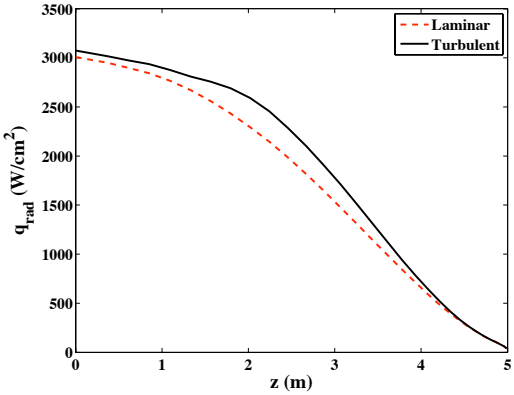

Figure 16: Radiative flux along the surface for the 15 km/s, 5 m radius case.

To assess the influence of turbulent Schmidt number on the radiative heating, Fig. 17 compares the radiative heating for turbulent Schmidt numbers of 0.5, 0.9, and 1.3. It is seen that increasing or decreasing the turbulent Schmidt number away from the baseline value of 0.9 results in less than a 3% change in the radiative heating. Figure 18 shows that a slightly larger percentage change in the convective heating is obtained for different turbulent Schmidt numbers, however the magnitude of the convective heating relative to the radiative heating makes this difference negligible.

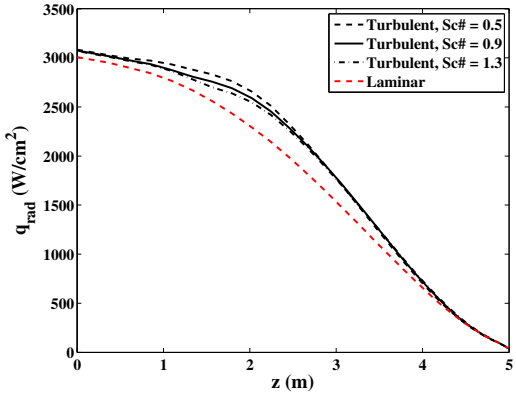

Figure 17: Radiative flux along the surface for the 15 km/s, 5 m radius case.

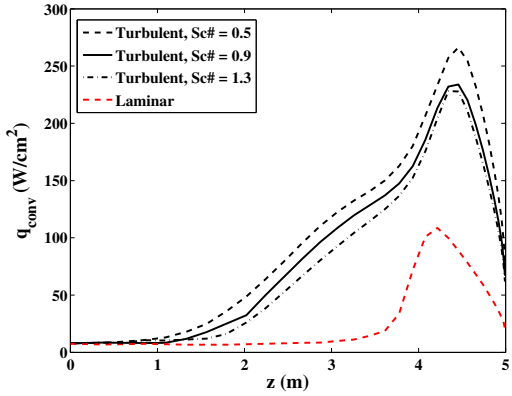

Figure 18: Convective flux along the surface for the 15 km/s, 5 m radius case.

Although the present baseline flowfield model accounts for the influence of turbulence on the radiative heating, the approximate nature of the algebraic turbulence model applied introduces uncertainty to the predictions. This structural uncertainty to account for the influence of turbulence model uncertainties on the radiative heating is assigned as ±10%. This accounts for the influence of turbulent Schmidt number and the formulation of the algebraic turbulence model.

B. Precursor Influence

The purpose of this section is to investigate the influence of free-stream radiative absorption on the flowfield structure and associated aerothermodynamic environment at hyperbolic Earth entry conditions. The study of this effect, typically referred to as the precursor effect, has been the subject of several previous studies for air shock layers.[51–58] Some of these studies[51–53,55,57] assumed thermochemical equilibrium throughout the shock layer and precursor region, which implies a single temperature model and chemical equilibrium throughout the flowfield. Radiation influences a thermochemical equilibrium flowfield through the presence of the divergence of the radiative flux in the energy equation. This is the term commonly treated in "coupled radiation" flowfield computations[34,59] for both thermochemical equilibrium and nonequilibrium flowfields. A number of studies[54,56,58] have applied thermochemical nonequilibrium models throughout the shock layer and precursor region. The influence of radiation on these nonequilibrium flowfields is accounted for through not only the divergence of the radiative flux, but also through the photochemical production

term in the species continuity equations. This term is required to treat the creation and destruction of species through photodissociation and photoionization. The work of Stanley and Carlson[56] represents the most recent detailed study of this phenomenon. They studied nitrogen flowfields using a viscous shock layer analysis. Details of the photochemical production terms was provided as well as modifications required for the tangent slab radiation transport in the precursor region. To examine the potential impact of the precursor effect on Mars-return cases, the photochemical production terms were added to LAURA following the approach of Stanley and Carlson. The absorption cross sections for the photoionization and photodissociation of O_2, which were not treated by Stanley and Carlson, were taken from Romanov et al.[60] The cross sections for N_2 applied by Stanley and Carlson were applied here, while the photoionization cross sections for N and O were taken from the TOPbase.[61]

The 15 km/s, 5 m radius Mars-return case was studied using the precursor treatment discussed in the previous paragraph. To simplify the analysis, ablation coupling is not included in these results. The vibrational-electronic temperature throughout the flowfield is presented in Fig. 19. A vibrational-electronic temperature greater than 1,000 K is seen to extend about one body radius from the surface around the sphere. In the stagnation region, this temperature nearly reaches the post-shock level as the shock is approached. This is shown more clearly in Fig. 20, which presents the stagnation line temperature profiles. In this figure, the bow shock is at 0.2 m on the horizontal axis. The vibrational-electronic temperature is seen to approach 13,000 K just before the shock, while the translational-rotational temperature remains at the free-stream value. The density is too low in the precursor region for the energy relaxation terms to begin to equilibrate the two temperatures. The divergence of the radiative flux therefore influences only the vibrational-electronic temperature.

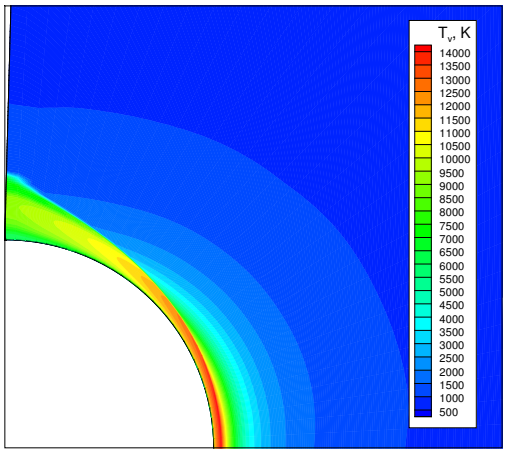

Figure 19: Vibrational-electronic temperature in the flowfield, including the precursor, for the 15 km/s, 5 m radius case.

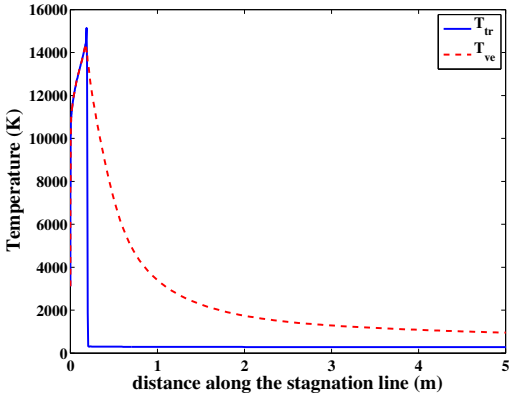

Figure 20: Temperatures along the stagnation line, including the precursor, for the 15 km/s, 5 m radius case.

The O_2 mass fraction throughout the flowfield is presented in Fig. 21. The shock layer is seen as the completely dissociated region near the body. In the stagnation region, the precursor influence is seen to reduce the O_2 mass fraction entering the shock layer from the ambient value of 0.24 to roughly 0.15. The reduction in O_2 in the precursor is due primarily to photodissociation, although O_2 photoionization is not negligible. The influence of photoionization and photodissociation may be seen in Fig. 22, which presents the species number densities along the stagnation line. The dissociation of O_2 into O is clearly seen, while the dissociation of N_2 is indicated by the rise of N. The precursor influence reduces the N_2 mass fraction entering the shock layer from 0.76 to only about 0.74 in the stagnation region, which is much less dissociation than that seen for O_2. The influence of photoionization processes are indicated by the presence of ionized species in the precursor. The most abundant ion in the precursor is seen to be O_2^+, which is followed surprisingly by NO^+. Note that collisional chemical reactions are responisble for the creation of NO and NO^+ in the precursor. These collisional reactions also have a influence on other species, although it is typically overshadowed by the photochemical contribution.

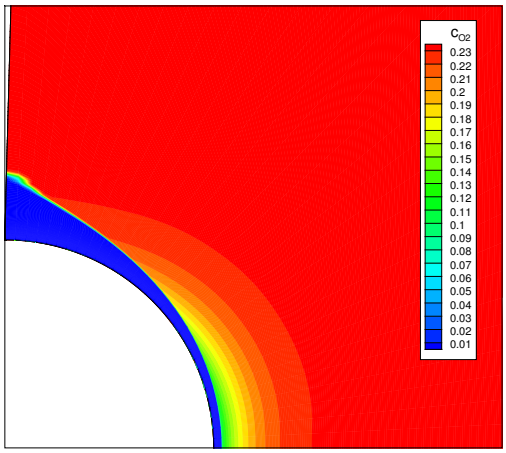

Figure 21: Mass fraction of O_2 in the flowfield, including the precursor, for the 15 km/s, 5 m radius case.

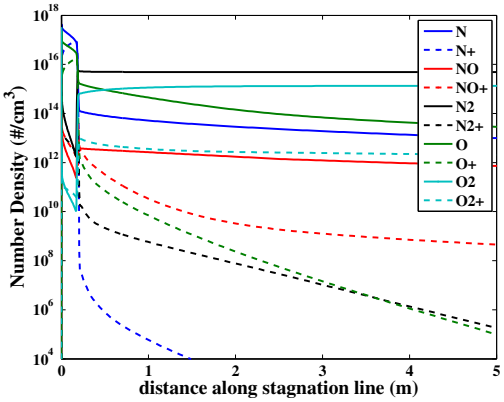

Figure 22: Number densities along the stagnation line, including the precursor, for the 15 km/s, 5 m radius case.

The strong precursor influence on the flowfield temperature and number densities shown in Figs. 19 - 22 is a result of strong radiative absorption in the free-stream. The magnitude of this absorption is indicated in Fig. 23, which presents the free-stream directed intensity profile along the stagnation line. The emission from the shock layer is apparent below 0.2 m on the horizontal axis, while beyond this point the negative slope of the curve represents absorption in the precursor. Figure 24 presents the intensity spectrum at the shock (red curve) and outer free-stream boundary (blue curve). The difference between these curves represents the total precursor absorption. It is clear that this absorption occurs exclusively in the vacuum ultraviolet (VUV) region of the spectrum ($h\nu > 6$ eV). Note that nearly all of the VUV radiation emitted from the shock layer is absorbed in the precursor.

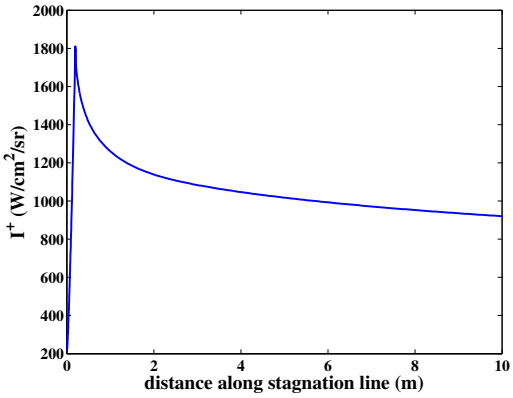

Figure 23: Radiative intensity directed along the stagnation line away from the body for the 15 km/s, 5 m radius case.

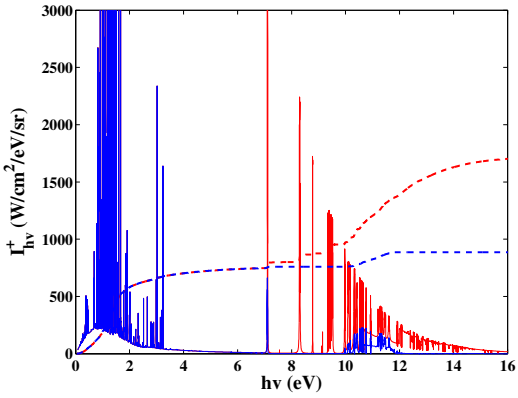

Figure 24: Radiative intensity spectrum directed away from the body at the shock (red) and outer boundary (blue).

The primary reason for modeling the precursor is to account for its influence on the shock layer radiative heating, which is strongly dependent on the shock layer temperatures. Figure 25 compares the vibrational-electronic temperature for a case with and without the treatment of the precursor (the figure is focused on the shock-layer, the rest of the precursor is the same as that in Fig. 20). The temperature difference in the shock layer between the two cases is roughly 150 K. Although this difference may appear small, the radiative heating heating is extremely sensitive to the temperature: The 1% increase in the shock layer temperature results in a 15% increase in the radiative flux reaching the wall. This result is shown in Fig. 26, which compares the wall directed radiative flux for the case with and without the precursor influence. The 15% increase due to the precursor confirms the importance of this phenomenon for modeling Mars-return radiative heating.

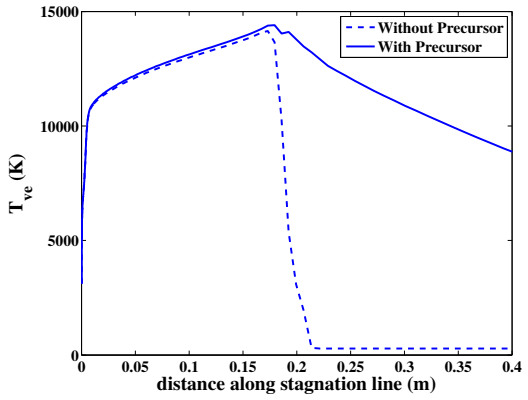

Figure 25: Vibrational-electronic temperature along the stagnation line close to the wall for the case with and without precursor modeling.

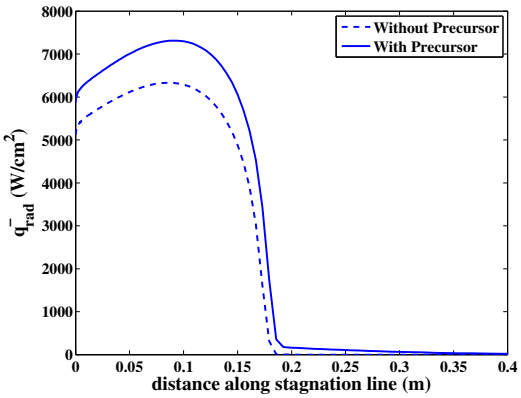

Figure 26: Wall directed radiative flux along the stagnation line close to the wall for the case with and without precursor modeling.

The analysis presented here on the influence of the radiative precursor on Mars-return radiative heating is relatively preliminary. Further work on this subject is certainly required to provide confidence in the modeling of the precursor. The +15% increase in the radiative heating predicted with this preliminary model could be increased by another 5% by differing the molecular photoionization and photodissociation cross sections to values proposed in the literature. However, the precursor influence could also be made negligible with other choices of these parameters (although note that the precursor never decreases the radiative heating). As a result, a +20%, -0% uncertainty is assigned to account for the precursor influence on the radiative heating for the 15 km/s case. Note that the precursor influence is strongly dependent on velocity. It was found that this uncertainty should be linearly reduced to a value of zero at 11 km/s.

C. Three-Dimensional Radiation Transport

Shock-layer radiation transport is typically computed using the tangent-slab approximation.[47,62] This approach is applied in the present baseline LAURA/HARA simulations, as well as the majority of other state-of-the-art shock-layer radiation predictions.[63,64] The quality of the tangent-slab approximation has been the subject of studies by Hartung and Hassan[65] and Matsuyama et al.[16] Hartung and Hassan considered relatively weakly radiating cases, which contained mostly optically thin radiation. They showed that the tangent-slab predictions were 5–15% greater than the three-dimensional transport predictions. Matsuyama et al. considered strongly radiating conditions similar to the present Mars-return conditions. They showed that the tangent-slab predictions were 7% greater than the three-dimensional transport predictions. The smaller difference for this case is expected because the radiation is more optically thick than the cases studied by Hartung and Hassan.

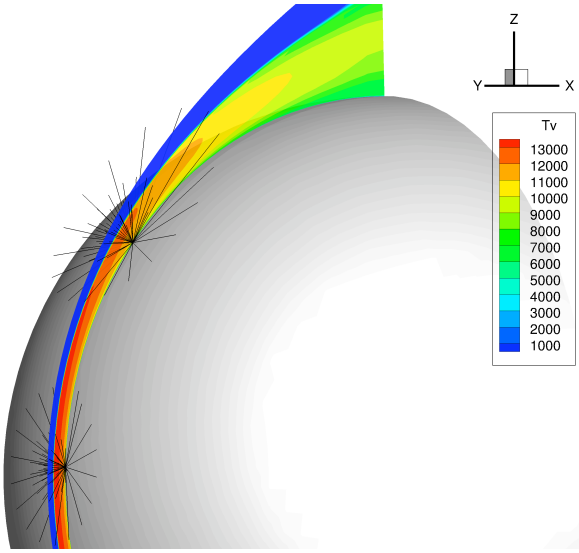

Figure 27: Rays applied for the radiative flux computation at the stagnation point and $z = 3$ m.

A 3D ray-tracing algorithm has been incorporated into the LAURA/HARA analysis. The relative efficiency of the HARA radiation code (assuming the use of the SRB model for molecular bands) makes the ray-tracing approach feasible. This is especially true if the ray-tracing approach is used only to compute the radiative flux at the surface, therefore retaining the tangent-slab approach to provide the radiative flux divergence at the potentially thousands of flowfield points. Using the tangent slab approach for the radiative flux divergence should introduce only second-order inaccuracies in the radiative flux reaching the surface,[66] whereas the tangent-slab approximation for computing the surface radiative flux introduces the 5 – 15% inaccuracies

cited in the previous paragraph.

The present ray-tracing approach integrates the following radiative flux equation at the surface

$$q_{h\nu} = \int_0^{2\pi} \int_0^{\pi/2} I_{h\nu}(\theta, \phi) cos\theta sin\phi d\theta d\phi \tag{3}$$

where θ is the angle of the ray from the body normal and ϕ is the angle of the ray around the body normal. In the numerical evaluation of this equation, the radiative intensity rays, $I_{h\nu}$, are computed at discrete values of θ and ϕ. Convergence studies found that 20-degree increments in θ and 20-degree increments in ϕ are sufficient for evaluating Eq. 3. The interpolating algorithm applied in extracting flowfield data for the radiative transfer computation of each ray has the ability to extrapolate data from axisymmetric flowfields (where only a single "pie slice" of the flowfield is simulated). This capability enables ray-tracing solutions of the present axisymmetric flowfields. A level of validation for this ray-tracing approach was achieved by applying it to a tangent-slab geometry and showing that the analytical tangent slab result was reproduced within 2%.

To assess the uncertainty introduced by assuming tangent-slab radiation transport in the present baseline radiation model, the ray-tracing algorithm discussed in the previous paragraph was applied to the 15 km/s, 5 m radius Mars-return case. For simplicity, the case without ablation was considered. The rays applied for this computation at the stagnation point and downstream at $z = 3$ m are shown in Fig. 27. The non-tangent-slab nature of the flowfield is especially apparent at the downstream point for many of the rays nearly parallel to the body. The wall-directed radiative flux spectra computed by the ray-tracing and tangent slab approaches are compared in Figs. 28 and 29 for the stagnation point and $z = 3$ m, respectively. These figures show that the tangent slab approach predicts about a 10% larger radiative flux than the ray-tracing approach. This result is consistent with those of past studies mentioned earlier. Note that most of the difference between the ray tracing and tangent slab predictions occurs from atomic lines in the 1 – 2 eV range.

As a result of the present computations applying the tangent-slab approximation, an uncertainty of +0%, -10% is assigned to account for this approximation. Only a negative uncertainty is applied here because in all studies the tangent slab approximation, which is applied in the present baseline model, was found to over-predict the radiative heating. The preliminary nature of the present ray-tracing approach, as well as those presented in the literature, allows this -10% to be considered an uncertainty and not just a bias (which could be accounted for by multiplying the baseline prediction by a factor 0.9). Further studies of ray-tracing approaches are required to gain confidence in their predictions. Once this confidence is gained, the tangent-slab radiative heating may be multiplied by an appropriate correction factor (such as 0.9) and the present +0%, -10% uncertainty may be removed.

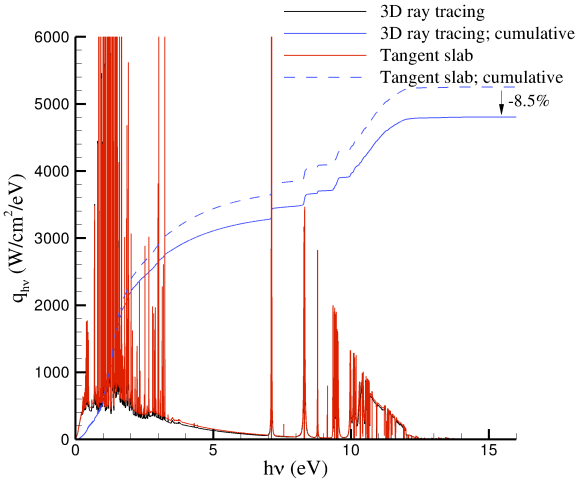

Figure 28: Comparison of ray-tracing and tangent slab radiative flux at the stagnation point.

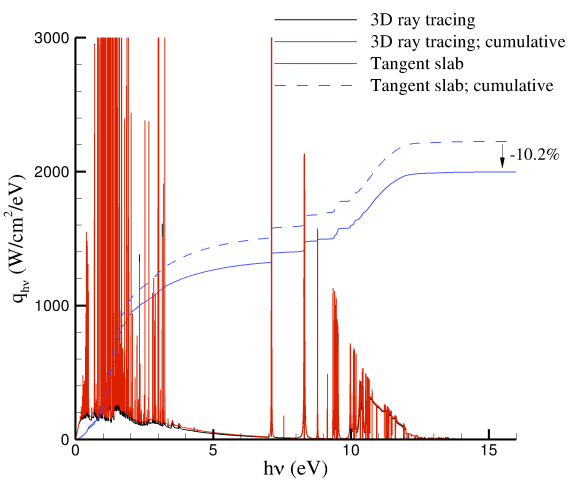

Figure 29: Comparison of ray-tracing and tangent slab radiative flux at $z = 3$ m.

D. Grid Convergence

The grid applied in the present study consisted of 64 points normal to the body. If grid points are clustered around the shock, these 64 points have been found to provide a grid converged radiative heating solution for cases without massive ablation. For the present cases, which do contain massive ablation, more grid points may be required to resolve the ablation zone that sits away from the wall. To check that 64 points was sufficient to model the radiative heating for the present 15 km/s case with massive ablation, a case was run with 128 points normal to the body. A comparison between the 64 and 128 point solutions is made in Fig. 30 for the dominant ablation species in the ablation zone. It is seen that the 128 point grid provides better resolution of many of the sharp gradients, although the overall magnitudes of the species are similar. The difference between the stagnation line wall directed radiative flux resulting from the 64 and 128 point grids is presented in Fig. 31. A slight difference is seen near the shock at 0.25 m and near the boundary layer at 0.05 m. These two differences are less than 2% each and offset one another to provide a wall flux with a difference of 0.5%. As a result of this close agreement, a ±2% uncertainty will be assigned to the structural uncertainty to account for grid convergence. Note that it is very computationally expensive to run this fine grid, especially with the 26 flowfield species presently treated, which is why the 64 point grid was chosen as the baseline.

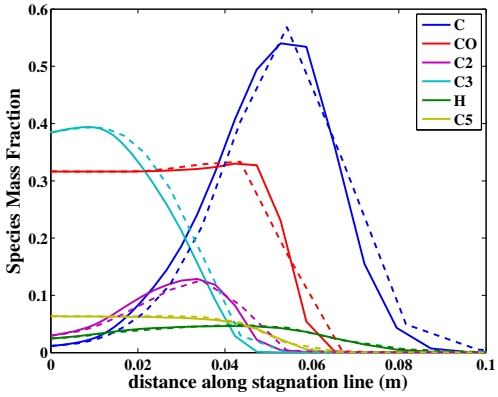

Figure 30: Stagnation-line species mass fractions for dominant ablation products in boundary layer for 64 (dashed curve) and 128 (solid curve) point grids.

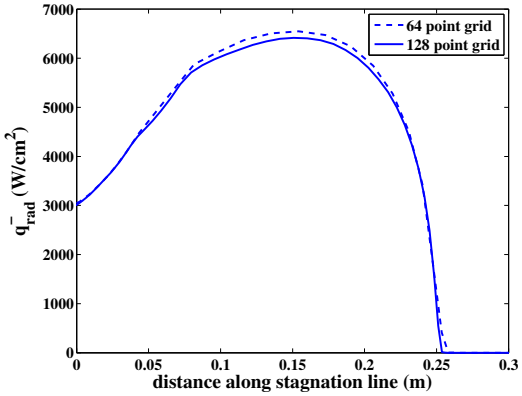

Figure 31: Wall directed radiative flux along stagnation line for 64 and 128 point grids.

E. Smeared Rotational Band Spectrum Modeling of Molecular Bands

As discussed in Section III, the HARA radiation code implemented in the present study applies the smeared rotational band (SRB) method for the spectrum modeling of diatomic molecular band systems.[46] This approach is known to be accurate for optically thin band systems, which makes it appropriate for modeling emitting band systems in high temperature air. However, for strongly absorbing VUV band systems in an ablation contaminated boundary layer, there is potential for the SRB approach to introduce inaccuracies into the radiative flux computation. The rigorous line-by-line (LBL) approach has recently been added to the HARA code. This approach requires many orders-of-magnitude more computational time than the SRB approach, which makes its application to radiation coupling more difficult.

To determine the uncertainty introduced by applying the SRB approach, comparisons were made between the SRB results and the recently added LBL capability in HARA. Using the coupled radiation and ablation flowfield obtained for the 5 m radius sphere at 15 km/s, the stagnation line radiative heating was computed using the SRB and LBL approaches. The exact same energy level and transition data were applied for both cases. The radiative flux spectrum at the wall predicted for both cases is presented in Fig. 32. Differences between the SRB and LBL approaches exist wherever the blue spectrum curve is seen. These differences are most apparent between 2 – 3 eV, which represents absorption from the C_2 Swan band, and above 9 eV, which contains CO, H_2, and N_2 band systems. As mentioned previously, the SRB is known to be inaccurate in regions of strong absorption. Previous studies[46] have shown, however, that this inaccuracy results in less than a 3% inaccuracy in the integrated radiative flux for air shock layers. This trend is confirmed by the cumulative flux curves in Fig. 32, which show a difference in the integrated flux of 2%. This good agreement is a result of the SRB approach's ability to closely model the vibrational band shapes without the rotational

structure. To examine the region above 9 eV, where much of this difference occurs, Fig. 33 provides a focused look at the 9 – 12 eV range. In this figure the individual rotational lines are merged into a solid blue area, so it is difficult to visualize the integrated contribution for the LBL spectrum. The majority of the deviation seen between 10 and 11.2 eV is a result of the SRB approach over-predicting the absorption. Note that the disagreement of 40 W/cm^2 seen in this figure represents only a 1.3% difference in the total radiative flux. The cumulative flux resulting from ignoring all molecular band absorption is shown in the "No Bands cumulative" curve in Fig. 33. Comparing this result with the LBL and SRB curves indicates the significant amount of absorption provided by the molecular band systems, and it confirms the relative success of the SRB approach in modeling absorption in this optically thick environment.

From the comparison presented in this section, a ±2% structural uncertainty will be assigned to account for using the the SRB approach for the baseline radiative heating predictions. It should be emphasized that even with the LBL capability available in HARA, it is extremely advantageous to retain the SRB approach for the baseline predictions. The SRB approach requires roughly 30 seconds per line-of-sight, while the LBL approach requires roughly 6 hours (using a single processor).

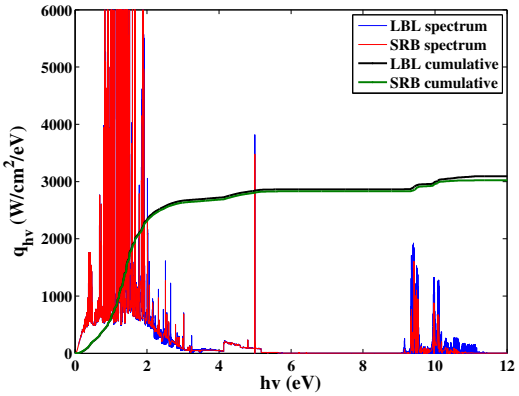

Figure 32: Comparison between LBL and SRB radiative flux spectrum at the stagnation point.

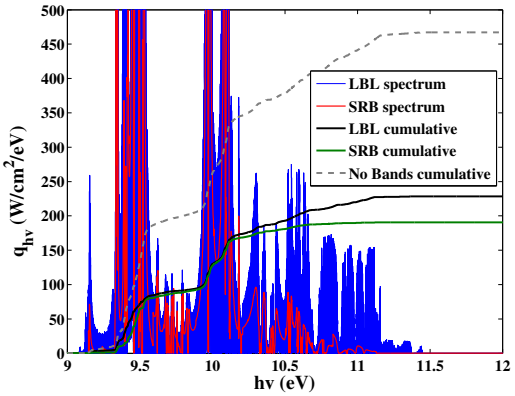

Figure 33: Comparison between LBL and SRB radiative flux spectrum at the stagnation point, with focus on VUV.

F. Spallation

The ejection of solid particles from the ablator surface into the flow, or spallation, may introduce an additional source of radiative heating if the solid particles reach the high-temperature inviscid region of the shock layer.[67] Spallation will occur if the combined radiative and convective heating rate is above a material-dependent threshold. For the carbon-phenolic heat shield presently considered, Lundell[68] finds that spallation occurs for heating rates above 14.5 kW/cm^2. Because the present heating rates are less than 4 kW/cm^2, it may be assumed that spallation does not occur and may be ignored. If an ablator other than carbon-phenolic is considered, such as PICA,[69] this assumption may not be appropriate.

G. Flowfield Diffusion Modeling

Several issues regarding diffusion modeling were investigated to assess their potential impact on radiative heating at the conditions of present interest. These issues are discussed in the following subsections. As will be discussed, no additional structural uncertainty will be assigned to account for these diffusion modeling issues.

1. *Rigorous Stefan-Maxwell Diffusion Modeling*

The "approximate-corrected" diffusion model proposed by Sutton and Gnoffo[70] is typically applied for aerothermodynamic simulations, and it is applied in the present study. This model has been shown to produce q_{conv} values that compare well with the exact model provided by the Stefan-Maxwell equations.[71,72] The species compositions through the boundary layer predicted by the approximate-corrected approach, however, may be noticeably different than the Stefan-Maxwell result.[40,73] These differences in the species compositions have the potential to influence the radiative heating, especially for the strongly ablating case of present interest where ablation strongly influences the radiative heating. To investigate this issue, the

present 15 km/s case with coupled ablation and radiation was computed using the Stefan-Maxwell diffusion model. This model is not typically applied because it is significantly more computationally expensive than the "approximate-corrected" model. A less than 1% change in the radiative heating was found to result from applying the rigorous Stefan-Maxwell model. Therefore, no structural uncertainty is assigned to account for this issue.

2. Ambipolar Diffusion

The ambipolar diffusion is typically applied to model the diffusion of ions in a partially-ionized flow. It assumes that each ion diffuses as if it were the only ionic species in the mixture. The ionization level for the present cases may be as high as 30%, as shown in Fig. 8. This significant ionization level may represent the upper applicability limit of theories and methods appropriate for a "partially ionized" gas, such as the ambipolar diffusion assumption. Although an approach for ionic diffusion modeling of strongly gases is not presently available to assess the impact of the ambipolar diffusion assumption on the present cases, the influence of the ionic diffusion model on the radiative heating may be assessed by removing the ambipolar diffusion assumption (and therefore treating ions in the same manner as neutral species). Such an analysis was performed for the 15 km/s case with coupled ablation and radiation. It was found that the radiative heating was influenced by less than 1% by the removal of the ambipolar diffusion assumption. As a result, no structural uncertainty is assigned to account for this issue.

3. Collision Cross-Section Uncertainties

The collision cross-section data required for computing the flowfield transport properties contain significant uncertainty for many of the collision processes. These uncertainties have been compiled and discussed by Wright et al.,[36,37] among others. The influence of these uncertainties was assessed by computing the flowfield for the 15 km/s case (with coupled ablation) with the cross-section values adjusted to the uncertainty limits proposed by Wright et al.. The resulting radiative heating value was within 1% of the baseline value, thus showing the insensitivity of the radiative heating to the collision cross sections. As a result, no structural uncertainty is assigned to account for this issue. Note that this issue could be included in the discussion of parametric uncertainties in Section VII, however it is included here to accompany the other diffusion modeling issues.

VII. Parametric Uncertainty Analysis

This section discusses the details of the present parametric uncertainty analysis and then presents a review of the actual uncertainties chosen for the modeling parameters. Parametric uncertainties in both the radiation and flowfield code are considered in this study.

A. Overview of Approach

The parametric uncertainties of interest in this study are those due to lack of knowledge, also known as epistemic uncertainties, as opposed to those due to chance, or aleatory uncertainties.[74] An interval analysis, which involves finding the upper and lower limit of the function of interest within the given parameter uncertainty limits, is appropriate for a problem with all epistemic uncertainties. This type of analysis is fundamentally different than the often mistakenly applied Monte-Carlo-type analysis, which is appropriate for a case with all aleatory uncertainties. The interval analysis produces significantly larger uncertainties than the Monte-Carlo analysis because it seeks out the upper and lower limit of the function of interest, which likely occurs far out (far beyond a couple standard deviations) on the gaussian distribution produced by a Monte-Carlo analysis.

The type on interval analysis applied in this work is simplified by the fact that the parametric uncertainties of interest are essentially independent of one another, the radiative heating varies monotonically with each parameter (within the parameters uncertainty bounds), and the cost of a HARA radiation computation is relatively small. As a result, the plus and minus uncertainty contribution of each parameter may be determined by computing the radiative flux with the parameter of interest changed to its upper and lower limits, while the other parameters remain at their baseline value. The change in the radiative heating produced by these two computations are then added to the total plus or minus uncertainty depending on the

sign of the deviation. Although this approach is inefficient relative to other techniques,[75] it is conceptually very simple and produces results that are easy to interpret. The remainder of this section discusses the actual parametric uncertainties applied in this work.

B. Uncertainty in Radiation Properties for Air

An uncertainty analysis of the radiative heating from air shock-layers was performed by Kleb and Johnston.[28] The same parameter uncertainties applied in that study were applied here. Kleb and Johnston[28] provide a detailed discussion of their uncertainty choices, so only a brief discussion is provided here.

1. Molecular Band Systems for Air

The most significant emitting molecular band system in air at the present conditions is the N_2^+ first-negative system. The oscillator strength uncertainty for this band system is chosen as $\pm 10\%$, following comparisons by Langhoff and Bauschilcher.[76] Following Laux and Kruger,[77] the uncertainties for the N_2 first-positive, N_2 second positive, and all NO band systems are chosen as $\pm 10\%$. For the N_2 VUV bands systems[46] (Birge-Hopfield, Worley, Worley-Jenkins, and Carroll-Yoshino), an uncertainty of $\pm 50\%$ is chosen based on the comparisons presented by Stark et al.,[78] Chan et al.,[79] Appleton and Steinberg,[80] and Carter.[81]

2. Atomic Lines for Air

The atomic line model applied in HARA for air is discussed in detail by Johnston et al.[46] A brief review of this model, focused on the model uncertainty, is provided here. For the strongest lines of nitrogen and oxygen, the available data for oscillator strengths and Stark broadening widths were assessed by Johnston et al.[46] and uncertainty values were proposed. These uncertainties, for the oscillator strength (f_{ij}) and Stark broadening width ($\Delta\lambda_{S,0}$), are listed in Tables 3 and 4 for the strongest nitrogen and oxygen line multiplets. The choice of these uncertainties will be discussed in the following paragraphs.

For lines not listed in Tables 3 and 4, the f_{ij} uncertainties proposed by Wiese et al.[82] were applied for the NIST lines. The $\Delta\lambda_{S,0}$ uncertainties for lines not listed in Tables 3 and 4 were assumed equal to $\pm 50\%$ if the $\Delta\lambda_{S,0}$ value was taken from Griem[83] or Wilson and Nicolet.[84] Otherwise, the $\Delta\lambda_{S,0}$ value was obtained from an approximate correlation[46] and the $\Delta\lambda_{S,0}$ uncertainty was set to $\pm 100\%$.

The theoretical[85,86] and experimental[87–91] data collected to determine these oscillator strength uncertainties are presented in Figs. 4 and 5 of Johnston et al.[46] for nitrogen multiplets 1–14 and 15–33, respectively. As discussed by Johnston et al.,[46] the present uncertainties were chosen based on the deviation of the post-1970 data from the Wiese et al. (1996) values[82] (therefore neglecting the Wiese et al. (1966) data[92] and Wilson and Nicolet (1967) data[84]). However, for the multiplets with only the Wilson and Nicolet (1967)[84] and Wiese et al. (1996) values[82] available (multiplets 1, 2, 4 and 5), the difference between these two values were used in the uncertainty determination. The presently chosen uncertainties are generally higher than those proposed by Wiese et al. (1996), although a few remain the same. A minimum uncertainty of $\pm 10\%$ was chosen because no experimental measurement contained an uncertainty lower than this value. The uncertainties listed in Table 4 for oxygen lines are taken directly from Wiese et al. (1996).

The experimental[93–98] and theoretical data collected to determine the $\Delta\lambda_{S,0}$ uncertainties are shown in Fig. 6 of Johnston et al.[46] for the multiplets listed in Table 3. For the multiplets with only the Wilson and Nicolet values available, an uncertainty of $\pm 75\%$ was assigned based on the comparison with other multiplets, while for the cases with "no data", an uncertainty of $\pm 100\%$ was conservatively chosen. For the multiplets with various measurements available it is noted that, except for multiplets 7, 9, 12, and 14, the measurement uncertainties overlap the averaged value as well as the baseline values from the other measurements and predictions. Considering this, the uncertainty was chosen to capture the baseline values, relative to the average, from all the measurements and theoretical results.

3. Atomic Photoionization Cross Sections for Air

Recent theoretical predictions by various researchers of nitrogen[99–101] and oxygen[102,103] photoionization cross sections (σ_{bf}) agree within 10% of each other. However, the comparison of predictions with actual measurements[104–108] is much worse, with the agreement ranging from 30–50%. A complication in the analyses of the measurements is the possible influence of the negative nitrogen ion, which provides an increase in the continuum radiation. The uncertain magnitude of the negative nitrogen ion cross section, which will be

Table 3: Strongest nitrogen line multiplets.

multiplet number	Wiese ID*	$h\nu$ (eV)	$\lambda_{CL,mult}$ (nm)	$\pm f_{ij}$ (%)	$\pm\Delta\lambda_{S,0}$ (%)
1	24	11.61	106.80	75	75
2	23	11.29	109.77	75	75
3	19	10.62	116.79	50	40
4	17	10.53	117.69	50	40
5	39	10.42	118.91	75	75
6	38	10.41	119.10	75	75
7	1	10.33	120.00	20	50
8	37	10.12	122.52	75	75
9	16	9.972	124.32	20	100
10	35	9.459	131.07	60	30
11	32	9.396	131.95	20	30
12	30	8.781	141.19	20	100
13	15	8.302	149.33	10	30
14	29	7.110	174.36	20	50
15	48	1.663	745.42	10	30
16	47	1.509	821.41	10	30
17	52	1.438	861.98	10	30
18	46	1.426	869.40	15	30
19	65	1.369	905.24	25	30
20	127	1.369	905.01	15	30
21	126	1.347	919.82	50	100
22	51	1.319	939.79	25	50
23	72	1.260	983.33	15	50
24	70	1.241	998.70	25	100
25	71	1.240	999.10	75	100
26	69	1.225	1011.7	10	50
27	80	1.158	1070.0	75	75
28	81	1.177	1052.6	10	75
29	68	1.098	1128.9	15	75
30	61	1.068	1160.0	25	100
31	100	1.029	1204.4	10	100
32	99	0.994	1246.9	15	100
33	114	0.910	1362.0	10	100

* Multiplet number listed by Wiese et al.[82]

Table 4: Strongest oxygen line multiplets.

multiplet number	Wiese ID*	$h\nu$ (eV)	$\lambda_{CL,mult}$ (nm)	$\pm f_{ij}$ (%)	$\pm\Delta\lambda_{S,0}$ (%)
1	2	9.51	130.35	3	50
2	56	1.59	777.55	3	50
3	60	1.47	844.88	10	50
4	64	1.34	926.64	3	50
5	78	1.09	1128.7	3	50

* Multiplet number listed by Wiese et al.[82]

discussed later, makes it difficult to subtract out of the continuum measurement to obtain the photoionization contribution. As a tradeoff between the consistency of the theoretical predictions and the poor agreement with the measurements, which depends on how the negative ion is treated, an uncertainty of ±20% is chosen for all the photoionization cross sections of nitrogen and oxygen.

4. Negative Ion Photodetachment Cross Sections for Air

As a result of the few theoretical predictions available[109–111] and the difficulty mentioned previously in obtaining cross sections from experimental data[112] (due to the overlapping photoionization contribution), there is significant uncertainty in the negative ion continuum cross section (σ^-).[113] From the wide spread in proposed cross sections, an uncertainty of ±100% is chosen for the negative nitrogen ion. The nominal σ^- values applied in HARA are presented by Johnston et al.[46] The lower limit of the ±100% uncertainty represents neglecting the negative ion contribution entirely.

C. Uncertainty in Radiation Properties for Ablation Products

The molecular band and atomic photoionization contributions from ablation products have a relatively significant influence on the radiative heating for Mars-return cases. The atomic line and negative ion photodetachment contributions from ablation products, however, are negligible. Therefore, the following discussion will focus exclusively on the uncertainties for the molecular band and atomic photoionization radiation.

Table 5: Oscillator strength uncertainties for molecular band systems resulting from ablation products.

Band System	+/- Uncertainty
CO Fourth-Positive[114,115]	40%
CN Red[114,115]	30%
CN Violet[114,115]	15%
C_2 Swan[114,115]	50%
C_2 Ballik-Ramsay[114–117]	50%
C_2 Phillips[114,115]	50%
C_3 Swings[118–120]	$O(1)$ mag.
C_3 UV[118–120]	$O(1)$ mag.
C_2H UV[118–120]	$O(1)$ mag.
H_2 Lyman[121–123]	10%
H_2 Werner[121–123]	20%

1. Molecular Band Systems for Ablation Products

Recent reviews of molecular band system data for a CO_2-N_2 gas[114–117] provide valuable insight into the uncertainties for many of the bands systems resulting from diatomic ablation products. Comparisons between experimental measurements and various predictions for the oscillator strengths for the C_2 and CO molecules are made in these papers. These comparisons are used to determine the uncertainties applied in the present work for C_2 and CO, which are listed in Table 5. Note that these uncertainties are relatively large and range from 15 to 50%.

One of the most significant absorbers in the ablation-contaminated boundary layer is the C_3 Swings band system. The three existing measurements of this band system [118,119,124] result in absorption cross sections with peak magnitudes within 50% of each other (if the updated thermodynamic data is applied when backing out the cross-section[125]). However, these measurements were all for temperatures below 4000 K, and the wavelength span of each measured cross-section varied significantly. Because of these two factors, the C_3 Swings absorption cross section was assigned a one order-of-magnitude uncertainty in this analysis.

The C_3 UV band system has been measured by Shinn[120] and computed by Arnold et al.[126] The measurements by Shinn are roughly an order-of-magnitude greater than the predictions of Arnold et al. Because of this, the C_3 UV absorption cross section was assigned a one order-of-magnitude uncertainty in this analysis.

Table 6: Heat of formation uncertainties for some ablation products.

Molecule	$\Delta_f H(0)$ (kJ/mol)	+/- Uncertainty (%)
CN	437.0	1.14
C_2	822.4	1.22
C_3	831.0	1.56
C_2H	565.0	1.10

The C_2H UV band system has been measured by Shinn[120] and Prakash et al.[119] The influence of Mie scattering on the interpretation of these data has been questioned by Arnold et al.[126] Because of this question and the scatter in the data, the C_2H UV absorption cross section was assigned a one order-of-magnitude uncertainty in this analysis.

Reviews of the H_2 Lyman and Werner band systems are provided by Fabian and Lewis.[122] They compare the oscillator strengths computed by Allison and Dalgarno,[121] which are applied in the present study, with various experimental measurements. The agreement for the Lyman band is shown to be excellent, while that for the Werner band is slightly worse. Based on these comparisons, the oscillator strength uncertainties for the Lyman and Werner bands are assigned as ±10% and ±20%, respectively.

2. *Atomic Photoionization for Ablation Products*

The contribution of atomic photoionization emission and absorption from atomic carbon and hydrogen is relatively small, the primary contribution being the VUV absorption from atomic carbon above 12 eV. A review of theoretical atomic carbon photoionization cross sections was made by Escalante.[127] As a result of this study and the experimental measurements of Marrone,[106] an uncertainty of ±20% was assigned to the atomic carbon and hydrogen photoionization cross sections in this work.

D. Uncertainty in C_2, C_3, and CN Heats of Formation

According to Gurvich et al.,[128] the heat of formation for four of the present ablation products have uncertainties greater than 1%. A discussion of the uncertainties for C_3 is also presented by Jones et al.[129] The uncertainties listed by Gurvich et al. are listed in Table 6 and are applied in the present work. These uncertainties were found to have a negligible impact on the radiative and convective heating for the 15 km/s case. Therefore, they will not be considered further in the present analysis. Note that this is not consistent with the results of Moss and Simmonds[30] for Jupiter entry, where they showed a roughly 10% influence of these properties. However, the larger uncertainties at the time and the larger ablation rates present for their case were responsible for the large influence observed.

E. Uncertainties Due to Ionization Potential Lowering

1. *Strong Dependence of Partition Functions on Excited Electronic States*

As discussed by Capitelli et al.[130] and Coufal et al.,[131] above a temperature of roughly 10,000 K the electronic partition functions of atoms become very sensitive to the treatment of highly excited states. This issue may potentially influence the flowfield predictions through its influence on the enthalpy. The enthalpy is related to the total partition functions of atomic species as follows:

$$\frac{H(T)-H(0)}{RT} = T\frac{\partial Q_{total}}{\partial T} = \frac{hc}{k}\frac{\sum_{i=1}^{N} E_i g_i exp\left(-\frac{hc}{kT}E_i\right)}{\sum_{i=1}^{N} g_i exp\left(-\frac{hc}{kT}E_i\right)} + \frac{5}{2} \tag{4}$$

This equation shows the dependence of the enthalpy on the summation over the electronic levels from the ground state ($i = 1$) to some upper level cutoff ($i = N$). For atomic nitrogen, Table 7 presents the 35 electronic levels applied in HARA, which will be used in the following discussion. The value of N chosen by various researchers has differed significantly. For example, Gurvich et al.[128] includes just the first 3 levels of Table 7 while Gordon and Mcbride[132] include all the levels with E_i values below $E_I - kT$, which for atomic nitrogen may be written as $14.54 - 8.618 \times 10^5$ T (eV), where T is in K. A comparison between these two approaches and that which includes all the levels listed in Table 7 is made in Figs. 34 and 35 for the specific heat and enthalpy, respectively. It is seen in Fig. 34 that the three approaches diverge for temperatures above 11,000 K, with the "All Levels" result being 40% greater than the Gurvich result at 15,000 K. The enthalpy differences between the three approaches in Fig. 35 are smaller than for the specific heat, and they become noticeable above 12,000 K.

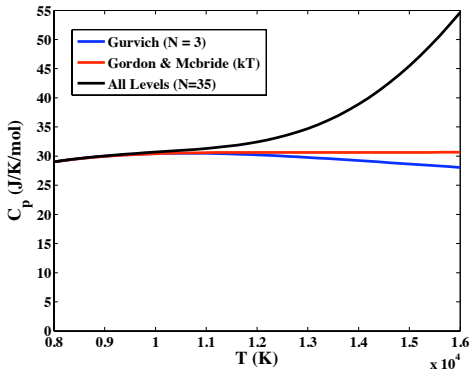

Figure 34: Comparison of various methods of computing the specific heat of atomic nitrogen.

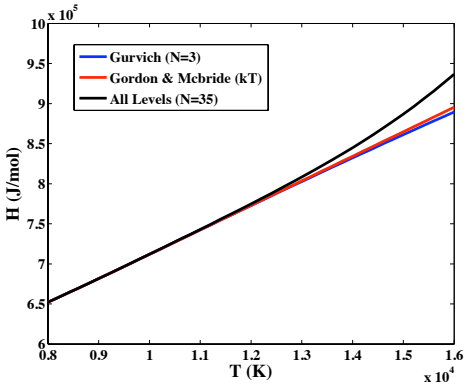

Figure 35: Comparison of various methods of computing the enthalpy of atomic nitrogen.

For the present Mars-return flight cases, the differences shown here in the specific heat and enthalpy due to the levels treated in the partition function were found to have a negligible influence on the flowfield and radiative flux. This phenomenon will therefore not be considered further in this work. However, the lowering of the ionization potential will be shown to have other influences in the following discussions.

2. *Lowering of the Ionization Potential*

As discussed by Pomerantz,[134] as the ionization and pressure of a gas increases, the ionization potential of atoms in the gas is reduced. Several models for predicting the magnitude of this reduction are presented by Nelson[135] and compared for shock layers relevant to Jupiter entry. The approach that resulted in the largest ionization potential reduction, referred to as the Unsöld approximation, may be written as

$$\Delta E_I = 3e^2(4\pi N_e/3)^{1/3} = 6.964 \times 10^{-7} N_e^{1/3} \tag{5}$$

where ΔE_I is in eV, N_e is the electron number density in particles/cm^3, and e is the electron charge. This equation indicates that at a number density of $1{\times}10^{17}$ particles/cm^3 (which is equal to the peak value for the Mars-return case), ΔE_I is equal to 0.32 eV.

The main consequence of ΔE_I is its influence on the Saha equation, which is a governing equation for computing the chemical equilibrium composition. The Saha equation is written as

$$\frac{N_+ N_e}{N_a} = 2\frac{Q_+}{Q_a}\left(\frac{2\pi m k T_e}{h^2}\right)^{3/2} exp\left(-\frac{E_I - \Delta E_I}{kT_e}\right) \tag{6}$$

As ΔE_I increase, this equation shows that the level of ionization will increase. When computing the state of the gas behind a shock, this tends to decrease the equilibrium temperature and therefore the radiation.

Analyses of radiating flowfields present in the aerothermodynamics literature do not typically account for the lowering of the ionization potential, with only a few exceptions.[135,136] To illustrate the approximate influence of ionization potential lowering on a high-speed Earth entry shock layer, the equilibrium conditions behind a normal shock moving at range of velocities and a density of $3{\times}10^{-4}$ kg/m^3 are considered. The percent difference in the post-shock temperature and electron number density due to ionization potential lowering are shown in Fig. 36. The differences in both of these quantities are seen to be less than 2% for the range of velocities. The percent difference in the radiative flux, assuming a 15-cm constant property layer at the post shock conditions, are also shown in the figure. A roughly 15% decrease in the radiative flux is seen to result from ionization potential lowering. This illustrates the significant sensitivity of the radiative flux to the temperature, and consequently to the ionization potential. For the actual shock-layer cases presented later, the influence of ionization potential lowering will be less than the 15% shown here because of the influence of radiative cooling, which tends to increase the shock-layer temperature as the radiation decreases.

Table 7: Electronic energy level data for atomic nitrogen defined by Johnston.[133]

Level i	E_i (eV)	g_i
1	0	4
2	2.383962	10
3	3.575602	6
4	10.332297	12
5	10.686543	6
6	10.927030	12
7	11.602633	2
8	11.758386	20
9	11.841712	12
10	11.995575	4
11	12.005823	10
12	12.124904	6
13	12.356713	10
14	12.856402	12
15	12.918660	6
16	12.972258	6
17	12.983572	28
18	12.999857	14
19	12.999348	12
20	13.019245	20
21	13.034976	10
22	13.201564	2
23	13.244404	20
24	13.268039	12
25	13.294202	10
26	13.321559	4
27	13.342560	6
28	13.676543	90
29	13.697743	126
30	13.960947	450
31	14.170345	648
32	14.270642	822
33	14.335606	1152
34	14.380238	1458
35	14.412100	1800

3. *Photoionization Edge Shift*

The photoionization edge shift refers to the change in the spectral position of the photoionization edge resulting from each electronic energy level.[137] Considering the hydrogenic photoionization model in a vacuum, the location of these edges are computed as $E_I - E_i$. However, as discussed in the previous subsection, at the pressures and temperatures of present interest the ionization potential, E_I, is reduced by some non-negligible value. This change in E_I from its value in a vacuum causes a shift in the photoionization edges.

The merging of atomic lines near the photoionization edges also contributes to the apparent photoionization edge shift.[138] If it is assumed that all atomic lines are treated in detail, then this influence should not be considered. This is believed to be the case for the HARA code, where atomic lines from both NIST[139] and the Opacity Project[85] are considered and detailed Stark broadening values are applied.[46]

The HARA code does not apply the hydrogenic model directly. Instead it applies detailed photoionization cross sections taken from the TOPbase project.[61] These cross-section were computed assuming a vacuum and therefore should also be corrected for the edge shift.

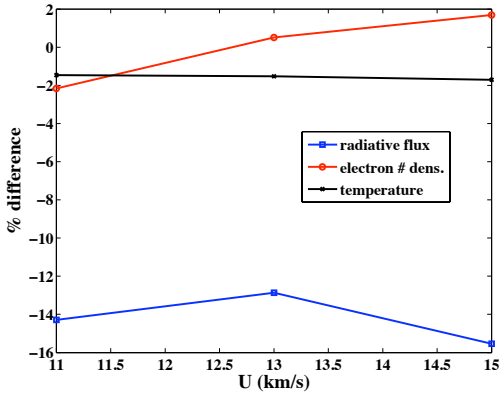

Figure 36: Influence of ionization potential lowering on equilibrium shock properties.

VIII. Parametric Uncertainty Results for a Range of Cases

The results of the parametric uncertainty analysis discussed in the previous section are presented in Table 8 for the stagnation point radiative heating of the 5 m radius case over a range of velocities. The individual components from the various radiative mechanisms are listed along with the total parametric uncertainty, which is the sum of the individual components. The positive uncertainty is listed without parenthesis, while the negative uncertainty is listed within parenthesis. The rows in this table each refer to a specific group of the uncertainty parameters: "Air: Molec. Bands" and "AP: Molec. Bands" refer to the uncertainty resulting from Air and Ablation Product (AP) molecular band oscillator strength uncertainties; "Air: Atomic Lines: $f_{i,j}$" from all air atomic line oscillator strength uncertainties; "Atomic Lines: $\Delta\lambda_{S,0}$" from all air atomic line Stark broadening width uncertainties; "Air: Atomic Photoionization" and "AP: Atomic Photoionization" from all air and ablation product atomic photoionization cross section uncertainties; "Air: Opacity Project Lines" from all Opacity Project line uncertainties; "Air: Neg. Ion Photodetach." from all negative ion photodetachment cross section uncertainties. In addition to these uncertainties, the influence of including ionization potential lowering and photoionization edge shift, which are not included in the baseline model, are listed in the "Ion. Potential Lowering" and "Photo. Edge Shift" rows. These two rows represent simply the impact of adding these phenomena to the prediction (note that the "Ion. Potential Lowering" result represents the only flowfield parametric uncertainty treated in this study). Similarly, the Opacity Project exclusive lines (meaning the lines that are included in the Opacity Project but not by NIST) are not included in the baseline radiation model. The "Air: Opacity Project Lines" row therefore represents the total contribution from these lines (it is always a positive contribution).

Table 8 shows that at 15 km/s the parametric uncertainty for the stagnation-point radiative heating is +47.3% and -28.3%. The dominant uncertainty contributors at this velocity are a product of the atomic lines and ablation product molecular bands. At lower velocities, the ablation product molecular bands are seen to contribute less to the uncertainty. It is interesting to note that the positive uncertainty increases with velocity, while the negative uncertainty decreases. This is mainly a result of the ablation product molecular band systems (AP: Molec. Bands), whose positive uncertainty contribution increases significantly with velocity, but whose negative contribution only slightly varies.

Table 8: Summary of parametric uncertainty contributors for the 5 m radius case at the stagnation point. Values not in parenthesis are the + component while those in parenthesis are the − component. All values are percent.

Parameter Group	11 km/s	12 km/s	13 km/s	14 km/s	15 km/s
Air: Molec. Bands	0.64(0.58)	0.11(0.11)	0.04(0.04)	0.01(0.01)	0.01(0.01)
Air: Atomic Lines: $f_{i,j}$	7.53(8.02)	7.21(7.88)	7.24(7.90)	6.91(7.43)	6.64(7.04)
Air: Atomic Lines: $\Delta\lambda_{S,0}$	7.17(8.31)	6.23(7.48)	5.97(7.25)	5.62(6.57)	5.26(5.90)
Air: Atomic Photoionization	3.88(3.99)	3.79(3.88)	3.76(3.78)	3.83(3.83)	3.89(3.88)
Air: Opacity Project Lines	9.73(0.00)	10.3(0.00)	10.6(0.00)	10.1(0.00)	9.70(0.00)
Air: Neg. Ion Photodetach.	4.48(4.48)	2.97(2.97)	2.02(2.02)	1.58(1.58)	1.26(1.26)
AP: Molec. Bands	2.86(6.02)	8.02(7.04)	10.0(7.72)	12.8(7.94)	15.1(7.20)
AP: Atomic Photoionization	0.40(0.37)	0.40(0.37)	0.38(0.35)	0.27(0.23)	0.16(0.13)
Ion. Potential Lowering	0.00(5.10)	0.00(4.45)	0.00(3.31)	0.00(3.18)	0.00(2.92)
Photo. Edge Shift	4.44(0.00)	4.79(0.00)	4.96(0.00)	5.14(0.00)	5.30(0.00)
Total	41.1(36.8)	43.8(34.2)	45.0(32.4)	46.2(30.8)	47.3(28.3)

The top individual uncertainty contributors for the 15 km/s case are listed in Table 9. The band systems for the C_3 and C_2H molecules are seen to contribute the top 2 uncertainties. These band systems

are strong absorbers, meaning that the positive uncertainty is a result of decreasing the band oscillator strengths (representing the lower uncertainty bounds). In addition to the molecular band oscillator strength uncertainties, Table 9 shows the negative ion photodetachment uncertainty from atomic nitrogen (σ^- (N^-)), the atomic nitrogen photoionization cross sections (σ_{bf} (N, level 30)) from a specified electron state (defined in Table 7), and the atomic line oscillator strength (f_{ij} (N)) and Stark broadening ($\Delta\lambda_{S,0}$ (N)) uncertainties from strong lines defined in Table 3. Note that all the individual lines in a single multiplet are combined in these results. It is seen that while the various molecular bands present in Table 9 combine to provide nearly the total molecular band uncertainty value in Table 8, the atomic line contributions in Table 9 combine to only a small fraction of the total values. This indicates that the many weak uncertainty contributions from the 430 lines for nitrogen and 293 lines for oxygen all contribute to the total atomic line uncertainty.

Table 9: Top uncertainty contributions from individual parameters for the 15 km/s case.

Rank	Parameter	Uncertainty (±%)	$\pm q_{rad}$ (%)
1	C_3 Swings	$O(1)$ mag.	9.60 (3.41)
2	C_2H UV	$O(1)$ mag.	2.39 (2.05)
3	σ^- (N^-)	100	1.26 (1.26)
4	C_2 Swan	50	0.89 (0.63)
5	f_{ij} (N) – 919.8 nm	50	0.49 (0.53)
6	CN Red	30	0.49 (0.46)
7	$\Delta\lambda_{S,0}$ (N) – 1052.6 nm	75	0.27 (0.66)
8	C_3 UV	$O(1)$ mag.	0.87 (0.02)
9	σ_{bf} (N, level 30)	20	0.44 (0.44)
10	$\Delta\lambda_{S,0}$ (N) – 1011.7 nm	50	0.39 (0.45)
11	f_{ij} (N) – 1070 nm	75	0.37 (0.45)
12	CO 4+	40	0.48 (0.31)
13	f_{ij} (N) – 999.1 nm	75	0.34 (0.37)
14	σ_{bf} (N, level 17)	20	0.32 (0.32)
15	H_2 Lyman	10	0.33 (0.21)

Similarly to Table 9, Tables 10 and 11 present the individual uncertainty contributors for the 13 and 11 km/s cases, respectively. By comparing these 3 tables, it is seen that as the velocity is decreased the uncertainties from ablation products become smaller. This behavior is expected from the reduced ablation rates presented in Section IV. As shown in Table 8, the increase in the negative ion photodetachment (σ^- (N^-)) and atomic line uncertainties as the velocity decreases compensate partially for the decrease in ablation product uncertainties. The N_2 Birge-Hopfield (N_2 BH1) band oscillator strength is present in Tables 10 and 11, which indicates the more N_2 is present in boundary layer because of the lower ablation rates.

Table 10: Top uncertainty contributions from individual parameters for the 13 km/s case.

Rank	Parameter	Uncertainty (±%)	$\pm q_{rad}$ (%)
1	C_3 Swings	$O(1)$ mag.	5.83 (4.95)
2	C_3 UV	$O(1)$ mag.	2.05 (2.30)
3	σ^- (N^-)	100	2.02 (2.02)
4	C_2H UV	$O(1)$ mag.	1.24 (1.76)
5	f_{ij} (N) – 919.8 nm	50	0.50 (0.55)
6	$\Delta\lambda_{S,0}$ (N) – 124.3 nm	100	0.49 (0.61)
7	$\Delta\lambda_{S,0}$ (N) – 1052.6 nm	75	0.35 (0.81)
8	$\Delta\lambda_{S,0}$ (N) – 1011.7 nm	50	0.36 (0.51)
9	f_{ij} (N) – 1070 nm	75	0.38 (0.46)
10	$\Delta\lambda_{S,0}$ (N) – 821.4 nm	30	0.34 (0.43)
11	σ_{bf} (N, level 30)	20	0.39 (0.39)
12	CO 4+	40	0.40 (0.30))
13	f_{ij} (N) – 999.1 nm	75	0.33 (0.38)
14	N_2 BH1	50	0.48 (0.31)
15	H_2 Lyman	10	0.36 (0.26)

Table 11: Top uncertainty contributions from individual parameters for the 11 km/s case.

Rank	Parameter	Uncertainty (±%)	$\pm q_{rad}$ (%)
1	σ^- (N^-)	100	4.48 (4.49)
2	C_3 UV	$O(1)$ mag.	1.12 (4.03)
3	CO 4+	40	0.80 (0.61))
4	$\Delta\lambda_{S,0}$ (N) – 174.3 nm	50	0.62 (0.69)
5	σ_{bf} (N, level 3)	20	0.46 (0.59)
6	$\Delta\lambda_{S,0}$ (N) – 1052.6 nm	75	0.35 (0.73)
7	f_{ij} (N) – 919.8 nm	50	0.42 (0.46)
8	$\Delta\lambda_{S,0}$ (N) – 124.3 nm	100	0.39 (0.48)
9	$\Delta\lambda_{S,0}$ (N) – 1011.7 nm	50	0.33 (0.50)
10	$\Delta\lambda_{S,0}$ (N) – 821.4 nm	30	0.36 (0.42)
11	f_{ij} (N) – 1070 nm	75	0.33 (0.39)
12	$\Delta\lambda_{S,0}$ (N) – 869.4 nm	30	0.36 (0.45)
13	N_2 BH1	50	0.37 (0.31)
14	CN Red	30	0.30 (0.30)
15	f_{ij} (N) – 999.1 nm	75	0.27 (0.31)

IX. Final Uncertainty Determination

The structural uncertainty for the 15 km/s, 5 m flight case was determined to be +34%, −24% in Section VI, while the parametric uncertainty was determined to be +47.3% and −28.3% in Section VIII. Combining these components results in a total radiative heating uncertainty of +81.3% and −52.3%. These uncertainty values are only appropriate for the baseline flowfield and radiation models presented in this work. However, sufficient details regarding the composition of these uncertainty values have been provided so that appropriate adjustments may be made for other flowfield and radiation models.

The approach used to determine the +81.3% and −52.3% flight case uncertainty values has been purely computational. This has been required because no laboratory or flight data exists at conditions that replicate a Mars-return condition. However, there have been laboratory shock tube measurements in the 1960s over small models (with radii on the order of an inch) that include temperatures comparable with the Mars-return flight case. Therefore, to include a level of validation to the present uncertainty analysis, the same baseline flowfield and radiation models developed in this work were applied to these shock tube cases, along with the present parametric uncertainty analysis. If the baseline predictions, combined with the computed parametric and structural uncertainty, compare favorably with the experimental measurements, then the present uncertainty analysis may be considered adequate. This analysis is discussed in detail in Parts II and III of this work. It may be noted that favorable comparisons between predictions and experiments are observed in Parts II and III. Therefore, it may be concluded that, to the best of our knowledge, the present uncertainty approach is adequate.

X. Summary of Part I

The radiative heating uncertainty for a Mars-return to Earth was studied. A baseline simulation approach that includes coupled ablation and radiation in the LAURA flowfield code was discussed. Radiation coupling was included using the HARA radiation code, which includes a smeared rotational band (SRB) treatment of molecular band systems and tangent slab radiation transport. The SRB model was shown to result in only a ±2% uncertainty, although it required orders-of-magnitude less computational time than the rigorous line-by-line approach. Coupled ablation and radiation were shown to both reduce the radiative heating by nearly 50% at 15 km/s. A structural uncertainty of +34%, -24% is determined for the radiative heating. This structural uncertainty contains a +20% contribution from precursor heating, a -10% contribution from radiation transport, and a ±10% contribution from turbulence modeling. A detailed discussion is provided for each of these uncertainty components. A epistemic parametric uncertainty analysis, using interval uncertainties, is presented. This analysis accounts for uncertainties in the radiation model as well as heat of formation uncertainties in the flowfield model. Discussions and references are provided to support the uncertainty range chosen for each parameter. Parametric uncertainties of around 50% are predicted from this analysis. The largest uncertainty contributors are the C_3 swings cross-section, photoionization edge shift, and Opacity Project atomic lines. Combining the parametric and structural uncertainties results in an uncertainty of +81.3% and −52.3% for the 15 km/s case. This is the recommended uncertainty for the radiative heating resulting from this work. Parts II and III of this work compare this uncertainty approach to experimental measurements, with favorable results.

Part II
Comparison with 1960s Era Shock Tube Measurements

XI. Introduction to Part II

Part II takes the simulation and uncertainty approaches presented in Part I of this study and applies them to experimental constricted-arc and 1960s era shock tube cases. These experiments measured the spectrally-integrated intensity at high temperatures (T >11,000 K) through a small column of gas (for the constricted-arc cases) or to the stagnation point of a small body (for the shock tube cases). The purpose of this work is to show that the uncertainty limits computed for the radiative intensity overlap the measurement error bars. This measure of agreement quality is based on the fact that the parametric uncertainty is computed using an interval analysis (as discussed in Part I). Satisfaction of this criteria will support the legitimacy of the uncertainty analysis applied in Part I to determine the flight case uncertainty.

The present work considers the shock-tube and constricted-arc experiments studied by Sutton,[140] which served as a guide for much of the present work. The shock tube experiments considered are by Hoshizaki,[141] Thomas and Menard,[142] Nerem,[143] and Gruszynski and Warren.[144] These experiments all measured the spectrally-integrated radiative intensity between 0 and 6 eV at the stagnation point of a small model placed in the shock tube. With free-stream shock tube velocities and pressures up to 1.0 Torr and 10 km/s, temperatures up to 16,000 K were obtained within the shock layer of the model. Because of the relevance of these high temperatures to a Mars return shock layer, these experimental studies were chosen as the best candidate for validating the simulation methodology and uncertainty analysis presented in Part I.

Other shock-tube radiation experiments are not considered in Part II for various reasons. Recent experiments[145,146] in the EAST shock tube are considered Part III of this work. These experiments contain spectrally-resolved intensity measurements behind a moving shock. Similar spectraly-resolved shock tube measurements [147–150] were not considered in this study because of their relatively low temperatures and limited spectral range. Reflected-shock measurements,[151,152] which were studied by Sutton,[140] are not considered here because of the uncertainty in the thermodynamic conditions of the measurements.

As stated previously, the purpose of Part II is to apply the simulation and uncertainty approaches presented in Part I to experimental shock tube and constricted-arc and cases, which will allow the legitimacy of the uncertainty analysis to be assessed. The relevance of the considered experiments to the actual Mars-return flight cases is discussed in Section XII. A brief review of the uncertainty analysis and a discussion of important parameters for experimental data comparisons are presented in Section XIII. Sections XIV and XV compare shock tube and constricted arc measurements, respectively, with simulations. Uncertainty analyses are presented for many of the simulations to provide error bars for the comparisons with measurements.

XII. Relevance of Experimental Cases to Flight

A range of simplified flight conditions for Mars-return were identified in Part I. These consisted of 1 and 5 m radius spheres at a free-stream density of 3×10^{-4} kg/m^3 and velocities ranging from 10 to 15 km/s. Uncertainty analyses were performed using the outlined approach, which resulted in a radiative heating uncertainty value for each case. As mentioned previously, the purpose of Part II is to apply this uncertainty approach to experimental cases and show that the computed uncertainty is large enough to capture the differences between measurements and predictions. The purpose of this section is to show that the experimental cases considered are relevant to the flight cases.

The experimental cases considered in this study measure the radiative intensity between 0 and 6 eV, which ignores the important vacuum ultraviolet (VUV) region of the spectrum (6 – 14 eV). The drawback of not obtaining experimental values for the VUV region is lessened by the fact that this region is predicted to contribute little to the wall radiative flux for a flight case, as a result of ablation product absorption. Although this absorbed radiation influences the flowfield through radiation coupling, it is a second order effect and does not result in a proportional increase in convective heating. Furthermore, since the experimental cases considered here do not contain ablation, VUV measurements would be of minimal value for representing the flight environment. Note that as shown in Fig. 11, ablation products also have an influence in the 0 – 6 eV range, although it is much less than in the VUV.

To show the similarity between the experimental and flight radiative heating environments, Fig. 37

compares the wall radiative flux between 0 and 6 eV predicted for the experimental and flight cases. The horizontal axis in this figure is the post-shock temperature. This temperature decreases from the shock to the body because of the radiative cooling. As will be shown, the radiative cooling effect is larger for the flight cases. For a given post shock temperature, an agreement in q_r^- values indicates similar radiative flux environments. This agreement is seen for many cases in the figure, which confirms the relevance of the experimental cases to the flight cases.

The ability of small shock tube models to produce radiative heating environments similar to large flight vehicles is apparent from studying the radiative flux equation for a constant property layer:

$$q^-_{r,h\nu} = \pi B_{h\nu} \left[1 - exp(-\kappa_{h\nu}\Delta z)\right] \tag{7}$$

The parameter $B_{h\nu}$ is the Planck function, which is a function of temperature only. The absorption coefficient $\kappa_{h\nu}$ may be roughly approximated assuming chemical equilibirum as follows

$$\kappa_{h\nu} \ = \psi(T)p \tag{8}$$

where is ψ is a like a cross-section and contains the complex spectral information. For a given temperature, both $B_{h\nu}$ and ψ remain constant, so that the only difference in Eq. (7) is the product $p\Delta z$. For the flight cases, p ranges from 0.3 to 0.6 atm while Δz, which may be considered the shock-standoff, is around 20 cm. This results in a $p\Delta z$ ranging from 6 to 12 atm-cm for the flight cases. For the experimental cases, the post shock pressure (for the bow shock of the model) and shock standoff are reported in Section XIV for each case. These pressures range from 2 to 15 atm and the shock standoff distances range from 0.15 to 0.80 cm, resulting in $p\Delta z$ ranging from about 1 to 10 atm-cm. This shows that the larger post shock pressures for the experimental cases compensate for the small shock standoff distances, which results in $p\Delta z$ that are the same order-of-magnitude as the flight cases.

To confirm further the relevance of the presently considered experiments with the flight cases, Fig. 38 compares the radiative flux spectrum at the stagnation point for the 15 km/s, 5 m flight case (without ablation) and the Thomas and Menard experiment at 9 km/s (which has a post-shock temperature of 14,080 K in Fig. 37). The cumulative flux below 6 eV is nearly identical for both cases, while the flux above 6 eV (VUV) is significantly larger for the laboratory case. This difference in the VUV is a result of the temperature decrease (moving from the shock to the wall) for the flight case (caused by radiative cooling), which increases absorption. Figure 39 illustrates this point by comparing the wall directed radiative flux profiles along the stagnation line. Minimal absorption is seen for the 0 – 6 eV profiles, while the 6 – 14 eV profiles show significant absorption. Note that absorption is indicated by a non-linear increase in the radiative flux as the wall is approached.

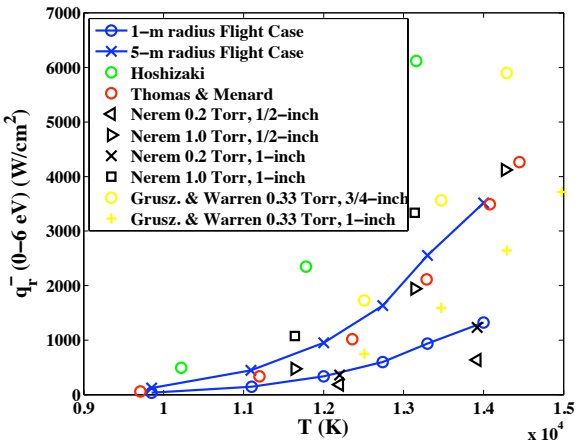

Figure 37: Comparison of experimental and flight radiative flux values as a function of post-shock temperature.

As mentioned in the previous paragraphs, the influence of radiative cooling is larger for the flight cases than the shock tube cases. The reason for this is that, for the shock tube cases, the radiative flux emitted from the shock layer is a smaller percentage of the total energy flux into the shock layer. For the shock tube cases, the total enthalpy flux into the shock layer is computed as $E = (0.5U_1^2)(\rho_2 U_2)$, where the first term in parenthesis is the free-stream total enthalpy and the second term is the mass flux across the bow shock (subscripts 1 and 2 indicate values before and after the moving shock). For the flight case this is simply $E = 0.5\rho U^3$, where ρ and U are the free-stream values. As an example, consider the Thomas and Menard experiment at 9 km/s (discussed previously), which is shown in Fig. 37 to produce nearly identical post shock temperature and radiative flux (below 6 eV) values as the 15 km/s, 5 m radius flight case. For the Thomas and Menard case E is equal to 4.65×10^9 W/m^2, while for the flight case it is equal to 5.06×10^8 W/m^2. The uncoupled radiative flux ($q_{r,0}$) for the Thomas and Menard case is 4.12×10^7 W/m^2, while for the flight case it is 1.55×10^8 W/m^2. It is clear from these values that the ratio $q_{r,0}/E$ is

much larger for the flight case than the experimental case, which indicates that radiative cooling will be more significant.

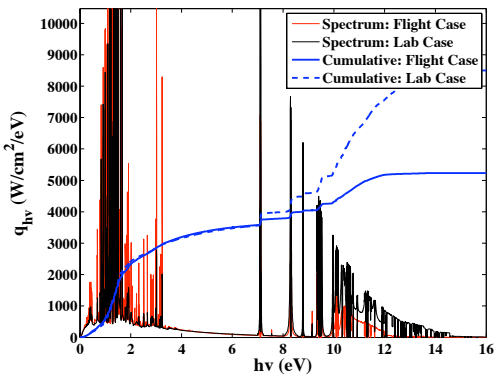

Figure 38: Comparison of an experimental and flight radiative flux spectrum.

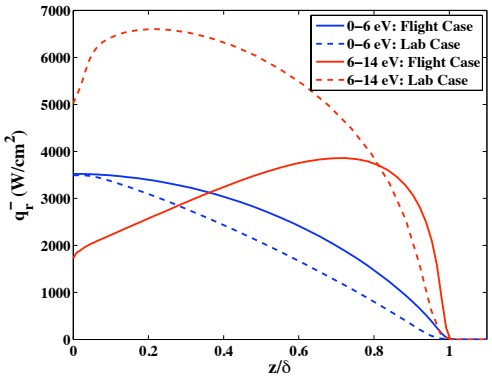

Figure 39: Comparison of wall-directed radiative flux along the stagnation line for an experimental and flight case.

XIII. Overview of Comparisons between Experiments and Predictions

The purpose of the present comparisons between predictions and experiments is to show that the predicted uncertainty bands for radiative intensity are sufficient to overlap measured radiative intensity values. This agreement would provide evidence that the uncertainty analysis and computational techniques discussed in Part I are valid and sufficient. The following subsections discuss the predicted uncertainty bars, the curve fitting of the data to aid in assessing the overlap with predictions, and a quantitative measure of comparison quality based on this overlap.

A. Uncertainty Analysis Review

The uncertainty analysis presented in Part I of this work identified all potentially significant structural and parametric uncertainties. The structural uncertainty value was determined to be +34% and -24% for the radiative flux to an ablating, turbulent vehicle. Because the present comparisons with measurements will consider the radiative intensity, instead of the radiative flux, to non-ablating laminar models, the ±10% uncertainty for turbulence modeling and the +10% uncertainty from transport modeling of the radiative flux are no longer issues. Furthermore, the small model size will minimize the precursor influence significantly, and therefore the +20% uncertainty to account for the precursor influence is unnecessary. Consequently, only the ±2% uncertainty to account for grid convergence and ±2% uncertainty to account for smeared rotational band modeling in the HARA radiation code are appropriate. The parametric uncertainty will be computed for each case and combined with the ±4% structural uncertainty to obtain the uncertainty for each prediction. Note that an interval uncertainty analysis is applied to obtain the parametric uncertainty. This means that the uncertainty bars placed on each prediction represent a range of possible prediction values, and that the baseline value is no more significant than the far ends of the uncertainty bars.

The parametric uncertainty analysis presented in Part I is applied to the present cases. Only uncertainties from air species are required for these cases because no ablation products are present. Furthermore, because the intensity measurements cover only the 0 – 6 eV spectral range, the uncertainties presented are for this spectral range only.

B. Computing "Data Fit Limits"

Deciding whether the predicted uncertainty bars overlap the measured data is complicated by the significant scatter in the presently considered data. To simplify the comparisons, the measured data are least-squares fit to a polynomial for each case. This polynomial is written here as

$$DataFit = a_1 x^2 + a_2 x + a_3 \tag{9}$$

where x is either the velocity in km/s (for the shock-tube cases) or temperature in K (for constricted arc cases) and the coefficients a_i are listed during the discussion of each case. It will be shown that the data

scatter is nearly completely bounded by ±35% limits on the curve fits for both the shock tube cases and constricted-arc cases. These limits, referred to here as "Data Fit Limit", will be plotted for each case and used in the following discussion of comparison quality.

C. Merit of Comparison Between Measurements and Predictions

For each comparison between experiment and prediction, the chosen measure of quality is the percent overlap of the predicted uncertainty bars with the Data Fit Limits defined in the previous paragraph. This overlap is illustrated in Fig. 40, which shows a 76% overlap between the HARA-LAURA uncertainty bar and the band created by the Data Fit Limits. The choice of this overlap as the measure of prediction quality is based on the fact that the prediction uncertainty bars are obtained from an interval analysis. This means that there is no probability distribution associated with the uncertainty bars, and hence the baseline value is no more probable (based on this analysis) than the ends of the uncertainty bars. Furthermore, it will be shown in the following Sections that the scatter of experimental data within the Data Fit Limits suggests that the band created by these limits also be treated as an interval. As a result of these two statements, the best comparison possible consists of the experiment and prediction intervals completely overlapping. Assuming that the prediction interval is smaller than the experimental interval, which it is for most shock-tube cases, then a 100% overlap of the prediction interval with the experimental interval represents the best possible agreement. However, note that even 100% overlap only guarantees that all possible predictions (according to the uncertainty analysis) overlap plausible experimental values, not that they necessarily agree. Nevertheless, this is the best possible agreement because it minimizes the maximum possible deviation between experiment and predictions.

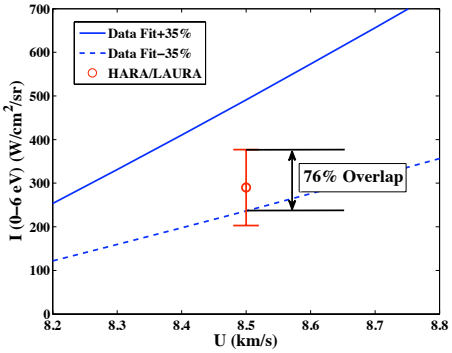

Figure 40: Example of percent overlap.

XIV. Comparison with Shock-Tube Radiative Intensity Measurements

This section compares the coupled HARA/LAURA predictions, along with their computed uncertainty, with the shock tube measurements of stagnation point radiative intensity. In addition to the HARA/LAURA predictions, results from the DPLR flowfield and NEQAIR radiation codes and the results of Sutton[140] are compared. For each experiment, the computed free-stream conditions are presented along with the resulting baseline radiative intensity between 0 and 6 eV. The parametric uncertainty is computed for the highest velocity condition for each experiment. These values, which represent the percent uncertainty for the spectrally-integrated intensity between 0 – 6 eV, are listed in Table 12. In this table, the values out of parenthesis represent the positive (+) uncertainty component, while the values in parenthesis represent the negative (−) component. The rows in this table each refer to a specific group of uncertainty parameters: "Air: Molec. Bands" refers to the uncertainty resulting from molecular band oscillator strength uncertainties; "Air: Atomic Lines: $f_{i,j}$" from all atomic line oscillator strength uncertainties; "Air: Atomic Lines: $\Delta\lambda_{S,0}$" from all atomic line Stark broadening width uncertainties; "Air: Atomic Photoionization" from all photoionization cross section uncertainties; "Air: Opacity Project Lines" from all Opacity Project line uncertainties; "Air: Neg. Ion Photodetach." from all negative ion photodetachment cross section uncertainties. In addition to these uncertainties, the influence of including ionization potential lowering and photoionization edge shift, which are not included in the baseline model, are listed in the "Ion. Potential Lower-

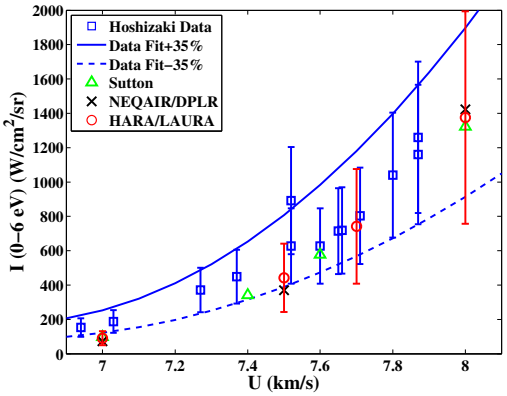

Figure 41: Comparison between intensity measurements and predictions for the Hoshizaki cases.

ing" and "Photo. Edge Shift" rows. These two rows represent simply the impact of adding these phenomena to the prediction (note that the "Ion. Potential Lowering" result represents the only flowfield parametric uncertainty treated in this study). Similarly, the Opacity Project exclusive lines (meaning the lines that are included in the Opacity Project but not by NIST) are not included in the baseline radiation model. The "Air: Opacity Project Lines" row therefore represents the total contribution from these lines (it is always a positive contribution).

The parametric uncertainties listed in Table 12 show that total parametric uncertainties for the various cases range between 24 – 41%. The Opacity Project lines and negative ion photodetachment cross sections provide the largest uncertainty variation between the various cases, with the former increasing with velocity and the latter decreasing. The Nerem 0.2 Torr case at 11 km/s represents the highest velocity case considered. It is seen that this case contains the largest Opacity Project line contribution and smallest negative ion contribution. The Stark broadening contribution to the uncertainty is seen to be relatively small, with the negative uncertainty significantly larger than the positive value.

Note that these computed parametric uncertainties are combined with the ±4% uncertainty discussed in Section XIII-A to obtain the total prediction uncertainty. The total prediction uncertainty is compared with the Data Fit Limits discussed in Section XIII-B to obtain the percent overlap defined in Section XIII-C. The curve-fit coefficients for the Data Fit curves are listed in Table 13 for each experimental case. The temperature limits for each curve fit are also listed in this table.

Table 12: Summary of Parametric Uncertainty Contributors for Shock Tube Cases.

Parameter Group	Hoshizaki 8 km/s, 1.16 Torr	Thomas and Menard 9.3 km/s, 1.25 Torr	Nerem 2.54 cm 9.0 km/s, 1.0 Torr	Nerem 2.54 cm 11 km/s, 0.2 Torr	Grusz. and War. 3.81 cm 10 km/s, 0.33 Torr
Air: Molec. Bands	0.13 (0.13)	0.06 (0.06)	0.04 (0.04)	0.02 (0.02)	0.02 (0.02)
Air: Atomic Lines: $f_{i,j}$	6.58 (6.63)	7.50 (7.68)	5.60 (5.58)	6.96 (6.95)	5.92 (5.94)
Air: Atomic Lines: $\Delta\lambda_{S,0}$	3.78 (5.16)	2.95 (4.53)	3.52 (4.98)	2.35 (4.06)	3.68 (5.62)
Air: Atomic Photoionization	4.26 (4.26)	4.83 (4.81)	5.48 (5.46)	5.58 (5.57)	5.83 (5.81)
Air: Opacity Project Lines	6.83 (0.00)	8.10 (0.00)	7.90 (0.00)	11.5 (0.00)	5.91 (0.00)
Air: Neg. Ion Photodetach.	13.0 (13.0)	4.40 (4.40)	7.80 (7.80)	2.18 (2.18)	4.20 (4.20)
Ion. Potential Lowering	0.00 (8.81)	0.00 (9.5)	0.00 (8.11)	0.00 (5.8)	0.00 (9.3)
Photo. Edge Shift	7.14 (0.00)	6.50 (0.00)	8.10 (0.00)	8.30 (0.00)	8.11 (0.00)
Total	41.7 (38.0)	34.4 (31.0)	38.4 (32.0)	34.6 (24.6)	33.7 (30.9)

Table 13: Curve-fit coefficients and temperature limits for the experimental Data Fit curves defined by Eq. (10).

Case	a_1	a_2	a_3	T_{lower} (K)	T_{upper} (K)
Hoshizaki	7.9271e+02	-1.0672e+04	3.6050e+04	6900	8100
Thomas and Menard	2.3286e+02	-3.1953e+03	1.1006e+04	6900	9500
Nerem 1.27 cm, 0.2 Torr	-2.4500e+01	6.2157e+02	-3.3763e+03	8000	11500
Nerem 1.27 cm, 1.0 Torr	3.6994e+02	-5.1314e+03	1.7785e+04	7500	9500
Nerem 2.54 cm, 0.2 Torr	3.9690e+01	-4.7992e+02	1.4029e+03	7500	11000
Nerem 2.54 cm, 1.0 Torr	8.4075e+02	-1.1980e+04	4.2705e+04	7500	9100
Grusz. and War. 3.81 cm	0.0	1.2409e+03	-9.5198e+03	8000	10000
Grusz. and War. 2.54 cm	4.9975e+01	-2.4786e+02	-1.1403e+03	8000	10000

A. Hoshizaki Measurements

Shock tube measurements were performed by Hoshizaki[141] in the Lockheed Shock Tube on 2.87 cm diameter flat-faced cylinders. The shock velocity ranged from 7 – 8 km/s and the initial pressure was 1.16 Torr. The radiative intensity at the stagnation point of the flat-faced cylinder was made using a thin-film resistance gauge coated with carbon, which measured the intensity between 0 and 6 eV. These data are presented in Fig. 41 along with various predictions. Note that the uncertainty bars of +45.7% and −42% placed on the HARA/LAURA results are the combination of the parametric uncertainty result listed in Table 12 and the ±4% structural uncertainty value discussed previously. The baseline HARA/LAURA predictions are are tabulated in Table 14, along with the "Conditions Behind Moving Shock", which are the actual free stream conditions applied to the LAURA simulation. The species in the free-stream are assumed in chemical

equilibrium at these conditions. Also shown in the table are the "Conditions Behind Bow Shock", which are the conditions immediately behind the bow shock produced by the model. As discussed previously, the shock layer pressure for these cases is much higher than for the flight case. This makes up for the small shock layer thicknesses, which are listed in the table for each case, and results in radiative flux and intensities that are the same order-of-magnitude as the flight case. It is seen that the shock layer temperature for the 8 km/s case is 13,160 K, which approaches the 14,000 K temperatures of the 15 km/s flight case.

Table 14: Summary of Hoshizaki Simulations.

Initial Conditions		Conditions Behind Moving Shock			Conditions Behind Bow Shock			Radiation Predictions	
Velocity (km/s)	Pressure (N/m^2)	Temp. (K)	Density (kg/m^3)	Velocity (km/s)	Temp. (K)	Pressure (atm)	Stand-off (cm)	I (0–6 eV) ($W/cm^2/sr$)	% Error Bar Overlap
7.0	154.6	6780	2.75e-2	6.54	10222	10.9	0.62	90.8	12.3
7.5	154.6	7084	2.86e-2	7.02	11780	13.0	0.63	442	63
7.7	154.6	7212	2.90e-2	7.22	12365	13.8	0.64	742	76
8.0	154.6	7416	2.94e-2	7.51	13160	15.1	0.64	1375	87

As described in Section XIII-B, the experimental data were curve-fit to Eq. 10, which resulted in the coefficients and temperature limits listed in Table 13. The curves in Fig. 41 labelled "Data Fit+35%" and "Data Fit-35%" represent this curve fit plotted with a 35% increase and decrease, respectively. These two curves form the "Data Fit Limits" discussed in Section XIII-B, which are used to obtain the percent overlap presented in Table 14.

Fig. 41 and Table 14 show that there is an error bar overlap greater than zero for each prediction. Except for the 7.0 km/s case, the error bar overlap is greater than 50%. Note that the DPLR/NEQAIR results in this figure are contained within the HARA/LAURA error bars. However, this is not required to validate the error bars because both of these other analyses contain structural uncertainties not present in the HARA/LAURA results (the DPLR/NEQAIR results do not contain radiation coupling while the Sutton results consist of an inviscid flowfield analysis).

B. Thomas and Menard Measurements

Shock tube measurements were performed by Thomas and Menard[142] in the JPL Shock Tube on 3.18 cm diameter flat-faced cylinders. The shock velocity ranged from 6.9 – 9.3 km/s and the initial pressure was 0.25 Torr. The radiative intensity at the stagnation point of the flat-faced cylinder was made using a thin-film resistance gauge coated with carbon, which measured the intensity between 0 and 6 eV. These data are presented in Fig. 42 along with various predictions. The HARA/LAURA predictions, shown in this figure with the error bars computed and listed in Table 12, are tabulated in Table 15.

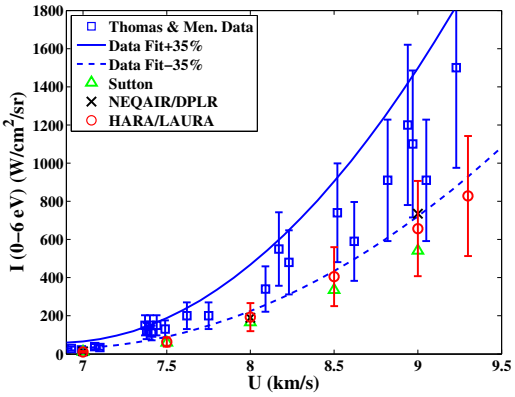

Figure 42: Comparison between intensity measurements and predictions for the Thomas and Menard cases.

Fig. 42 and Table 15 show that there is an error bar overlap greater than zero for each prediction above 7.5 km/s. This result is similar to the Hoshizaki case, where the agreement got better as the velocity increased. The relatively good agreement at higher velocities is encouraging because these cases contain the higher temperatures of interest for the flight cases. The similarity between the radiative flux environment for these cases and the flight cases were shown previously in Fig. 37. The good comparison between the radiative flux below 6 eV for the 15 km/s flight case and 9 km/s Thomas and Menard case was shown in Figs. 38 and 39.

C. Nerem Measurements

Shock tube measurements were performed by Nerem[143] in the Ohio State Shock Tube on 1.27 and 2.54 cm radius spheres. The shock velocity ranged from 5 – 11 km/s at initial pressures of 0.2 and 1.0 Torr.

Table 15: Summary of Thomas and Menard Simulations.

Initial Conditions		Conditions Behind Moving Shock			Conditions Behind Bow Shock			Radiation Predictions	
Velocity (km/s)	Pressure (N/m^2)	Temp. (K)	Density (kg/m^3)	Velocity (km/s)	Temp. (K)	Pressure (atm)	Stand-off (cm)	I (0–6 eV) ($W/cm^2/sr$)	% Error Bar Overlap
7.0	33.3	6293	6.31e-3	6.56	9710	2.54	0.67	10.8	0
7.5	33.3	6560	6.58e-3	7.05	11200	2.98	0.69	63.1	0
8.0	33.3	6858	6.78e-3	7.54	12360	3.54	0.69	194	29
8.5	33.3	7238	6.87e-3	8.01	13290	4.04	0.70	405	40
9.0	33.3	7849	6.77e-3	8.48	14080	4.48	0.69	657	37
9.3	33.3	8450	6.57e-3	8.74	14450	4.60	0.69	828	34

The radiative intensity at the stagnation point of the sphere was made using a thin-film platinum gauge, which measured the intensity between 0 and 6 eV. These data are presented in Figs. 43 and 44 for the 1.27 cm cases at 0.2 and 1.0 Torr, respectively. Tables 16 and 17 list the results for these two cases. The agreement in Fig. 44 for the 1.0 Torr case is excellent, with an error bar overlap of greater than 50% for each case. For the lower pressure 0.2 Torr case in Fig. 43, the agreement is not as good, although the error bar overlap is greater than zero for each case. It should be mentioned that the 0.2 Torr case contains a non-neglgible region of thermochemical nonequilibrium behind the bow shock. This explains the large disagreement between the HARA/LAURA predictions and the NEQAIR/DPLR and Sutton results. The NEQAIR/DPLR results assumed a single temperature thermochemical nonequilibrium model while the Sutton results assumed chemical equilibrium.

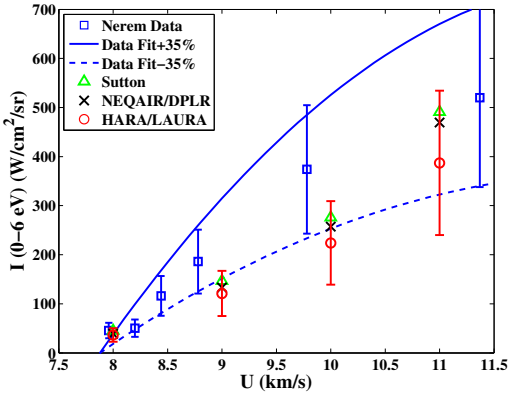

Figure 43: Comparison between intensity measurements and predictions for the 0.2 Torr (26.6 N/m^2), 1.27 cm radii Nerem cases.

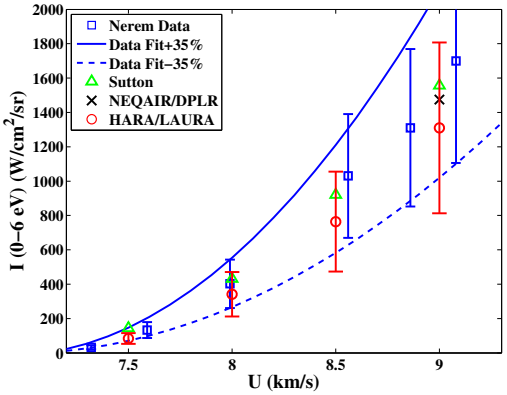

Figure 44: Comparison between intensity measurements and predictions for the 1.0 Torr (133.3 N/m^2), 1.27 cm radii Nerem cases.

Table 16: Summary of Nerem Simulations for the 1.27 cm radii, 0.2 Torr Cases.

Initial Conditions		Conditions Behind Moving Shock			Conditions Behind Bow Shock			Radiation Predictions	
Velocity (km/s)	Pressure (N/m^2)	Temp. (K)	Density (kg/m^3)	Velocity (km/s)	Temp. (K)	Pressure (atm)	Stand-off (cm)	I (0–6 eV) ($W/cm^2/sr$)	% Error Bar Overlap
8.0	26.6	6782	5.46e-3	7.54	12200	2.7	0.17	36.5	100
9.0	26.6	7779	5.44e-3	8.48	13920	3.3	0.17	121	17
10.0	26.6	9844	4.99e-3	9.37	15180	4.1	0.16	224	33
11.0	26.6	11156	4.99e-3	10.3	16500	4.9	0.15	387	72

For the 2.54 cm cases, Figs. 45 and 46 present the comparisons between predictions and measurements at 0.2 and 1.0 Torr, respectively. The HARA/LAURA results are also listed in Tables 18 and 19. The conditions behind the moving shock and bow shock are not listed in these tables because they are the same as those listed in Tables 16 and 17. As with the 1.27 cm cases, the 1.0 Torr comparison is better than the 0.2 Torr comparison, and the error bar overlap is greater than zero for all cases. In fact, it is greater than 40% for all cases.

Table 17: Summary of Nerem Simulations for the 1.27 cm radii, 1.0 Torr Cases.

Initial Conditions		Conditions Behind Moving Shock			Conditions Behind Bow Shock			Radiation Predictions	
Velocity (km/s)	Pressure (N/m^2)	Temp. (K)	Density (kg/m^3)	Velocity (km/s)	Temp. (K)	Pressure (atm)	Stand-off (cm)	I (0–6 eV) ($W/cm^2/sr$)	% Error Bar Overlap
7.5	133	7030	2.48e-3	7.03	11640	10.9	0.16	86.7	74
8.0	133	7359	2.55e-3	7.50	13140	13.2	0.16	353	82
8.5	133	7757	2.59e-3	7.99	14270	15.1	0.16	779	83
9.0	133	8330	2.58e-3	8.45	15240	16.6	0.16	1354	83

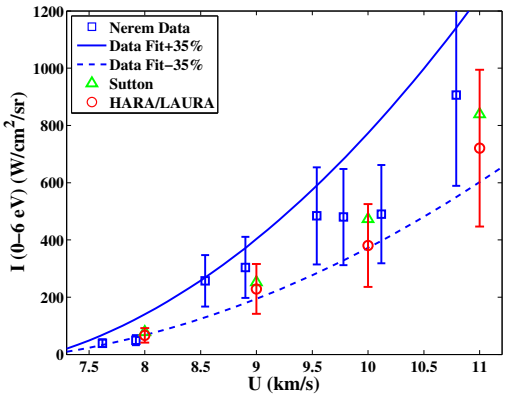

Figure 45: Comparison between intensity measurements and predictions for the 0.2 Torr (26.6 N/m^2), 2.54 cm radii Nerem cases.

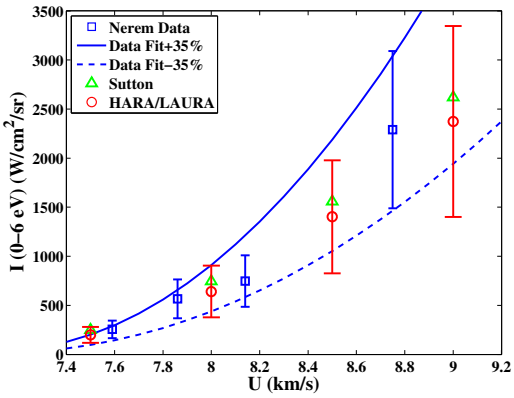

Figure 46: Comparison between intensity measurements and predictions for the 1.0 Torr (133.3 N/m^2), 2.54 cm radii Nerem cases.

Table 18: Summary of Nerem Simulations for the 2.54 cm radii, 0.2 Torr Cases.

Initial Conditions		Radiation Predictions	
Velocity (km/s)	Pressure (N/m^2)	I (0–6 eV) ($W/cm^2/sr$)	% Error Bar Overlap
8.0	26.6	66.5	48
9.0	26.6	229	70
10.0	26.6	380	53
11.0	26.6	720	72

Table 19: Summary of Nerem Simulations for the 2.54 cm radii, 1.0 Torr Cases.

Initial Conditions		Radiation Predictions	
Velocity (km/s)	Pressure (N/m^2)	I (0–6 eV) ($W/cm^2/sr$)	% Error Bar Overlap
7.5	133	199	52
8.0	133	641	89
8.5	133	1402	80
9.0	133	2374	72

D. Gruszczynski and Warren Measurements

Shock tube measurements were performed by Gruszczynski and Warren[144] in the General Electric Shock Tube on 2.57 cm radius spheres and 3.81 cm diameter flat-faced cylinders. The shock velocity ranged from 8.5 – 9.6 km/s at an initial pressure of 0.33 Torr. The radiative intensity at the stagnation point was made using a thin-film platinum gauge, which measured the intensity between 0 and 6 eV. These data are presented in Figs. 47 and 48 for the 1.27 cm cases at 0.2 and 1.0 Torr, respectively. Tables 20 and 21 list the results for these two cases. The agreement is excellent for both, with an error bar overlap of greater than 50% for every velocity except the 8 km/s flat-faced cylinder case.

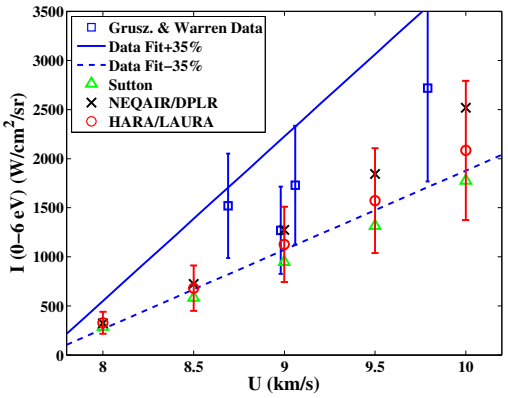

Figure 47: Comparison between intensity measurements and predictions for the 3.81 cm diameter flat-faced cylinder Gruszczynski and Warren cases.

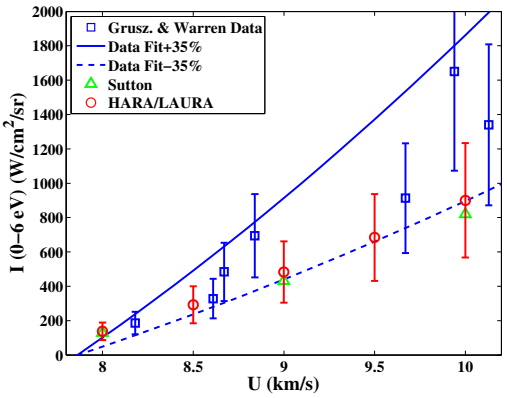

Figure 48: Comparison between intensity measurements and predictions for the 2.54 cm radius sphere Gruszczynski and Warren cases.

Table 20: Summary of Gruszczynski and Warren Simulations for the 3.81 cm diameter flat-faced cylinder.

Initial Conditions		Conditions Behind Moving Shock			Conditions Behind Bow Shock			Radiation Predictions	
Velocity (km/s)	Pressure (N/m^2)	Temp. (K)	Density (kg/m^3)	Velocity (km/s)	Temp. (K)	Pressure (atm)	Stand-off (cm)	I (0–6 eV) (W/cm^2/sr)	% Error Bar Overlap
8.0	44.0	6954	8.84e-3	7.53	12510	4.63	0.84	328	78
8.5	44.0	7337	8.97e-3	8.00	13470	5.31	0.84	680	53
9.0	44.0	7937	8.85e-3	8.47	14290	5.85	0.83	1127	57
9.5	44.0	8984	8.42e-3	8.92	14980	6.22	0.81	1572	59
10.0	44.0	10018	8.13e-3	9.36	15150	6.25	0.82	2084	65

Table 21: Summary of Gruszczynski and Warren Simulations for the 2.54 cm radius sphere.

Initial Conditions		Radiation Predictions	
Velocity (km/s)	Pressure (N/m^2)	I (0–6 eV) (W/cm^2/sr)	% Error Bar Overlap
8.0	44.0	135	13
8.5	44.0	290	76
9.0	44.0	483	62
9.5	44.0	684	55
10.0	44.0	900	51

XV. Comparisons with Constricted-Arc Emission Measurements

Constricted-arc experiments exist in the literature [153–159] that measure the radiative emission between 0 and 6 eV from a small column of equilibrium gas at temperatures up to 15,000 K and pressures of 1 atm. These conditions are relevant to the inviscid region of a Mars-return shock layer, and are therefore ideal for the present study. This section will compare the HARA predictions, including uncertainties, to these constricted-arc measurements.

The chemical equilibrium solver included in LAURA is used to compute the equilibrium composition. The same thermodynamic properties used in the LAURA flowfield properties are applied for these cases. A constant property layer of 0.2 cm is assumed to compute the radiative intensity for these cases. This length approximates the column of gas measured in the constricted-arc. The emission (J) is computed from this intensity (I) as $J = I/\Delta z$. The present comparisons are essentially independent of Δz because only the 0–6 eV range is considered, which is nearly optically thin.

Comparisons between the present HARA solutions and the experimental measurements are presented in Figs. 49 and 50 for the air and N_2 cases, respectively. The error bars on the HARA results will be discussed

in the following paragraph. Note that as for the shock tube cases, the "Data Fit" limits are computed from a least squares fit to the experimental data. The coefficients for these curve fits (defined in Eq. (10)) are a_1 =8.2525e-06, a_2 = −1.6055e-01, and a_3 =7.9872e+02 for the air case and a_1 =7.5730e-06, a_2 = −1.3445e-01, and a_3 =5.9129e+02 for the N_2 case. Excellent agreement is seen in these figures between the HARA solutions and the experimental data. The percent overlap is greater than 50% for temperatures greater than 10,000 K. This encouraging result provides confidence in the present equilibrium chemistry and radiation modeling.

The parametric uncertainty results for the air cases are listed in Table 22. Although the total uncertainty value is nearly constant at around +30% and −20% for the range of temperatures, it is the result of varying uncertainty contributors. Increased contributions from atomic photoionization, Opacity Project lines, and photoionization edge shift with increased temperature are offset by the decreased atomic line and negative ion photodetachment contributions.

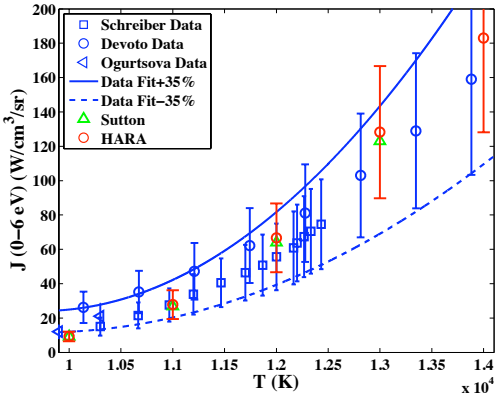

Figure 49: Comparison of HARA results with constricted-arc measurements for air.

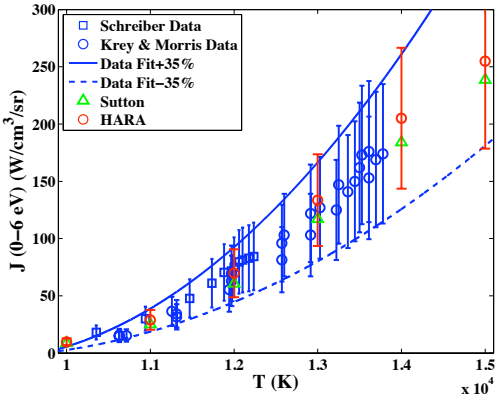

Figure 50: Comparison of HARA results with constricted-arc measurements for N_2.

Table 22: Summary of parametric uncertainty contributors for constricted-arc air cases.

Parameter Group	10,000 K	11,000 K	12,000 K	13,000 K	14,000 K	15,000 K
Air: Molec. Bands	0.42 (0.42)	0.14 (0.14)	0.05 (0.05)	0.02 (0.02)	0.01 (0.01)	0.01 (0.01)
Air: Atomic Lines	11.0 (11.4)	11.5 (12.1)	11.4 (11.9)	10.9 (11.4)	10.5 (10.7)	9.88 (10.1)
Air: Atomic Photoionization	1.76 (1.76)	2.45 (2.44)	3.10 (3.09)	3.69 (3.68)	4.21 (4.20)	4.66 (4.64)
Air: Opacity Project Lines	5.91 (0.00)	7.69 (0.00)	8.06 (0.00)	8.51 (0.00)	9.19 (0.00)	9.80 (0.00)
Air: Neg. Ion Photodetach.	6.71 (6.71)	4.86 (4.86)	3.41 (3.41)	2.32 (2.32)	1.52 (1.52)	0.90 (0.95)
Ion. Potential Lowering	4.10 (0.00)	1.90 (0.00)	0.00 (0.80)	0.00 (3.2)	0.00 (6.42)	0.00 (9.87)
Photo. Edge Shift	1.70 (0.00)	2.69 (0.00)	3.39 (0.00)	4.30 (0.00)	4.60 (0.00)	4.30 (0.00)
Total	31.6 (20.2)	31.2 (19.5)	29.4 (19.3)	29.7 (20.6)	30.0 (22.9)	29.6 (25.6)

XVI. Summary of Part II

The radiation and flowfield simulation approach and uncertainty analysis presented in Part I of this work were applied to experimental shock tube and constricted-arc cases. These experiments measured the frequency-integrated radiative intensity between 0 and 6 eV at shock layer temperatures and radiative intensity values relevant to a Mars-return shock layer. Comparisons between the simulations, including computed uncertainty bars, and measurements showed good agreement for a range of conditions and experiments. This indicates that the present simulation and uncertainty approaches provide credible results, and supports the legitimacy of the parametric uncertainty results computed in Part I for the flight cases.

Part III
Comparisons with EAST Measurements

XVII. Introduction to Part III

Part III takes the simulation and uncertainty approaches presented in Part I of this study and applies them to recent measurements made in the EAST shock tube.[146,160] These experiments measured the spectrally-dependent intensity behind shocks moving between 8.5 and 11.5 km/s at 0.2 Torr, which result in post shock temperatures between roughly 7,200 and 12,000 K. Although these temperatures are lower than those present for a 15 km/s Mars-return case, the frequency-dependent nature of the EAST measurements provides insight into the differences between predicted and measured total radiative intensity. The purpose of Part III is the same as Part II, which is to show that the error bars computed for the radiative intensity overlap the measurement error bars. As was discussed in Part II, this measure of agreement quality is considered because the computed uncertainty is based on an interval analysis.

The present work is an extension of the study of Brandis et al.,[161] who presented comparisons between the Hara and NEQAIR radiation codes and the presently considered EAST measurements. The focus of that work was the uncertainty and scatter of the EAST measurements, as well as the code differences between Hara and NEQAIR. The present work will apply the measurement curve fits and error bars computed by Brandis et al., but will focus on the parametric uncertainty of the Hara code and its agreement with the EAST data. These comparisons will be presented in a format similar to that applied in Part II for the 1960s era shock tube data, with curve fits to the data being compared to the predictions for a range of shock velocities. Unlike the comparisons in Part II, where only the frequency integrated intensity between 0 – 6 eV was available, the present comparisons will be made for both the frequency integrated and frequency dependent intensity in four wavelength ranges (129 – 178 nm, 338 – 470 nm, 730 – 890 nm, and 890 – 1440 nm), which cover the 0 – 10.2 eV range. This ability to look at spectral details will allow disagreements between the measured and predicted intensity to be isolated to individual spectral details, such as an atomic line.

Previous studies of earlier EAST measurements[145] were performed by Johnston[162] and Bose et al.,[163] among others. These studies were limited to a few cases that contained limited spectral coverage. In addition to the numerous shots made since these previous studies, recent advances in the EAST measurement techniques[146] have resulted in more complete spectral coverage. This significant increase in the spectral range and number of shots has motivated the present study.

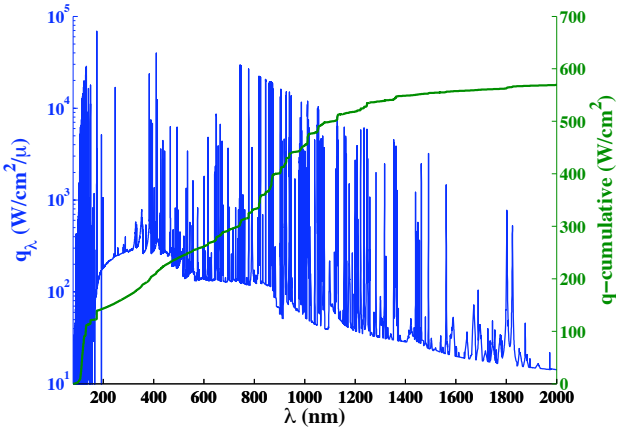

Figure 51: Radiative flux spectrum at the wall for a 5 m sphere at 11 km/s and a density of 3.0e-4 kg/m^3.

As stated previously, the purpose of this work is to apply the simulation and uncertainty approaches presented in Part I of this study to EAST measurement cases, which will allow the legitimacy of the uncertainty analysis to be assessed. The relevance of the considered experiments to the actual flight cases is discussed in Section XVIII. An overview of the EAST measurements is presented in Section XIX. A brief review of the uncertainty analysis and a discussion of important parameters for experimental data comparisons are presented in Section XX. This section also compares the present predictions with EAST shock tube measurements. Uncertainty analyses are presented for many of the simulations to provide error bars for the comparisons with measurements.

XVIII. Relevance of 0.2 Torr EAST Cases to Flight

The Mars-return flight conditions considered in Part I consisted of a free-stream density and temperature of of 3.0×10^{-4} kg/m^3 and 276 K, respectively. This represents a free-stream pressure of 0.18 Torr, which

closely matches the 0.2 Torr EAST measurements considered here. The EAST shock tube has a diameter of 10.16 cm. This diameter is the path length for the radiative transfer computation, which is about half of the stagnation point shock standoff for the non-ablating 5 m radius Mars return case. This difference in path length should not change the important contributors to the radiation transport. The shock velocities for the EAST measurements are less than 12 km/s, which are low compared to the 13 – 15 km/s velocities relevant to a Mars return. As a result, the present comparisons will not consider the high temperature phenomena ($T > 13,000$ K), discussed in Part I, resulting from velocities greater than 13 km/s. Note that these phenomena were considered in the 1960s era shock tube data studied in Part II of this work. However, unlike Part II, the present comparisons will provide detailed spectral comparisons, which provide valuable information regarding the source of disagreements between predictions and experiments.

The present comparisons with EAST data are most relevant to the 5 m radius, 11.0 km/s case at 3.0×10^{-4} kg/m^3 and 276 K. The uncertainties for this case were presented in Section VIII. The radiative flux spectrum at the stagnation point for this case is presented in Fig. 51. The four wavelength ranges (129 – 178 nm, 338 – 470 nm, 730 – 890 nm, and 890 – 1440 nm) considered in the EAST data cover 60% of the stagnation point radiative flux for this 11 km/s case (15% of the remaining flux is below 129 nm). The stagnation line temperature, pressure, and percent ionization are presented in Figs. 52 and 53. These results include radiation and ablation coupling. The peak vibrational-electronic temperature (T_{ve}) is 11,100 K, while the post-shock pressure is 0.34 atm. This pressure is about half of the 15 km/s result presented in Fig. 8 of Part I. The peak percent ionization is 10% for this case, which is less than one-third of the 15 km/s result. Overall, the comparisons with EAST measurements near 11 km/s are relevant to the Mars return cases near 11 km/s.

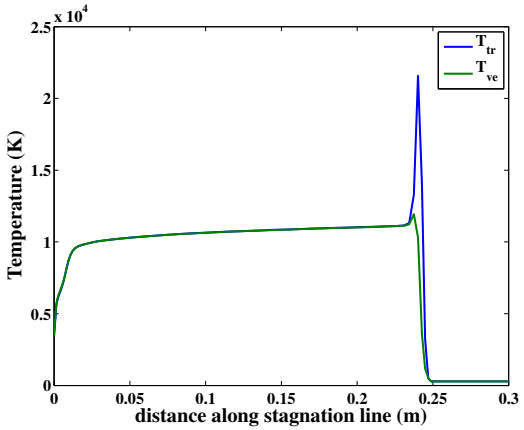

Figure 52: Stagnation line temperatures for the 11 km/s case.

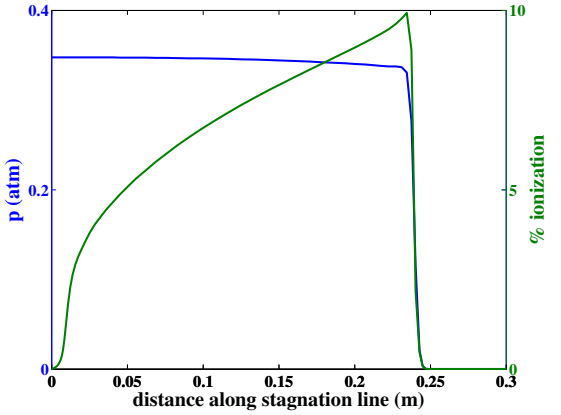

Figure 53: Stagnation line pressure and percent ionization for the 11 km/s case.

XIX. EAST Measurement Overview

The EAST shock tube measurements considered in this work are taken from Cruden et al.[146,160] The measurements from the EAST facility consist of intensity rays normal to the shock tube axis and behind the moving shock. These measurements are fundamentally different than the 1960s era shock tube measurements considered in Part II, which consisted of frequency integrated radiative flux measurements to a small body placed in the shock tube. The EAST measurements provide spatial profile data behind the moving shock as well as frequency dependent intensity data. This information, although more difficult to obtain, provides valuable insight into nonequilibrium processes, the individual contribution of various radiative mechanisms, and temperature data through line shape studies. The second of these, the insight into various radiative mechanisms, will be utilized in the present study. The intensity values in the apparent equilibrium post shock regions are considered in this work. These data were curve-fit as a function of velocity using the following equation:

$$DataFit = a_1 x^{a_2} \tag{10}$$

where x is the velocity in km/s and the coefficients a_i are listed in Table 23. It will be shown that the data scatter is nearly completely bounded by ±35% limits on the curve fits. These limits, referred to here as

"Data Fit Limits" in the same manner as Part II, will be plotted for each case.

Table 23: Curve-fit coefficients for the experimental Data Fit curves defined by Eq. (10).

λ Range	a_1	a_2
129 - 178 nm	5.459797E-16	15.060330
338 - 470 nm	2.917811E-13	11.726380
730 - 890 nm	2.886236E-13	12.328360
890 - 1440 nm	9.777360E-13	11.927280

For each comparison between experiment and prediction, the chosen measure of quality is the percent overlap of the predicted uncertainty bars with the Data Fit Limits defined in the previous paragraph. This overlap is illustrated in Fig. 40 of Part I, which shows a 76% overlap between the LAURA/HARA uncertainty bar and the band created by the Data Fit Limits. The choice of this overlap as the measure of prediction quality is based on the fact that the prediction uncertainty bars are obtained from an interval analysis. This "% Error Bar Overlap" will be reported for a range of velocities in each spectral range.

XX. HARA Uncertainty Analysis in Each Spectral Range

To determine if uncertainties in the radiation code modeling parameters are responsible for the disagreements with EAST data, the present section applies a parametric uncertainty analysis to the HARA code for each spectral range. The details of the applied uncertainty analysis are the same as those presented in Part I and applied to the flight case and 1960s era shock tube data. This analysis assumes interval uncertainties for all parameters. The present analysis considers only uncertainties in the radiation code, therefore ignoring the ionization potential lowering influence on the equilibrium chemistry. As mentioned previously, four spectral ranges will be considered here: 129 – 178 nm, 338 – 470 nm, 730 – 890 nm, and 890 – 1440 nm.

A. The 129 - 178 nm Wavelength Range (VUV)

The 129 – 178 nm range accounts for 9% of the total stagnation point radiative flux for the 11 km/s entry case. The main emission contributors in this spectral range are the 5 atomic nitrogen line multiplets listed in Table 24, which were identified and studied in detail by Johnston et al.[46] The uncertainties in the line oscillator strengths and Stark broadening widths determined by Johnston et al. are listed in Table 24 and are applied in the present uncertainty analysis. Note that each of the line multiplets listed here contains multiple individual lines. The uncertainties listed are applied to all individual lines in a multiplet. The influence of all lines in a multiplet are summed when the uncertainty from a multiplet is reported in the following discussion.

Table 24: Strongest nitrogen line multiplets between 129 and 178 nm.

Wiese ID*	$\lambda_{CL,mult}$ (nm)	$\pm f_{ij}$ (%)	$\pm\Delta\lambda_{S,0}$ (%)
35	131.07	60	30
32	131.95	20	30
30	141.19	20	100
15	149.33	10	30
29	174.36	20	50

* Multiplet number listed by Wiese et al.[82]

An example of the comparison between HARA predictions and EAST measurements in this spectral range is shown in Fig. 54. Except for some weak lines that are likely due to non-air contaminates, all major spectral features are predicted by HARA. The integrated intensity predicted by HARA is 2% higher than the EAST measurements for this case. As will be shown, this uncertainty is less than the uncertainty in the predictions. Note that the lines near 149 and 174 nm are slightly over-predicted, which is possibly a result of boundary layer absorption not being treated in the predictions or the uncertainties in the Stark broadening and oscilator strength uncertainties listed in Table 24. The over-prediction of these lines is seen to be cancelled in the integrated intensity by the contribution from contaminates. This indicates that the 2% disagreement for this spectral range is misleading, and without the contaminate contributions the over-prediction is 7%.

A breakdown of the HARA uncertainty results at 9, 10, and 11 km/s is presented in Table 25. The rows in this table each refer to a specific group of uncertainty parameters: "Molec. Bands" refers to the uncertainty resulting from all molecular band oscillator strength uncertainties; "Atomic Lines: $f_{i,j}$" from all atomic line oscillator strength uncertainties; "Atomic Lines: $\Delta\lambda_{S,0}$" from all atomic line Stark broadening width uncertainties; "Atomic Photoionization" from all atomic photoionization cross section uncertainties; "Opacity Project Lines" from all Opacity Project line uncertainties; "Neg. Ion Photodetach." from all

negative ion photodetachment cross section uncertainties; and "Photo. Edge Shift" refers to the contribution from the photoionization edge shift. As expected, this table shows the increase in the uncertainty contribution from atomic lines as the velocity increases, along with a decrease in the molecular band contribution. The first 3 rows, resulting from molecular bands and atomic lines, represent the major uncertainty contributors for all velocities in this spectral range. This indicates the small radiative emission contribution from atomic photoionization, Opacity Project lines, and negative ion photodetachment between 129 – 178 nm. A list of the individual uncertainty contributors for this spectral range is presented in Table 26. As in Table 25, the positive uncertainties are listed first while the negative uncertainties are listed second in parenthesis. Also, these values represent the percent uncertainty of the integrated intensity in this spectral range. It is seen that the 149 and 174 nm lines, which were noted previously to account for the largest disagreement in this spectral range, contribute more than ±10% to the parametric uncertainty.

Table 25: Summary of parametric uncertainty contributors for the 129 – 178 nm range. The positive uncertainties are listed first while the negative uncertainties are listed second in parenthesis.

Parameter Group	9 km/s	10 km/s	11 km/s
Molec. Bands	4.19 (4.19)	0.26 (0.26)	0.05 (0.05)
Atomic Lines: $f_{i,j}$	4.67 (5.87)	9.10 (10.7)	9.68 (10.8)
Atomic Lines: $\Delta\lambda_{S,0}$	4.65 (5.79)	17.3 (17.0)	19.3 (17.9)
Atomic Photoionization	0.01 (0.01)	0.14 (0.13)	0.27 (0.27)
Opacity Project Lines	0.14 (0.00)	0.35 (0.00)	0.38 (0.00)
Neg. Ion Photodetach.	0.26 (0.26)	0.62 (0.62)	0.65 (0.65)
Photo. Edge Shift	0.00 (0.00)	0.00 (0.00)	0.00 (0.00)
Total	13.9 (16.1)	27.8 (28.7)	30.3 (29.7)

Table 26: Top 7 uncertainty contributions to the 129 – 178 nm range from individual parameters for the 11 km/s case.

Rank	Parameter	Uncertainty (±%)	$\pm J_c$ (%)
1	$\Delta\lambda_{S,0}$ (N) – 174.36 nm	50	4.96 (5.34)
2	$\Delta\lambda_{S,0}$ (N) – 149.33 nm	30	3.17 (3.82)
3	$\Delta\lambda_{S,0}$ (O) – 130.35 nm	50	2.49 (3.14)
4	f_{ij} (N) – 174.36 nm	20	2.16 (2.07)
5	$\Delta\lambda_{S,0}$ (N) – 141.19 nm	100	1.55 (2.01)
6	f_{ij} (N) – 149.33 nm	10	1.32 (1.31)
7	f_{ij} (N) – 131.07 nm	60	1.22 (1.59)

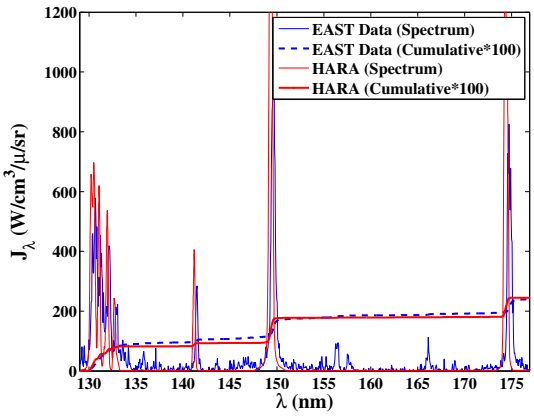

Figure 54: Comparison between HARA predictions and EAST measurements for a 10.94 km/s, 0.2 Torr case (Shot 92).

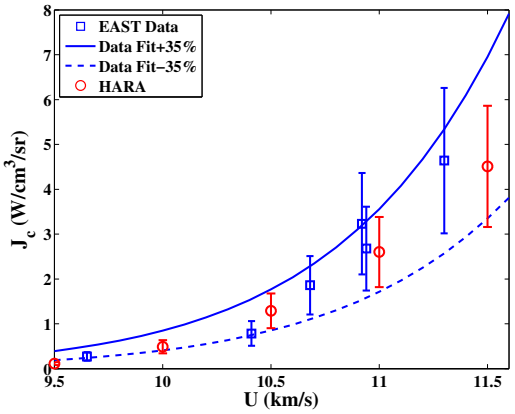

Figure 55: Comparison between 129 - 178 nm integrated intensity predicted by HARA and measured in EAST at 0.2 Torr and in equilibrium.

Comparisons between predictions and EAST measurements in the 129 – 178 nm range are presented in Fig. 55. It is seen that the HARA predictions compare well for the entire range of velocities. These predictions are also listed in Table 27, along with the % Error Bar Overlap. Except for the 9.5 km/s case, the % Error Bar Overlap is greater than 78% for all cases. This good agreement provides confidence in the present baseline computational approach and uncertainty analysis. Note that Brandis et al.,[161] discusses the poor agreement seen here for velocities below 10 km/s.

Table 27: Predicted J_c values and the % Error Bar Overlap between 129 – 178 nm.

Velocity (km/s)	J_c (W/cm^3/sr)	% Error Bar Overlap
9.5	0.11	0
10.0	0.49	78
10.5	1.29	100
11.0	2.60	100
11.5	4.52	93

B. The 338 – 470 nm Wavelength Range (UV)

The 338 – 470 nm range accounts for 9% of the total stagnation point radiative flux for the 11 km/s entry case. The main emission contributors in this spectral range are the N_2^+ 1– band system and the atomic nitrogen photoionization continuum (σ_{bf}). As discussed in Part I, the

uncertainty for the N_2^+ 1– oscillator strength (N_2^+ 1- f_{ij}) was chosen as ±10%, while the atomic nitrogen photoionization cross section uncertainties were chosen as ±20%. The negative ion photodetachment cross section for nitrogen may also contribute in this spectral range, depending on the highly uncertain cross section applied. A ±100% uncertainty is applied for the negative ion photodetachment cross section (σ^-).

A breakdown of the HARA uncertainty results at 9, 10, and 11 km/s is presented in Table 28, which is structured identically to Table 25. The uncertainty contributors for this spectral range are seen to be considerably different than for the previous 129 – 178 nm range. The Stark broadening contribution ($\Delta\lambda_{S,0}$) is seen to be less than one percent, unlike the previous range where this contributions was nearly 20% at 11 km/s. Conversely, the Opacity Project Lines and Negative Ion Photodetachment contributions are significant in the 338 – 470 nm range, while their contributions were negligible for the previous range. The individual uncertainty contributors in the 338 – 470 nm range are presented in Table 29. The negative ion photodetachment cross section (σ^-) for nitrogen is by far the greatest individual contributor. A number of photoionization cross sections and atomic line oscillator strengths are present in this list, but each contribute less than 2% to the total uncertainty.

Table 28: Summary of parametric uncertainty contributors for the 338 – 470 nm range.

Parameter Group	9 km/s	10 km/s	11 km/s
Molec. Bands	8.78 (8.78)	2.88 (2.88)	0.80 (0.79)
Atomic Lines: $f_{i,j}$	0.36 (0.36)	3.77 (3.70)	5.00 (4.85)
Atomic Lines: $\Delta\lambda_{S,0}$	0.00 (0.00)	0.16 (0.19)	0.26 (0.22)
Atomic Photoionization	0.39 (0.39)	6.24 (6.22)	10.1 (10.1)
Opacity Project Lines	0.73 (0.00)	7.99 (0.00)	10.8 (0.00)
Neg. Ion Photodetach.	7.93 (7.93)	21.5 (21.5)	15.0 (15.0)
Photo. Edge Shift	0.15 (0.00)	2.97 (0.00)	4.92 (0.00)
Total	18.3 (17.5)	45.5 (34.4)	46.9 (30.9)

Table 29: Top 10 uncertainty contributions to the 338 – 470 nm range from individual parameters for the 11 km/s case.

Rank	Parameter	Uncertainty (±%)	$\pm J_c$ (%)
1	σ^- (N^-)	100	15.0 (15.0)
2	σ_{bf} (N, level 8)	20	1.72 (1.72)
3	f_{ij} (N) – 410.8 nm	25	1.02 (1.03)
4	σ_{bf} (N, level 9)	20	0.85 (0.85)
5	σ_{bf} (N, level 17)	20	0.78 (0.78)
6	N_2^+ 1- f_{ij}	10	0.77 (0.77)
7	f_{ij} (N) – 382.9 nm	25	0.74 (0.73)
8	σ_{bf} (O, level 6)	20	0.69 (0.69)
9	f_{ij} (N) – 389.2 nm	25	0.60 (0.61)
10	σ_{bf} (N, level 18)	20	0.50 (0.50)

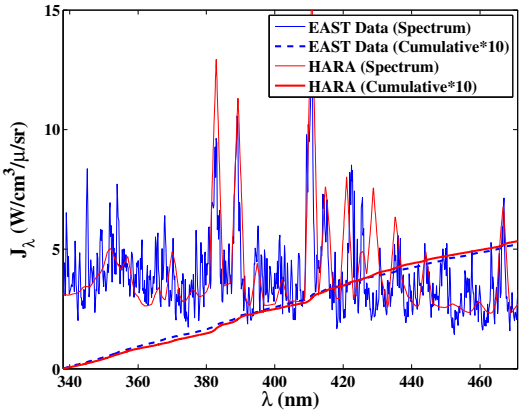

Figure 56: Comparison between HARA predictions and EAST measurements for a 10.92 km/s, 0.2 Torr case (Shot 33).

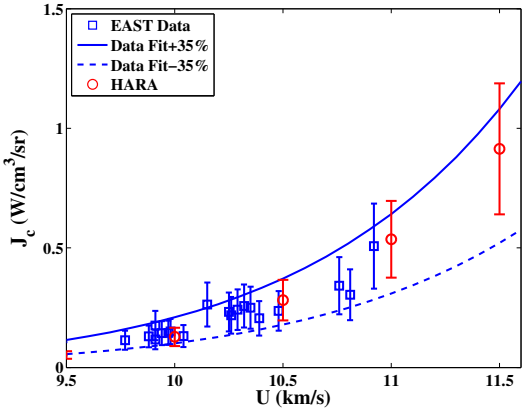

Figure 57: Comparison between 338 – 470 nm integrated intensity predicted by HARA and measured in EAST at 0.2 Torr and in equilibrium.

An example comparison between HARA predictions and EAST measurements in this spectral range is shown in Fig. 56. It is seen that all major spectral features are well in both shape and magnitude, except for two small features around 460 nm. The integrated intensity predicted by HARA is 2% larger than the EAST measurements for this case. Comparisons of the integrated intensity between 338 – 470 nm predicted by HARA and the EAST measurements are presented in Fig. 57 for a range of velocities. The predicted intensity values presented in this figure are listed in Table 30 along with the % Error Bar Overlap. Except for the 9.5 km/s case, the comparisons are excellent.

Table 30: Predicted J_c values and the % Error Bar Overlap between 338 - 470 nm.

Velocity (km/s)	J_c (W/cm³/sr)	% Error Bar Overlap
9.5	0.052	40
10.0	0.13	85
10.5	0.28	100
11.0	0.54	83
11.5	0.91	80

C. The 730 - 890 nm Wavelength Range

The 730 – 890 nm range accounts for 17% of the total stagnation point radiative flux for the 11 km/s entry case. The main emission contributors in this spectral range are the 4 atomic nitrogen line multiplets listed in Table 31, which were identified and studied in detail by Johnston et al.[46] The uncertainties listed in this table are applied in the present uncertainty analysis.

A breakdown of the HARA uncertainty results at 9, 10, and 11 km/s is presented in Table 32. This table shows that the atomic line oscillator strengths (Atomic Lines: f_{ij}) and Stark broadening widths (Atomic Lines: $\Delta\lambda_{S,0}$) are the largest contributors. Note that the total uncertainty for these cases is less than 19%, which is significantly less than for the previous 2 spectral ranges. This lower uncertainty is a consequence of the smaller Stark broadening uncertainty contribution than the 129 – 178 nm range and a smaller negative ion photodetachment contribution than the 338 – 470 nm range. The individual uncertainty contributors for this spectral range are listed in Table 33. As expected, the top 10 contributors are all atomic line oscillator strengths and Stark broadening widths. All 4 strong nitrogen lines listed in Table 31 are present in this table, along with 2 strong oxygen lines.

Table 31: Strongest nitrogen line multiplets between 730 and 890 nm.

Wiese ID*	$\lambda_{CL,mult}$ (nm)	$\pm f_{ij}$ (%)	$\pm\Delta\lambda_{S,0}$ (%)
48	745.42	10	30
47	821.41	10	30
52	861.98	10	30
46	869.40	15	30

* Multiplet number listed by Wiese et al.[82]

Table 32: Summary of parametric uncertainty contributors for the 730 – 890 nm range.

Parameter Group	9 km/s	10 km/s	11 km/s
Molec. Bands	0.23 (0.23)	0.01 (0.01)	0.00 (0.00)
Atomic Lines: $f_{i,j}$	8.66 (8.88)	6.54 (7.10)	6.56 (6.94)
Atomic Lines: $\Delta\lambda_{S,0}$	0.26 (0.71)	5.77 (7.09)	8.68 (11.2)
Atomic Photoionization	0.23 (0.23)	0.94 (0.94)	1.59 (1.59)
Opacity Project Lines	0.01 (0.00)	0.26 (0.00)	0.90 (0.00)
Neg. Ion Photodetach.	1.03 (1.03)	0.54 (0.54)	0.36 (0.36)
Photo. Edge Shift	0.07 (0.00)	0.26 (0.00)	0.49 (0.00)
Total	10.5 (11.1)	14.3 (15.7)	18.6 (20.1)

Table 33: Top 10 uncertainty contributions to the 730 – 890 nm range from individual parameters for the 11 km/s case.

Rank	Parameter	Uncertainty (±%)	$\pm J_c$ (%)
1	$\Delta\lambda_{S,0}$ (N) – 869.40 nm	30	2.31 (2.91)
2	$\Delta\lambda_{S,0}$ (N) – 821.41 nm	30	1.99 (2.55)
3	$\Delta\lambda_{S,0}$ (O) – 777.55 nm	50	1.93 (2.55)
4	f_{ij} (N) – 869.40 nm	15	1.79 (1.94)
5	f_{ij} (N) – 821.41 nm	10	1.14 (1.24)
6	$\Delta\lambda_{S,0}$ (N) – 745.42 nm	30	0.85 (1.08)
7	$\Delta\lambda_{S,0}$ (N) – 861.98 nm	30	0.77 (1.01)
8	$\Delta\lambda_{S,0}$ (O) – 844.88 nm	50	0.75 (0.98)
9	f_{ij} (N) – 861.98 nm	10	0.65 (0.69)
10	f_{ij} (N) – 745.42 nm	10	0.61 (0.64)

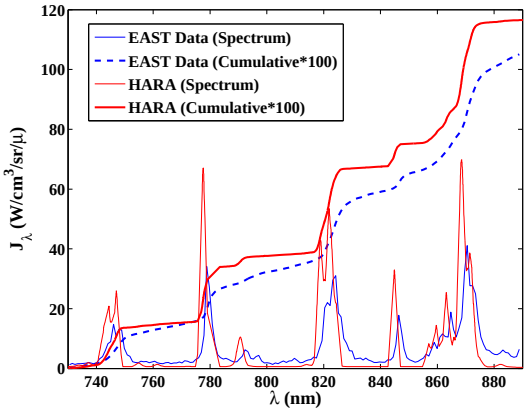

Figure 58: Comparison between HARA predictions and EAST measurements for a 10.48 km/s, 0.2 Torr case (Shot 98).

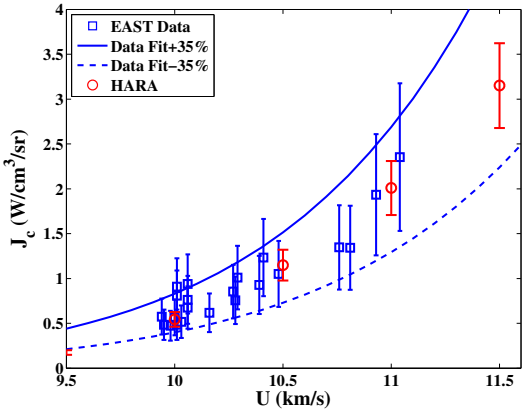

Figure 59: Comparison between 730 – 890 nm integrated intensity predicted by HARA and measured in EAST at 0.2 Torr and in equilibrium.

An example comparison between HARA predictions and EAST measurements in the 730 – 890 nm range is shown in Fig. 58. It is seen that the atomic line peaks are over-predicted but the underlying continuum is under-predicted. The resulting integrated intensity predicted by HARA is 14% larger than the EAST measurements for this case. Comparisons of the integrated intensity between 730 – 890 nm predicted by HARA and the EAST measurements are presented in Fig. 59 for a range of velocities. The predicted intensity values presented in this figure are listed in Table 34 along with the % Error Bar Overlap. The agreement

Table 34: Predicted J_c values and the % Error Bar Overlap between 730 – 890 nm.

Velocity (km/s)	J_c (W/cm^3/sr)	% Error Bar Overlap
9.5	0.17	0
10.0	0.54	100
10.5	1.15	100
11.0	2.01	100
11.5	3.15	100

between the predictions and measurements is seen to be excellent, with a 100% Error Bar Overlap for all velocities above 9.5 km/s.

D. The 890 – 1440 nm Wavelength Range (IR)

The 890 – 1440 nm range accounts for 25% of the total stagnation point radiative flux for the 11 km/s entry case, which makes it the most important of all the ranges studied here. The main emission contributors in this spectral range are the 15 atomic nitrogen line multiplets listed in Table 35.

A breakdown of the HARA uncertainty results at 9, 10, and 11 km/s is presented in Table 36 for the 890 – 1440 nm range. Similarly to the 730 – 890 nm range, atomic line oscillator strengths and Stark broadening widths are the largest uncertainty contributors. Unlike this previous spectral range, the Opacity Project lines and photoionization edge shift contribute noticeably to the uncertainty. The individual uncertainty contributors for this spectral range are listed in Table 37. Not surprisingly, the top 8 contributors are all atomic line oscillator strengths and Stark broadening widths. All lines listed here are present in Table 35.

A comparison between HARA predictions and EAST measurements in the 890 –1440 nm range is shown in Fig. 60. Although the atomic line peaks are over-predicted for some lines, the overall agreement is excellent. The resulting integrated intensity predicted by HARA is 5% lower than the EAST measurements for this case. Note that the over-prediction in the 900 – 1000 nm range is cancelled by an under-prediction in the 1100 – 1400 nm range. The largest difference comes from the over-prediction of the line at 1011 nm.

Table 35: Strongest nitrogen line multiplets between 890 and 1440 nm.

Wiese ID*	$\lambda_{CL,mult}$ (nm)	$\pm f_{ij}$ (%)	$\pm\Delta\lambda_{S,0}$ (%)
65	905.24	25	30
127	905.01	15	30
126	919.82	50	100
51	939.79	25	50
72	983.33	15	50
70	998.70	25	100
71	999.10	75	100
69	1011.7	10	50
80	1070.0	75	75
81	1052.6	10	75
68	1128.9	15	75
61	1160.0	25	100
100	1204.4	10	100
99	1246.9	15	100
114	1362.0	10	100

* Multiplet number listed by Wiese et al.[82]

Comparisons of the integrated intensity between 730 – 890 nm predicted by HARA and the EAST measurements are presented in Fig. 61 for a range of velocities. The predicted intensity values shown in this figure are listed in Table 38 along with the % Error Bar Overlap. At velocities less than 10.5 km/s, an under-prediction is seen, while agreement at higher velocities is excellent. Note that the majority of the EAST measurements are between 10.2 and 11.2 km/s, and in this range the comparisons with predictions are excellent. Outside of this velocity range, the curve fit to the data is an extrapolation, and therefore may not be accurate.

Table 36: Summary of parametric uncertainty contributors for the 890 – 1440 nm range.

Parameter Group	9 km/s	10 km/s	11 km/s
Molec. Bands	0.22 (0.22)	0.00 (0.00)	0.00 (0.00)
Atomic Lines: $f_{i,j}$	13.3 (13.6)	11.5 (12.1)	11.5 (12.0)
Atomic Lines: $\Delta\lambda_{S,0}$	0.20 (0.35)	5.02 (7.48)	6.63 (10.5)
Atomic Photoionization	0.25 (0.25)	0.73 (0.73)	1.08 (1.08)
Opacity Project Lines	1.67 (0.00)	4.87 (0.00)	6.91 (0.00)
Neg. Ion Photodetach.	1.50 (1.50)	0.48 (0.48)	0.25 (0.25)
Photo. Edge Shift	0.33 (0.00)	2.05 (0.00)	3.87 (0.00)
Total	17.4 (15.9)	24.7 (20.9)	30.2 (23.8)

Table 37: Top 8 uncertainty contributions to the 890 – 1440 nm range from individual parameters for the 11 km/s case.

Rank	Parameter	Uncertainty (±%)	$\pm J_c$ (%)
1	f_{ij} (N) – 919.82 nm	50	1.53 (1.30)
2	f_{ij} (N) – 1070.0 nm	75	1.00 (1.00)
3	$\Delta\lambda_{S,0}$ (N) – 939.79 nm	50	0.98 (1.48)
4	f_{ij} (N) – 1011.7 nm	10	0.82 (0.77)
5	$\Delta\lambda_{S,0}$ (N) – 1011.7 nm	50	0.81 (1.45)
6	f_{ij} (N) – 939.79 nm	25	0.78 (0.81)
7	f_{ij} (N) – 999.10 nm	75	0.68 (0.70)
8	$\Delta\lambda_{S,0}$ (N) – 1052.6 nm	75	0.55 (1.73)

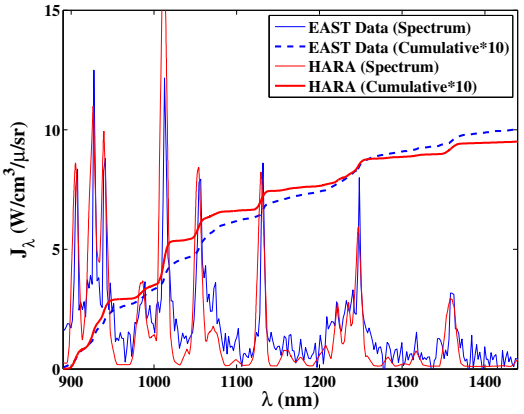

Figure 60: Comparison between HARA predictions and EAST measurements for a 10.29 km/s, 0.2 Torr case (Shot 29).

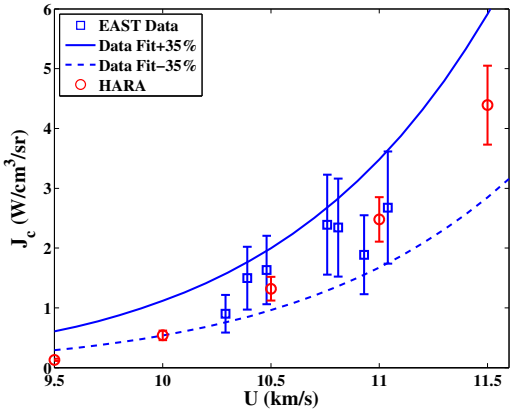

Figure 61: Comparison between 890 – 1440 nm integrated intensity predicted by HARA and measured in EAST at 0.2 Torr and in equilibrium.

Table 38: Predicted J_c values and the % Error Bar Overlap between 890 - 1440 nm.

Velocity (km/s)	J_c (W/cm^3/sr)	% Error Bar Overlap
9.5	0.13	0
10.0	0.54	51
10.5	1.32	100
11.0	2.48	100
11.5	4.39	100

XXI. Summary of Part III

The air radiation model and uncertainty analysis presented in Part I of this work are applied to EAST shock tube cases. The EAST measurements include the wavelength dependent intensity in four spectral ranges that span 129 – 1440 nm. This wavelength range captures 60% of the radiative flux for a 11 km/s entry at 60 km altitude. The measurements spanned a velocity between 9.5 – 11.5 km/s, which represents the low end of a Mars return entry, although the pressure of 0.2 Torr nearly matches the flight conditions. The predicted equilibrium radiation was found to fall within the scatter of the measurements for nearly all cases, which is roughly ±30%. The parametric uncertainty analysis applied to the predictions resulted in uncertainties ranging from 10 – 47 %, with the largest uncertainties predicted in the 338 – 470 nm range. The combination of the negative ion photodetachment, atomic photoionization, and Opacity Project lines contribute significant uncertainty in this wavelength range. In other wavelength ranges, the atomic line oscillator strengths and Stark broadening widths contribute significant uncertainty to the predictions. Overall, the comparisons presented in this paper provide confidence in the equilibrium air radiation predictions at temperatures near 11,500 K, and compliments the good agreement at higher temperatures seen in Part II.

Part IV
Summary and Future Work

XXII. Summary

The purpose of the this paper was to assess the radiative heating uncertainty for a Mars-return to Earth. In Part I, a baseline simulation approach that includes coupled ablation and radiation in the Laura flowfield code was presented. The Hara radiation code, which includes a smeared rotational band (SRB) treatment of molecular band systems and tangent slab radiation transport, was applied for the coupled radiation predictions. The SRB model was shown to result in only a ±2% uncertainty, although it required orders-of-magnitude less computational time than the rigorous line-by-line approach. Coupled ablation and radiation were shown to both reduce the radiative heating by nearly 50% at 15 km/s. A structural uncertainty of +34%, -24% was determined for the radiative heating. This structural uncertainty contains a +20% contribution to account for neglecting precursor heating and a -10% contribution for including simplified (tangent-slab) radiation transport in the baseline model. The precursor uncertainty was assessed by implementing a detailed precursor model in the Laura/Hara simulations. This computationally expensive analysis was shown to increase the radiative heating by 15% for the 15 km/s, 5 m radius case, although significant uncertainties exist in this precursor model (leading to the uncertainty choice of +20%). The radiation transport uncertainty was assessed by comparing the simplified tangent-slab approach applied in the baseline model to detailed (computational expensive) ray-tracing results. A parametric uncertainty analysis, which assumes interval uncertainties, was developed and presented in Section VII. This analysis treated uncertainties in the Hara radiation model as well as heat of formation uncertainties in the Laura flowfield model. Parametric uncertainties of around ±50% are predicted from this analysis. The largest uncertainty contributors are the C_3 Swings cross-section, photoionization edge shift, and Opacity Project atomic lines. Combining the parametric and structural uncertainties results in an uncertainty of +81.3% and −52.3% for the 15 km/s, 5 m radius Mars-return case. This is the recommended uncertainty for the Mars-return radiative heating resulting from this work.

In Part II, the radiation and flowfield simulation approach and uncertainty analysis presented in Part I was applied to 1960s era experimental shock tube and constricted-arc cases. These experiments measured the frequency-integrated radiative intensity between 0 and 6 eV at shock layer temperatures and radiative intensity values relevant to a Mars-return shock layer. No ablation was present in these experiments, therefore only the air uncertainties were considered in the simulations. Comparisons between the simulations, including computed uncertainty bars, and measurements showed good agreement for a range of conditions and experiments.

In Part III, the air radiation model and uncertainty analysis presented in Part I were applied to EAST shock tube cases. The EAST measurements include the wavelength dependent intensity in four spectral ranges that span 120 – 1400 nm. This wavelength range captures 73% of the radiative flux for a 11 km/s entry at 60 km altitude. The measurements spanned a velocity between 9.5 – 11.5 km/s, which represents the low end of a Mars return entry, although the pressure of 0.2 Torr nearly matches the flight conditions. These relatively low velocity conditions for Mars-return are considered because the measurements contain wavelength dependent data, which allows the contributions from individual radiative mechanisms to be studied. The predicted equilibrium radiation was found to fall within the scatter of the measurements for nearly all cases, which is roughly ±30%. The parametric uncertainty analysis applied to the predictions resulted in uncertainties ranging from 10 – 47 %, with the largest uncertainties predicted in the 338 – 470 nm range. The combination of the negative ion photodetachment, atomic photoionization, and Opacity Project lines contribute significant uncertainty in this wavelength range. In other wavelength ranges, the atomic line oscillator strengths and Stark broadening widths contribute significant uncertainty to the predictions. Overall, the comparisons presented in Part III provide confidence in the equilibrium air radiation predictions at temperatures near 11,500 K, and compliments the good agreement at higher temperatures seen in Part II.

The application of the baseline simulation and uncertainty approaches, presented in Part I, to the experimental cases in Parts II and III supports the legitimacy of the parametric uncertainty results computed in Part I for the flight cases. However, because these experimental cases contain no ablation, it was not possible to experimentally assess the uncertainties due to ablation products (from C_3, etc.) in these comparisons (although the ablation product uncertainties are contained in the parametric uncertainty analysis of the

flight case). This lack of ablation in experimental cases also restricted the influence of ablation on radiative heating to be experimentally verified. The small model size in Part II and the relatively low velocity in Part III restricted the influence of the radiative precursor from being experimentally assessed.

XXIII. Past Radiation Measurements with Ablation

As mentioned in the previous section, the lack of experimental measurements that capture the influence of massive ablation on radiative heating represents a significant weakness in the understanding of Mars-return radiative heating. Although there have been radiation measurements performed in ablating environments, none of these experiments have produced data of sufficient fidelity or at conditions with sufficient ablation to warrant a detailed analysis using the present uncertainty approach. Nevertheless, these past measurements are briefly discussed in this section for the purpose of guiding future studies.

Measurements by Georg and Yakushin[164–166] and Gudzovskii[167] considered the radiation in flowfields with ablating asbestos and graphite. Due to the limited information presented by Georg and Yakushin, the data presented in these papers was not suitable for comparison in the present work. Recent work by Schott et al.[168] consist of radiative intensity measurements at the stagnation point of an ablating model in an arcjet facility. This preliminary work shows promise but has not yet published quantitative results that would allow consideration in the present uncertainty assessment. Preliminary work by D'Souza et al.[169] measured the radiative intensity along the stagnation line to a small (3 cm radius) shock tube model with an ablating epoxy surface. This work is also promising but the difference between the epoxy surface and an actual ablating surface is significant, with the sublimation temperature of the epoxy around 600 K compared to the greater than 3200 K temperature for carbon phenolic.

The Apollo 4 flight experiment[170] consisted of the unmanned entry of an actual Apollo capsule at 10.8 km/s with an ablating Avcoat heatshield. A total radiometer was placed at the stagnation point to measure the spectrally-integrated radiative intensity below 6.2 eV. The ablation rates for this case were an order-of-magnitude lower than for the 15 km/s Mars-return case. The study by Johnston et al.[18] applied the same LAURA/HARA analysis considered in this work to the Apollo 4 peak heating condition at 10.2 km/s. The influence of ablation was shown to be less than 3% on the radiative intensity below 6 eV. Therefore, the Apollo 4 intensity data, which is also complicated by the radiometer being located in a cavity on the heatshield (which is difficult to simulate), is of limited value for assessing the influence of ablation on radiative heating. Nevertheless, note that Johnston et al. found agreement within 30% for the predicted and measured radiative intensity for Apollo 4. This agreement at low velocities is consistent with that shown in Part III.

The Stardust vehicle was a 0.229 m sphere-cone that entered the atmosphere at 12.6 km/s.[171] There were no instruments on the vehicle for measuring the radiative or convective heating experienced during reentry. However, the radiation emitted from the shock-layer and vehicle surface was measured by observation aircraft equipped with radiometers.[172] These radiometers measured the radiation between 1.4 and 3.0 eV. The difficulty in using these measurements to validate radiation models is that the measured radiative intensity consists of that from the vehicle surface and entire shock-layer. A review of these measurements and their comparison with predictions were presented by Liu et al.[173] Like the Apollo 4 case, the ablation rates for the Stardust case are an order-of-magnitude lower than for the 15 km/s Mars-return case. In fact, Liu et al. did not consider ablation products in their comparison with the observation data, which showed relatively good agreement between predictions and measurements.

XXIV. Suggested Future Work

The insufficiency of existing radiation data to an ablating surface was discussed in the previous section. There is clearly a need for radiation measurements to massively ablating surfaces to decrease the nearly $\pm 80\%$ radiative heating uncertainty for a Mars-return entry. This data is unlikely to come from a flight case, since even the Apollo 4 measurements at Lunar-return conditions did not contain enough ablation to influence the radiation significantly. The preliminary work by Schott et al.[168] and D'Souza et al.[169] show promise to capture these measurements, although they each contain the weaknesses mentioned in the previous section. It would be desirable for these experiments to contain turbulent flow. This would allow the $\pm 10\%$ uncertainty due to turbulent flow, which influences the radiation by changing the profiles of the boundary layer ablation products, to be assessed and possibly reduced.

The parametric uncertainty analysis in Section VIII showed that nearly a $\pm 15\%$ uncertainty results from

the radiation properties of ablation products. The spectral models used for many of these band systems, which include the C_3 Swings, C_3 UV, and C_2H UV bands, consist of simple curve fits based on early 1980s measurements. Increasing the fidelity of these models from the present one order-of-magnitude uncertainty on the absorption cross-section could reduce the $\pm 15\%$ uncertainty to nearly zero.

A $+20\%$ structural uncertainty was assigned to account for the influence of the radiative precursor on the radiative heating. The preliminary precursor model applied to assess the influence of this phenomenon is based on the two-temperature thermochemistry model. Park[174] suggests that this model is not appropriate for conditions where the absorption of radiation in the free-stream causes ionization. A study of the precursor that treats each specie with a separate temperature, such as that by Panesi et al.,[175] would be very useful in reducing the $+20\%$ structural uncertainty associated with the precursor.

XXV. Acknowledgments

The authors would like to thank NASA's Fundamental Aeronautics Program for funding this work and James L. Brown (NASA Ames), Scott Berry (NASA Langley), Brain Hollis (NASA Langley) and Joseph G. Marvin (ERC Corporation) for their comments and recommendations as members of the Uncertainty Quantification Team. Also, the assistance of Brett Cruden (NASA Ames) in analyzing the EAST data is greatly appreciated.

References

[1]Robinson, J. S., Wurster, K. E., and Mills, J. C., "Entry Trajectory and Aeroheating Environment Definition for Capsule-Shaped Vehicles," *Journal of Spacecraft & Rockets*, Vol. 46, No. 1, 2009, pp. 74–86.

[2]Howe, J. T. and Viegas, J. R., "Solutions of the Ionized Radiating Shock Layer, Including Reabsorption and Foreign Species Effects, and Stagnation Region Heat Transfer," NASA TR R 159, 1963.

[3]Hoshizaki, H. and Wilson, K. H., "Convective and Radiative Heat Transfer to an Ablating Body," *AIAA Journal*, Vol. 6, No. 8, 1968, pp. 1441–1449.

[4]Wilson, K. H. and Hoshizaki, H., "Effect of Ablation Product Absorption and Line Transitions on Shock Layer Radiative Transport," NASA CR 1264, 1969.

[5]Chin, J. H., "Radiation Transport for Stagnation Flows Including Effects of Lines and Ablation Layer," *AIAA Journal*, Vol. 7, No. 7, 1969, pp. 1310–1318.

[6]Rigdon, W. S., Dirling, R. B., and Thomas, M., "Stagnation Point Heat Transfer During Hypervelocity Atmospheric Entry," NASA CR 1462, 1970.

[7]Smith, G. L., Suttles, J. T., Sullivan, E. M., and Graves, R. A., "Viscous Radiating Flowfield on an Ablating Body," AIAA Paper 70–218, 1970.

[8]Garrett, L. B., Smith, G. L., and Perkins, J. N., "An Implicit Finite-Difference Solution to the Viscous Shock Layer, Including Effects of Radiation and Strong Blowing," NASA TR R 388, 1972.

[9]Engel, C. D., Farmer, C. F., and Pike, R. W., "Ablation and Radiation Coupled Viscous Hypersonic Shock Layers," *AIAA Journal*, Vol. 11, No. 8, 1973, pp. 1174–1181.

[10]Sutton, K., "Characteristics of Coupled Nongray Radiating Gas Flows with Ablation Product Effects About Blunt Bodies," Ph.d. dissertation, 1973.

[11]Moss, J. N., "The Effect of Ablation Injection on Radiative and Convective Heating," NASA TMX 71976, 1974.

[12]Moss, J. N., "Radiative Viscous-Shock-Layer Solutions with Coupled Mass Ablation," *AIAA Journal*, Vol. 14, No. 9, 1976, pp. 1311–1317.

[13]Gupta, R. N., Lee, K. P., Moss, J. N., and Sutton, K., "Viscous Shock Layer Solutions with Coupled Mass Ablation," *Journal of Spacecraft & Rockets*, Vol. 29, No. 2, 1992, pp. 173–181.

[14]Henline, W. D. and Tauber, M. E., "Trajectory-Based Heating Analysis for the European Space Agency/Rosetta Earth Return Vehicle," *Journal of Spacecraft & Rockets*, Vol. 31, No. 3, 1994, pp. 421–428.

[15]Bartlett, E. P., Nicolet, W. E., Anderson, L. W., and Kendall, R. M., "Further Studies of the Coupled Chemically Reacting Boundary Layer and Charring Ablator," NASA CR 92471, 1968.

[16]Matsuyama, S., Sakai, T., Sasoh, A., and Sawada, K., "Parallel Computation of Fully Coupled Hypersonic Radiating Flowfield Using Multiband Model," *Journal of Thermophysics and Heat Transfer*, Vol. 17, No. 1, 2003, pp. 21–28.

[17]Gollan, R. J., Jacobs, P. A., Karl, S., and Smith, S. C., "Numerical Modeling of Radiating Superorbital Flows," *ANZIAM Journal*, Vol. 45, 2004, pp. C248–C268.

[18]Johnston, C. O., Gnoffo, P. A., and Sutton, K., "Influence of Ablation on Radiative Heating for Earth Entry," *Journal of Spacecraft & Rockets*, Vol. 46, No. 3, 2009, pp. 481–491.

[19]Tauber, M. E., Palmer, G. E., and Yang, L., "Earth Atmospheric Entry Studies for Manned Mars Missions," *Journal of Thermophysics and Heat Transfer*, Vol. 6, No. 2, 1992, pp. 193–199.

[20]Park, C., "Aerothermodynamic of Manned Mars Mission," AIAA Paper 89–0313, 1989.

[21]Park, C. and Milos, F. S., "Computational Equations for Radiating and Ablating Shock Layers," AIAA Paper 1990–0356, 1990.

[22]Sutton, K. and Hartung, L. C., "Equilibrium Radiative Heating Tables for Earth Entry," NASA TM 102652, 1990.

[23]Cambier, J. L. and Tauber, M. E., "Computation of Nonequilibrium Shock Layers for the Comet Sample Return Vehicle," AIAA Paper 93–2863, 1993.

[24]Park, C., "Nonequilibrium Air Radiation (NEQAIR) Program: User's Manual," NASA TM 86707, 1985.

[25]Nicolet, W. E., "Advanced Methods for Calculating Radiation Transport in Ablation-Product Contaminated Boundary Layers," NASA CR 1656, 1970.

[26]Coleman, W. D., Hearne, L. F., Lefferdo, J. M., Gallagher, L. W., and Vojvodich, N. S., "Effects of Environmental and Ablator Performance Uncertainties on Heat-Shielding Requirements for Hyperbolic Entry Vehicles," *Journal of Spacecraft & Rockets*, Vol. 5, No. 11, 1968, pp. 1260–1270.

[27]Rolin, M. N. and Yurevich, F. B., "Evaluating Certain Ambiguities in Results of Calculations of Radiative-Convective Heat Exchange in Hypersonic Flow about a Body," *High Temperature*, Vol. 23, No. 2, 1985, pp. 282–288.

[28]Kleb, B. and Johnston, C. O., "Uncertainty Analysis of Air Radiation for Lunar Return Shock Layers," AIAA Paper 2008–6388, 2008.

[29]Palmer, G., "Uncertainty Analysis of CEV LEO and Lunar Return Entries," AIAA Paper 2007–4253, June 2007.

[30]Moss, J. N. and Simmonds, A. L., "Galileo Probe Forebody Flowfield Predictions During Jupiter Entry," AIAA Paper 1982–0874, 1982.

[31]Park, C., "Stagnation-Region Heating Environments of the Galileo Probe," *Journal of Thermophysics and Heat Transfer*, Vol. 23, No. 3, 2009, pp. 417–424.

[32]Nelson, H. F., "Analysis of Jupiter Probe Heat Shield Recession Uncertainties," AIAA Paper 78–919, 1978.

[33]Mazaheri, A., Gnoffo, P. A., Johnston, C. O., and Kleb, B., "LAURA Users Manual," NASA TM 2010-216836, 2010.

[34]Gnoffo, P. A., Johnston, C. O., and Thompson, R. A., "Implementation of Radiation, Ablation, and Free-Energy Minimization in Hypersonic Simulations," *Journal of Spacecraft & Rockets*, Vol. 47, No. 2, 2010, pp. 481–491.

[35]Mcbride, B. J., Zehe, M. J., and Gordon, S., "NASA Glenn Coefficients for Calculating Coefficients for Calculating Thermodynamic Properties of Individual Species," NASA TP 2002–211556, 2002.

[36]Wright, M. J., Bose, D., Palmer, G., and Levin, E., "Recommended Collision Integrals for Transport Property Computations 1: Air Species," *AIAA Journal*, Vol. 43, No. 12, 2005, pp. 2558–2564.

[37]Wright, M. J., Hwang, H., and Schwenke, D. W., "Recommended Collision Integrals for Transport Property Computations Part 2: Mars and Venus Entries," *AIAA Journal*, Vol. 45, No. 1, 2007, pp. 281–288.

[38]Svhehla, R. A., "Estimated Viscosities and Thermal Conductivities of Gases at High Temperatures," NASA TR R 142, 1962.

[39]Park, C., Jaffe, R. L., and Partridge, H., "Chemical-Kinetic Parameters of Hyperbolic Earth Entry," *Journal of Thermophysics and Heat Transfer*, Vol. 15, No. 1, 2001, pp. 76–90.

[40]Johnston, C. O., Gnoffo, P. A., and Mazaheri, A., "A Study of Ablation-Flowfield Coupling Relevant to the Orion Heatshield," AIAA Paper 2009–4318, 2009.

[41]Cebeci, T., "Variation of the Van Driest Damping Parameter with Mass Transfer," *AIAA Journal*, Vol. 11, No. 2, 1973, pp. 237–238.

[42]Cheatwood, F. M. and Thompson, R. A., "The Addition of Algebraic Turbulence Modeling to Program LAURA," NASA TM 107758, 1993.

[43]Rindal, R. A. and Powars, C. A., "Effects of Carbon Vapor Thermochemistry Uncertainties on R/V Ablation Predictions," AIAA Paper 1971–414, 1971.

[44]Bueche, J. F., "Effects of Improvements and Uncertainties in Thermophysical Properties on Carbon Phenolic Heatshield Thermal Performance Predictions," AIAA Paper 1977–787, 1977.

[45]Chen, Y.-K., Squire, T., Laub, B., and Wright, M., "Monte Carlo Analysis for Spacecraft Thermal Protection System Design," AIAA Paper 2006–2951, 2006.

[46]Johnston, C. O., Hollis, B. R., and Sutton, K., "Spectrum Modeling for Air Shock-Layer Radiation at Lunar-Return Conditions," *Journal of Spacecraft & Rockets*, Vol. 45, Sep.-Oct. 2008, pp. 865–878.

[47]Johnston, C. O., "Improved Exponential Integral Approximation for Tangent-Slab Radiation Transport," *Journal of Thermophysics and Heat Transfer*, Vol. 24, No. 3, 2010, pp. 659–661.

[48]Wright, M. J., Bose, D., and Chen, Y.-K., "Probabilistic Modeling of Aerothermal and Thermal Protection Material Response Uncertainties," *AIAA Journal*, Vol. 45, No. 2, 2007, pp. 399–410.

[49]Moss, J. N., Simmonds, A. L., and Anderson, E. C., "Turbulent Radiating Shock Layers with Coupled Ablation Injection," *Journal of Spacecraft & Rockets*, Vol. 17, No. 3, 1980, pp. 177–183.

[50]Park, C., "Injection-Induced Turbulence in Stagnation-Point Boundary Layers," *AIAA Journal*, Vol. 22, No. 2, 1984, pp. 219–2225.

[51]Zeldovich, Y. B. and Raizer, Y. P., *Physics of Shock Waves and High Temperature Hydrodynamic Phenomena*, Academic Press, New York and London, 1967.

[52]Yoshikawa, K. K., "Analysis of Radiative Heat Transfer for Large Objects at Meteoric Speeds," NASA TN 4051, 1967.

[53]Lasher, L. E. and Wilson, K. H., "Effect of Shock Precursor Heating on Radiative Flux to Blunt Bodies," NASA CR 1265, 1969.

[54]Vertushkin, V. K. and Romishevskii, E. A., "Influence of the Precursor Effect on Hypersonic Blunt Body Flow," *Fluid Dynamics*, , No. 6, 1970, pp. 933–939.

[55]Zinn, J. and Anderson, R. C., "Structure and Luminosity of Strong Shock Waves in Air," *The Physics of Fluids*, Vol. 16, No. 10, 1973, pp. 1639–1644.

[56]Stanley, S. A. and Carlson, L. A., "Effects of Shock Wave Precursor Ahead of Hypersonic Entry Vehicles," *Journal of Spacecraft & Rockets*, Vol. 29, No. 2, 1992, pp. 190–197.

[57]Nemtchinov, I. V., Popova, O. P., Shuvalov, V. V., and Svetsov, V. V., "Radiation Emitted During the Flight of Asteroids and Comets through the Atmosphere," *Planetary and Space Sciences*, Vol. 42, No. 6, 1994, pp. 491–506.

[58]Golub, A. P., Kosarev, I. B., Nemchinov, I. V., and Shuvalov, V. V., "Emission and Ablation of a Large Meteoroid in the Course of Its Motion Through the Earth's Atmosphere," *Solar System Research*, Vol. 30, No. 3, 1996, pp. 213–228.

[59]Bauman, P. T., Stogner, R., Carey, G. F., Schulz, K. W., Upadhyay, R., and Maurente, A., "Loose-Coupling Algorithm for Simulating Hypersonic Flows with Radiation and Abaltion," *Journal of Spacecraft & Rockets*, Vol. 48, No. 1, 2011, pp. 72–80.

[60]Romanov, G. S., Stankevich, Y. A., Stanchits, L. K., and Stepanov, K. L., "Thermodynamic and Optical Properties of Gases in a Wide Range of Parameters," *International Journal of Heat and Mass Transfer*, Vol. 38, No. 3, 1995, pp. 545–556.

[61]Cunto, W., Mendoza, C., Ochsenbein, F., and Zeippen, C., "TOPbase at the CDS," *Astronomy and Astrophysics*, Vol. 275, Aug. 1993, pp. L5–L8, see also vizier.u-strasbg.fr/topbase/topbase.html.

[62]Barnwell, R. W., "Inviscid Radiating Shock-Layers About Spheres Traveling at Hyperbolic Speeds in Air," NASA TR R-311, 1969.

[63]Hash, D., "Fire II Calculations for Hypersonic Nonequilibrium Aerothermodynamics Code Verification: DPLR, LAURA and US3D," AIAA Paper 2007–0605, 2007.

[64]Palmer, G., White, T., and Pace, A., "Direct Coupling of the NEQAIR Radiation and DPLR CFD Codes," AIAA Paper 2010–5051, 2010.

[65]Hartung, L. C. and Hassan, H. A., "Radiation Transport Around Axisymmetric Blunt Body Vehicles Using a Modified Differential Approximation," *Journal of Thermophysics and Heat Transfer*, Vol. 7, No. 2, 1993, pp. 220–227.

[66]Potter, D., "Modeling of Radiating Shock Layers for Atmospheric Entry at Earth and Mars," Ph.d. dissertation, 2011.

[67]Park, C., "Interaction of Spalled Particles with Shock Layer Flow," *Journal of Thermophysics and Heat Transfer*, Vol. 13, No. 4, 1999, pp. 441–449.

[68]Lundell, J. H., "Spallation of the Galileo Probe Heat Shield," AIAA Paper 1982–0852, 1982.

[69]Park, C., Raiche, G. A., and Driver, D. M., "Radiation of Spalled Particles in Shock Layers," *Journal of Thermophysics and Heat Transfer*, Vol. 18, No. 4, 2004, pp. 519–525.

[70]Sutton, K. and Gnoffo, P. A., "Multi-Component Diffusion with Application to Computational Aerothermodynamics," AIAA Paper 98–2575, 1998.

[71]Gnoffo, P. A., Weilmuenster, K. J., Hamilton, H. H., Olynick, D. A., and Venkatapathy, E., "Computational Aerothermodynamic Design Issues for Hypersonic Vehicles," *Journal of Spacecraft & Rockets*, Vol. 36, No. 1, 1999, pp. 21–43.

[72]Gosse, R. and Candler, G., "Diffusion Model Comparisons for Direct Reentry Applications," AIAA Paper 2003–3635, 2003.

[73]Rini, P. and Degrez, G., "Elemental Demixing in Air and Carbon Dioxide Stagnation-Line Flows," *Journal of Thermophysics and Heat Transfer*, Vol. 18, No. 4, 2004, pp. 511–518.

[74]Swiler, L. P., Paez, T. L., Mayes, R. L., and Eldred, M. S., "Epistemic Uncertainty in the Calculation of Margins," AIAA Paper 2010–2249, 2010.

[75]Kreinovich, V. and Ferson, S. A., "A New Cauchy-Based Black-Box Technique for Uncertainty in Risk Analysis," *Reliability Engineering and Systems Safety*, Vol. 85, 2004, pp. 267–279.

[76]Bauschlicher, C. W. and Langhoff, S. R., "Theoretical Study of the First and Second Negative System of N_2^+," *Journal of Chemical Physics*, Vol. 88, No. 1, 1988, pp. 329–338.

[77]Laux, C. O. and Kruger, C. H., "Arrays of Radiative Transition Probabilities for the N_2 First and Second Positive, NO Beta and Gamma N_2^+ First Negative, and O_2 Schumann-Runge Band Systems," *Journal of Quantitative Spectroscopy and Radiative Transfer*, Vol. 48, No. 1, 1992, pp. 9–24.

[78]Stark, G., Huber, K. P., Yoshino, K., Chan, M.-C., Matsui, T., Smith, P. L., and Ito, K., "Line Oscillator Strength Measurements in the 0-0 Band of the $c^4\ ^1\Sigma_u^+ - X^1\Sigma_g^+$ Transition of N_2," *The Astrophysical Journal*, Vol. 531, 2000, pp. 321–328.

[79]Chan, W. F., Cooper, G., Sodhi, R. N. S., and Brion, C. E., "Absolute Optical Oscillator Strengths for Discrete and Continuum Photoabsorption of Molecular Nitrogen (11-200 eV)," *Chemical Physics*, Vol. 170, 1993, pp. 81–97.

[80]Appleton, J. P. and Steinberg, M., "Vacuum-Ultraviolet Absorption of Shock-Heated Vibrationally Excited Nitrogen," *Chemical Physics*, Vol. 46, No. 4, 1967, pp. 1521–1529.

[81]Carter, V. L., "High-Resolution N_2 Absorption Study from 730 to 980 A," *Chemical Physics*, Vol. 56, No. 8, 1972, pp. 4195–4205.

[82]Wiese, W. L., Fuhr, J. R., and Deters, T. M., "Atomic Transition Probabilities of Carbon, Nitrogen, and Oxygen," *Journal of Physical and Chemical Reference Data Monograph*, , No. 7, 1996.

[83]Griem, H. R., *Spectral Line Broadening by Plasmas*, Academic Press, New York, 1974.

[84]Wilson, K. H. and Nicolet, W. E., "Spectral Absorption Coefficients of Carbon, Nitrogen, and Oxygen Atoms," *Journal of Quantitative Spectroscopy and Radiative Transfer*, Vol. 7, 1967, pp. 891–941.

[85]The Opacity Project Team, *The Opacity Project*, Vol. 1, Bristol and Philadelphia: Institute of Physics Publishing, 1995.

[86]Hibbert, A., Biemont, E., Godefroid, M., and Vaeck, N., "New Accurate Transition Probabilities for Astrophysically Important Lines of Neutral Nitrogen," *Astronomy and Astrophysics Supplement Series*, Vol. 88, 1991, pp. 505–524.

[87]Goldbach, C., Martin, M., Nollez, G., Plomdeur, P., Zimmerman, J.-P., and Babic, D., "Oscillator Strength Measurements in the Vacuum Ultraviolet: I The Strong 1243, 1493, 1743 Angstrom Multiplets of Neutral Nitrogen," *Astronomy and Astrophysics*, Vol. 161, 1986, pp. 47–54.

[88]Goldbach, C., Ludke, T., Martin, M., and Nollez, G. D., "Oscillator Strength Measurements in the Vacuum Ultraviolet: V. Neutral Nitrogen Lines in the 950–1200 Angstrom Range," *Astronomy and Astrophysics*, Vol. 266, 1992, pp. 605–612.

[89]Goldbach, C. and Nollez, G. D., "Oscillator Strength Measurements in the Vacuum Ultraviolet: III. Weak Lines of Neutral Nitrogen," *Astronomy and Astrophysics*, Vol. 201, 1988, pp. 189–193.

[90]Zhu, Q., Bridges, J. M., Hahn, T., and Wiese, W. L., "Atomic Transition-Probability Measurements for Prominent Spectral Lines of Neutral Nitrogen," *Physical Review A*, Vol. 40, 1989, pp. 3721–3726.

[91]Musielok, J., Wiese, W. L., and Veres, G., "Atomic Transition Probabilities and Tests of the Spectroscopic Coupling Scheme for N I," *Physical Review A*, Vol. 51, 1995, pp. 3588–3597.

[92]Wiese, W. L., Smith, M. W., and Glennon, B. M., "Atomic Transition Probabilities, Vol. 1, Hydrogen through Neon," NSRDS-NBS 4, National Bureau of Standards, May 1966.

[93]Morris, J. C. and Garrison, R. L., "Measurements of the Radiation Emitted f-Values and Stark Half-Widths for the Strong Vacuum Ultraviolet Lines of O I and N I," *Physical Review*, Vol. 188, 1969, pp. 112–118.

[94]Helbig, V., Kelleher, D. E., and Wiese, W. L., "Stark Broadening Study of Neutral Nitrogen Lines," *Physical Review A*, Vol. 14, 1974, pp. 1082–1093.

[95]Cullmann, E. and Labuhn, F., "Stark Broadening of Nitrogen (I) Vacuum-U.V. Lines Using a Wall-Stabalized Arc," *Journal of Quantitative Spectroscopy and Radiative Transfer*, Vol. 20, 1978, pp. 205–209.

[96]Nubbemeyer, H., "Experimental Ion Contributions to the Stark Broadening of Neutral Nitrogen Spectral Lines in the Vacuum UV," *Physical Review A*, Vol. 22, 1980, pp. 1034–1040.

[97]Goly, A. and Weniger, S., "Stark Broadening of Some C(I) and N(I) Vacuum Ultraviolet Lines," *Journal of Quantitative Spectroscopy and Radiative Transfer*, Vol. 36, 1986, pp. 147–161.

[98]Sohns, E. and Kock, M., "Plasma Diagnostics Based on Self-Reversed Lines-II. Application to Nitrogen, Carbon, and Oxygen Arc Measurements in the Vacuum Ultraviolet," *Journal of Quantitative Spectroscopy and Radiative Transfer*, Vol. 47, 1992, pp. 335–343.

[99]Nahar, S. N. and Pradhan, A. K., "Electron-Ion Recombination Rate Coefficients, Photoionization Cross-Sections, and Ionization Fractions for Astrophysically Abundant Elements. I. Carbon and Nitrogen," *The Astrophysical Journal Supplement Series*, Vol. 111, 1997, pp. 339–355.

[100]Bell, K. L. and Berrington, K. L., "Photoionization of the ^{4} S_o Ground State of Atomic Nitrogen and Atomic Nitrogen ^{4} S_o–^4P Oscillator Strengths," *Journal of Physics B*, Vol. 24, 1991, pp. 933–941.

[101]Bell, K. L. and Berrington, K. L., "Photoionization of Excited States of Atomic Nitrogen," *Journal of Physics B*, Vol. 25, 1992, pp. 1209–1216.

[102]Nahar, S. N., "Photoionization Cross Sections and Oscillator Strengths for Oxygen Lines: O I – O VII," *Physical Review A*, Vol. 58, 1998, pp. 3766–3782.

[103]Tayal, S. S., "Resonant Photoionization Cross Sections and Branching Ratios for Atomic Oxygen," *Physical Review A*, Vol. 65, 2002, pp. 032724–+.

[104]Morris, J. C., Krey, R. U., and Bach, G. R., "The Continuum Radiation of Oxygen and Nitrogen for Use in Plasma Temperature Determination," *Journal of Quantitative Spectroscopy and Radiative Transfer*, Vol. 6, 1966, pp. 727–740.

[105]Thomas, G. M. and Menard, W. A., "Measurements of the Continuum and Atomic Line Radiation from High Temperature Air," *AIAA Journal*, Vol. 5, No. 12, 1967, pp. 2214–2223.

[106]Marrone, P. V. and Wurster, W. H., "Measurement of Atomic Nitrogen and Carbon Photoionization Cross Sections Using Shock Tube Vacuum Ultraviolet Spectroscopy," *Journal of Quantitative Spectroscopy and Radiative Transfer*, Vol. 11, 1971, pp. 327–348.

[107]Ciffone, D. L. and Borucki, J. G., "Spectral Measurements of Nitrogen Continuum Radiation Behind Incident Shocks at Speeds up to 13 km/sec," *Journal of Quantitative Spectroscopy and Radiative Transfer*, Vol. 11, 1971, pp. 1291–1310.

[108]Cooper, D. M., "Spectral Intensity Measurements from High-Pressure Nitrogen Plasma," *Journal of Quantitative Spectroscopy and Radiative Transfer*, Vol. 12, 1972, pp. 1175–1189.

[109]Moskvin, Y. V., "Cross-Section Photo-Detachment of the Negative Nitrogen Ion," *Optics and Spectroscopy*, Vol. 28, 1970, pp. 356–356.

[110]Asinovskii, E. I., Kirillin, A. V., and Kobzev, G. A., "Continuous Radiation of Nitrogen Plasma," *High Temperature*, Vol. 6, 1968, pp. 710–712.

[111]Soon, W. H. and Kunc, J. A., "Nitrogen-Plasma Continuum Emission Associated with $N^-(^3P)$ and $N^-(^1D)$ ions," *Physical Review A*, Vol. 41, 1990, pp. 4531–4533.

[112]Konkov, A. A., Nikolaev, V. M., and Plastinin, Y. A., "On the Intensity of Emission Continuum of the Negative Nitrogen Atom," *Optics and Spectroscopy*, Vol. 25, 1968, pp. 380–382.

[113]D'Yachkov, L. G., Golubev, O. A., Kobzev, G. A., and Vargin, A. N., "Studies of Continuum Radiation from Nitrogen, Oxygen and Carbon Dioxide Plasmas in the Vacuum Ultraviolet Region," *Journal of Quantitative Spectroscopy and Radiative Transfer*, Vol. 20, 1978, pp. 175–189.

[114]Babou, Y., Riviere, P., Perrin, M.-Y., and Soufiani, A., "Spectroscopic Data for the Prediction of Radiative Transfer in CO_2-N_2 Plasmas," *Journal of Quantitative Spectroscopy and Radiative Transfer*, Vol. 110, 2009, pp. 89–108.

[115]da Silva, M. L. and Dudeck, M., "Arrays of Radiative Transition Probabilities for CO_2-N_2 Plasmas," *Journal of Quantitative Spectroscopy and Radiative Transfer*, Vol. 102, 2006, pp. 348–386.

[116]Kokkin, D. L., Bacskay, G. B., and Schmidt, T. W., "Oscillator Strengths and Radiative Lifetimes for C_2: Swan, Ballik-Ramsay, Phillips, and $d^3\Pi_g$-$c^3\Sigma_u$," *Journal of Chemical Physics*, Vol. 126, No. 084302, 2007.

[117]Schmidt, T. W. and Bacskayt, G. B., "Oscillator Strengths of the Mulliken, Swan, Ballik-Ramsay, Phillips, and $d^3\Pi_g$-$c^3\Sigma_u$ Systems of C_2 Calculated by MRCI Methods Utilizing a Biorthogonal Transformation of CASSCF Orbitals," *Journal of Chemical Physics*, Vol. 127, No. 234310, 2007.

[118]Cooper, D. M. and Jones, J. J., "An Experimental Determination of the Cross Section of the Swings Band System of C_3," *Journal of Quantitative Spectroscopy and Radiative Transfer*, Vol. 22, 1979, pp. 201–208.

[119]Prakash, S. G. and Park, C., "Shock Tube Spectroscopy of C_3+C_2H Mixture in the 140-700 nm Range," AIAA Paper 1979–0094, 1979.

[120]Shinn, J. L., "Optical Absorption of Carbon and Hydrocarbon Species from Shock Heated Acetylene and Methane in the 135-220 nm Wavelength Range," AIAA Paper 1981–1189, 1981.

[121]Allison, A. C. and Dalgarno, A., "Band Oscillator Strengths and Transitions Probabilities for the Lyman and Werner Systems of H_2, HD, and D_2," *Atomic Data*, Vol. 1, No. 3, 1970, pp. 289–304.

[122]Fabian, W. and Lewis, B. R., "Experimentally Determined Oscillator Strengths for Molecular Hydrogen-I. The Lyman and Werner Bands Above 900 A," *Journal of Quantitative Spectroscopy and Radiative Transfer*, Vol. 14, 1974, pp. 523–535.

[123]Lewis, B. R., "Experimentally Determined Oscillator Strengths for Molecular Hydrogen-II. The Lyman and Werner Bands Below 900 A." *Journal of Quantitative Spectroscopy and Radiative Transfer*, Vol. 14, 1974, pp. 537–546.

[124]Brewer, L. and Engelke, J. L., "Spectrum of C_3," *Journal of Chemical Physics*, Vol. 36, No. 4, 1962, pp. 992–998.

[125]Moss, J. N., Jones, J. J., and Simmonds, A. L., "Radiative Flux Penetration Through a Blown Shock Layer," AIAA Paper 1978–908, 1978.

[126]Arnold, J. O., Cooper, D. M., Park, C., and Prakash, S. G., "Line-by-Line Transport Calculations for Jupiter Entry Probes," AIAA Paper 1979–1082, 1979.

[127]Escalante, V., "Photoionization of Excited States of Neutral Atomic Carbon and Singly Ionized Nitrogen," *Atomic Data and Nuclear Data Tables*, Vol. 51, No. 1, 1992, pp. 1–57.

[128]Gurvich, L. V., Veyts, I. V., and Alcock, C. B., *Thermodynamic Properties of Individual Substances*, Hemisphere, New York, 1989.

[129]Jones, J. J., "The Optical Absorption of Triatomic Carbon C_3 for the Wavelength Range 260 to 560 nm," NASA TP 1141, 1978.

[130]Capitelli, M., Colonna, G., Giordano, D., and Marraffa, L., "High-Temperature Thermodynamic Properties of Mars-Atmosphere Components," *Journal of Spacecraft & Rockets*, Vol. 42, No. 6, 2005, pp. 980–989.

[131]Coufal, O., Sezemsky, P., and Zivny, O., "Database System of Thermodynamic Properties of Individual Substances at High Temperatures," *Journal of Physics D: Applied Physics*, Vol. 38, 2005, pp. 1265–1274.

[132]Gordon, S. and Mcbride, B. J., "Thermodynamic Data to 20,000 K for Monatomic Gases," NASA TP 1999–208523, 1999.

[133]Johnston, C. O., *Nonequilibrium Shock-Layer Radiative Heating for Earth and Titan Entry*, Ph.D. thesis, Virginia Polytechnic Institute and State University, 2006.

[134]Pomerantz, J., "The Influence of the Absorption of Radiation on Shock Tube Phenomena," *Journal of Quantitative Spectroscopy and Radiative Transfer*, Vol. 1, 1963, pp. 185–248.

[135]Nelson, H. F., "Effects of Reduction of the Ionization Potential on Solutions of the Rankine-Hugoniot Equations for Jovian Entry," *Journal of Quantitative Spectroscopy and Radiative Transfer*, Vol. 16, 1976, pp. 1061–1064.

[136]Nelson, H. F. and Goulard, R., "Equilibrium Radiation from Isothermal Hydrogen-Helium Plasmas," *Journal of Quantitative Spectroscopy and Radiative Transfer*, Vol. 8, 1968, pp. 1351–1372.

[137]Griem, H. R., *Thermodynamic Properties of Individual Substances*, Cambridge University Press, Cambridge, 1997.

[138]Inglis, D. R. and Teller, E., "Ionic Depression of Series Limits in One Electron Spectra," *Astrophysical Journal*, Vol. 90, 1939, pp. 439–448.

[139]Ralchenko, Y., "NIST Atomic Spectra Database, Version 3.1.0," physics.nist.gov/PhysRefData/ASD/, July 2006, last accessed September 3rd, 2007.

[140]Sutton, K., "Air Radiation Revisited," AIAA Paper 84–1733, 1984.

[141]Hoshizaki, M., "Equilibrium Total Radiation Measurements in Air at Superorbital Entry Velocities," Lockheed msc, report 6-90-63-97, 1963.

[142]Thomas, G. M. and Menard, W. A., "Measurements of the Continuum and Atomic Line Radiation from High-Temperature Air," *AIAA Journal*, Vol. 5, No. 12, 1967, pp. 2214–2223.

[143]Nerem, R. M. and Stickford, G. H., "Shock-Tube Studies of Equilibrium Air Radiation," *AIAA Journal*, Vol. 3, No. 6, 1965, pp. 1011–1018.

[144]Gruszczynski, J. S. and Warren, W. R., "Study of Equilibrium Air Total Radiation," *AIAA Journal*, Vol. 5, No. 3, 1967, pp. 517–525.

[145]Grinstead, J., Wilder, M., Olejniczak, J., Bogdanoff, D., Allen, G., and Danf, K., "Shock-Heated Air Radiation Measurements at Lunar Return Conditions," AIAA Paper 2008–1244, Jan. 2008.

[146]Cruden, B. A., Martinez, R., Grinstead, J. H., and Olejniczak, J., "Simultaneous Vacuum Ultraviolet through Near IR Absolute Radiation Measurements with Spatiotemporal Resolution in an Electric Arc Shock Tube," AIAA Paper 2009–4240, 2009.

[147]Allen, R. A., Rose, P. H., and Camm, J. C., "Nonequilibrium and Equilibrium Radiation at Super-Satellite Re-Entry Velocities," AVCO Research Report 156, 1962.

[148]Donohue, K., Reincecke, R. D., Marinelli, W. J., Krech, R. H., and Caledonia, G. E., "Aerothermodynamic Radiation Studies," NASA CR 185666, 1991.

[149]Koreeda, J., Ohama, Y., and Honma, H., "Imaging Spectroscopy of the Nonequilibrium Shock Front Radiation in Air," *Shock Waves*, Vol. 8, No. 2, 1998, pp. 71–78.

[150]Matsuda, A., Fujita, K., Sato, S., and Abe, T., "Nonequilibrium Phenomena Behind Strong Shock Waves Generated in Superorbital Reentry Flight," *Journal of Thermophysics and Heat Transfer*, Vol. 18, No. 3, 2004, pp. 342–348.

[151]Wood, A. D., Hoshizaki, H., Andrews, J., and Wilson, K., "Measurements of the Total Radiant Intensity of Air," *AIAA Journal*, Vol. 7, No. 1, 1969, pp. 130–139.

[152]Golobic, R. A. and Nerem, R. M., "Shock-Tube Measurements of End-Wall Radiative Heat Transfer in Air," *AIAA Journal*, Vol. 6, No. 9, 1968, pp. 1741–1747.

[153]Krey, R. U. and Morris, J. C., "Experimental Total and Total Line Radiation of Nitrogen, Oxygen, and Argon Plasmas," *Physics of Fluids*, Vol. 13, No. 6, 1970, pp. 1483–1487.

[154]Schreiber, P. W., Hunter, A. M., and Benedetto, K. R., "Measurement of Nitrogen Plasma Transport Properties," *AIAA Journal*, Vol. 10, No. 5, 1972, pp. 670–674.

[155]Schreiber, P. W., Hunter, A. M., and Benedetto, K. R., "Electrical Conductivity and Total Emission Coefficient of Air Plasma," *AIAA Journal*, Vol. 11, No. 6, 1973, pp. 815–821.

[156]Devoto, R. S., Bauder, U. H., and Cailleteau, U. H., "Air Transport Coefficients from Electric Arc Measurements," *Physics of Fluids*, Vol. 21, No. 4, 1978, pp. 552–558.

[157]Ernst, K. A., Kopainsky, J. G., and Maecker, H. H., "The Energy Transport, Including Emission and Absorption, in N_2-Arcs of Different Radii," *IEEE Transactions in Plasma Sciences*, Vol. 21, No. 4, 1978, pp. 552–558.

[158]Asinovsky, E. I., Drokhanova, E. V., Kirillin, A. V., and Lagarkov, A. N., "Experimental and Theoretical Investigation of the Thermal Conductivity Coefficient and of the Total Emission Coefficient," *High Temperature*, Vol. 5, No. 5, 1967, pp. 662–671.

[159]Ogurtsova, N. N., Podoshenskii, I. V., and Shelemina, V. M., "The Radiative Power of Air, N_2 and CO_2 at 10,000 K," *High Temperature*, Vol. 6, No. 6, 1968, pp. 788–793.

[160]Cruden, B. A., Prabhu, D., Martinez, R., Lee, H., Bose, D., and Grinstead, J. H., "Absolute Radiation Measurements in Venus and Mars Entry Conditions," AIAA Paper 2010–4508, 2010.

[161]Brandis, A. M., Johnston, C. O., Cruden, B. A., Prabhu, D., and Bose, D., "Uncertainty Analysis of NEQAIR and HARA Predictions of Air Radiation Measurements Obtained in the EAST Facility," AIAA Paper 2011–XXXX, 2011.

[162]Johnston, C. O., "A Comparison of EAST Shock Tube Radiation Measurements with a New Air Radiation Model," AIAA Paper 2008–1245, Jan. 2008.

[163]Bose, D., McCorkle, E., Thompson, C., Bogdanoff, D., Prabhu, D. K., Allen, G. A., and Grinstead, J., "Analysis and Model Validation of Shock Layer Radiation in Air," AIAA Paper 2008–1246, Jan. 2008.

[164]Georg, E. B. and Yakushin, M. I., "Thermal Boundary Layer on Models Disintegrating in a High-Enthalpy Gas Stream," *Fluid Dynamics*, Vol. 11, No. 1, 1976, pp. 26–31.

[165]Georg, E. B. and Yakushin, M. I., "Radiational Properties of the Decomposition Products of a Model Around Which Flows a Subsonic High-Temperature Plasma Stream," *Fluid Dynamics*, Vol. 13, No. 6, 1978, pp. 854–857.

[166]Georg, E. B. and Yakushin, M. I., "Spectral Extinction Coefficient of Vapor of Heatproof Material Destroyed by a High-Temperature Flux of Air Plasma," *Journal of Engineering Physics*, Vol. 38, No. 1, 1980, pp. 85–89.

[167]Gudzovskii, A. V. and Kondranin, T. V., "Screening of Radiative Heat Flux by the Injection of Products of the Destruction of Asbestos Plastic in Hypersonic Flow over a Sphere," *Journal of Engineering Physics*, Vol. 46, No. 2, 1984, pp. 303–308.

[168]Schott, T., Herring, G. C., Munk, M. M., Grinstead, J. H., and Prabhu, D. K., "Fiber-Based Measurement of Bow-Shock Spectra for Reentry Flight Testing," AIAA Paper 2010–0301, 2010.

[169]D'Souza, M. G., Eichmann, T. N., Potter, D. F., Morgan, R. G., McIntyre, T. J., Jacobs, P. A., and Mudford, N. R., "Observation of an Ablating Surface in Expansion Tunnel Flow," *AIAA Journal*, Vol. 48, No. 7, 2010, pp. 1557–1560.

[170]Reid, R. C., Rochelle, W. C., and Milhoan, J. D., "Radiative Heating to the Command Module: Engineering Prediction and Flight Measurement," , No. 58091, 1972.

[171]Olynick, D., Chen, Y.-K., and Tauber, M. E., "Aerothermodynamics of the Stardust Sample Return Capsule," *Journal of Spacecraft & Rockets*, Vol. 36, No. 3, 1999, pp. 442–462.

[172]Jenniskens, P., Koop, M., and Albers, J., "Intensified Low-Resolution Optical Spectroscopy of the Stardust Sample Return Capsule Entry," *Journal of Spacecraft & Rockets*, Vol. 47, No. 6, 2010, pp. 895–900.

[173]Liu, Y., Prabhu, D., Trumble, K. A., Saunders, D., and Jenniskens, P., "Radiation Modeling for the Reentry of the Stardust Sample Return Capsule," *Journal of Spacecraft & Rockets*, Vol. 47, No. 5, 2010, pp. 741–752.

[174]Park, C., "The Limits of Two-Temperature Model," AIAA Paper 2010–0911, 2010.

[175]Panesi, M., Magin, T., Bourdon, A., Bultel, A., and Chazot, O., "Fire II Flight Experiment Analysis by Means of a Collisional-Radiative Model," *Journal of Thermophysics and Heat Transfer*, Vol. 23, No. 2, 2009, pp. 236–248.